UNIVERSITAT
POLITÈCNICA
DE VALÈNCIA

Doctoral Thesis

ADVANCED TECHNIQUES FOR THE CHARACTERIZATION AND EXPERIMENTAL VALIDATION OF PASSIVE INTER-MODULATION EFFECT (PIM) IN SPACE COMMUNICATIONS SYSTEMS

Davide Smacchia

Advisors:
Dr. Pablo Soto Pacheco (Universitat Politècnica de València)
Dr. Vicente E. Boria Esbert (Universitat Politècnica de València)

Dissertation submitted to the Departamento de Comunicaciones, in partial fulfillment of the requirements for:
Título de Doctor por la Universitat Politècnica de València
València, February 2022

Acknowledgements

This Ph.D. may be intended as the arrival of a long path started on January 2008 when, through an Erasmus exchange, I left my former university in Perugia to do my Master Thesis at the Universitat Politècnica de València.

In such a time I had the chance to know the two tutors of this work, Vicente Boria and Pablo Soto, who took me in their research group (GAM) as a younger brother. My deepest thanks to them, both for the technical and human aspects. Thanks for the endless discussions, brainstormings, papers written with six hands.

In 2010 I moved to the ESA-VSC labs, where I had the opportunity, and the luck, to meet an exceptional team work lead by David Raboso and David Argiles. Both Davids, along with my colleagues Laura, Oscar, Mariam, Marta, Maria José, Rocio, Rafa, and more recently Javier and John, helped me to face the RF high power breakdown & disturbance phenomena in satellite payloads. In particular the Passive-Inter-Modulation (PIM) effect, which is the one that raised more interest in myself and that is the focal point of this Ph.D. thesis work. I am in debt with you all, for the discussions, for the support, for the test campaign carried out together, all elements that, once mixed, have stimulated my research activity.

Among the group above, a particular mention goes to David Raboso, who with his long experience helped me to address many investigations.

A thanksgiving also goes to Marco Guglielmi, who gave me useful food for thoughts for some of the topics treated in this Ph.D. work.

I would also thank Ana Rodriguez and José Vicente Morro, that in these 14 years in Valencia were always present. A warmest thank to Stefano Sirci that, despite now left to colder places, supported me like a brother.

Grazie alla famiglia che ho lasciato in Italia, che mi ha sempre appoggiato nelle mie scelte di vita. Mamma, babbo, Paolo, Gloria, Annita, Anastasia, Romina, Ettore, Enea, Ascanio vi voglio un mondo di bene e vi tengo sempre nel mio cuore. Come ci tengo i familiari che ci hanno lasciati troppo presto.

Per ultimo, ma in primis per importanza, un Grazie alla mia di famiglia. Erika ed Elia, vi amo. Questo lavoro è dedicato a voi.

Davide

Abstract

Modern satellite payloads operate in multicarrier scenarios, under a continuous demand for higher capacity links. This leads to an increase in the RF power levels, frequency of operation, and the number of transmitted channels, thus stimulating non-linear high-power effects, such as Multipactor, Corona, thermal issues and Passive Inter-Modulation (PIM).

Among the above-mentioned phenomena, PIM is largely the less studied, or, at least, understood. This is due to its extreme non-linear nature and its close relation to workmanship, which make very difficult the development of models able to faithfully predict and explain PIM degradation. PIM terms, once ignited in the downlink, may interfere the real weak signal to be detected in the uplink reception channel, thus threatening the payload throughput.

Traditional PIM models are based on a two-carriers excitation. This is a simple and quite representative case, but has significant differences with the real multicarrier scenario. This Ph.D. thesis work tries to diminish this gap by means of two novel contributions of relevance for real operation conditions. Firstly, the role of the carrier phases (neglected for two-carriers excitation) has been theoretically investigated. Secondly, a new model to account for the effect of non-contributing carriers for a given PIM term has been developed, which is based on a novel energy conservation assumption. The resulting enhanced models fit to experimental data.

Due to the complexity of PIM modeling, PIM validation of RF payload components is conducted only by testing. The availability of low PIM test set-ups is therefore of great interest for the space industry and space agencies. However, the design of low PIM test benches is very challenging, as their intrinsic residual PIM (noise floor) has to be well below the one requested to validate the test devices. For satellite hardware, a dynamic range of 185 dBc between the RF power levels of the transmission carriers and the signal to be detected can exist.

During this Ph.D. thesis work, novel integrated test bed architectures in waveguide technology, both for conducted (forward and backward) and radiated PIM scenarios, have been developed. These architectures consent a considerable mitigation of the residual PIM noise floor of the test facility, being at the same time flexible, free from unwanted interactions and spurious resonances, and able to

withstand considerable RF power levels for the transmission carriers. The key elements of these set-ups are the low PIM multiplexers, which may integrate two new families of high-power waveguide filters able to provide a high number of transmission zeros, and therefore a high rejection, in the PIM reception channel.

The test benches conceived for measuring conducted backward PIM, however, are normally unprotected from the PIM generated by the termination absorbing the high-power transmission carriers. To alleviate this situation, a new type of low PIM terminations in waveguide technology has been proposed and verified with real PIM tests, showing a noticeable benefit in mitigating the residual PIM noise floor of backward PIM test facilities. Moreover, novel transitions able to improve the PIM performance of standard flanges have also been conceived. Finally, and with regard to radiated scenarios, a novel formulation able to convert payload PIM specifications to a practical PIM test is proposed. This formulation consents to link the power flux densities at the device under test (DUT) with the RF power levels measured by the test bench.

Last but not least, a large class of PIM measurements carried out with the novel test bed architectures have been reported. These measurements cover several frequency ranges (C-, Ku-, K- and Ka-bands) and different PIM scenarios, both conducted (forward and backward) and radiated. The exceptional residual PIM noise floor of each test bed will be pointed out. In addition, PIM tests on an anechoic chamber facility, multi-layer insulation blankets (MLIs) and reflector mesh samples are presented, with interesting considerations about the geometry of the structure and the impact on the PIM performance of typical elements as sawing areas and rivets. Finally, a PIM study conducted for an on-board anomaly observed during the docking of the Automatic Transfer Vehicle 3 (ATV-3) to the International Space Station (ISS) is presented. Such a study consented the localization of potential PIM sources in the thermal blanket of the ATV, and led to a set of recommendations to mitigate the PIM issue for the forthcoming ATVs.

Resumen

Las cargas útiles de los satélites de telecomunicación actuales operan en entornos multiportadora, bajo una demanda continua de mayores capacidades de transmisión. Esto ha originado un aumento en los niveles de potencia de RF, en las frecuencias de trabajo, y en el número de canales transmitidos, estimulando la aparición de efectos no lineales de alta potencia, como Multipactor, Corona, térmicos y la Intermodulación Pasiva (PIM).

De entre todos los efectos anteriores, la intermodulación pasiva es el menos estudiado, o, como mínimo, el menos comprendido. Esto se debe a su carácter ampliamente no lineal y su estrecha relación con la calidad del trabajo realizado por los operarios, lo que dificulta el desarrollo de modelos capaces de predecir y explicar fielmente las degradaciones asociadas al efecto del PIM. Los términos de PIM generados en el enlace descendente, de hecho, pueden interferir a la débil señal a detectar a través del canal de recepción, amenazando por tanto la capacidad de transmisión del enlace ascendente.

Los modelos tradicionales de PIM suelen basarse en una excitación formada por dos portadoras. Aunque se trata de un caso simple pero bastante representativo, presenta en cualquier caso diferencias importantes con el escenario real multiportadora. El trabajo realizado en esta Tesis Doctoral intenta reducir estas diferencias. Para lograrlo, se realizan dos nuevas contribuciones de relevancia para las condiciones reales de operación de los satélites. En primer lugar, se ha investigado de forma teórica el papel de las fases de las portadoras en el PIM (que se desprecia para una excitación mediante dos portadoras). En segundo lugar, se ha propuesto un nuevo modelo capaz de tener en cuenta el efecto de las portadoras no contribuyentes en un cierto término de PIM, aplicando un nuevo principio de conservación de energía. Los resultados obtenidos con los dos nuevos modelos teóricos desarrollados se ajustan perfectamente a los datos experimentales.

Debido a la compleja naturaleza del PIM, la validación de los componentes de RF de las cargas útiles de los satélites se realiza exclusivamente mediante tests experimentales. Por lo tanto, la disponibilidad de bancos de medida de PIM es un tema de gran interés para la industría y las agencias espaciales. Sin embargo, el diseño de bancos de altas prestaciones es un desafío, ya que su nivel de PIM

residual debe ser bastante inferior al requerido para validar los dispositivos de RF. Para hardware embarcado en satélites, la diferencia entre el nivel de las portadoras a transmitir (enlace descendente) y la señal de RF a detectar (enlace ascendente) puede llegar a ser del orden de los 185 dBc.

En esta Tesis Doctoral se proponen unas nuevas arquitecturas integradas de bancos de medida de PIM, implementables mediante tecnología en guía de ondas. Se han desarrollado arquitecturas tanto para PIM conducido (en dirección progresiva y regresiva) como radiado. Dichas arquitecturas permiten una reducción importante del nivel de PIM residual del sistema de medida, siendo además flexibles, capaces de manejar elevados niveles de potencia, y libres de resonancias e interacciones indeseadas. Los elementos claves de estos bancos de medidas son unos multiplexores de bajo PIM, que pueden incorporar dos familias de filtros de alta potencia que admiten un elevado número de ceros de transmisión, y por tanto, capaces de proporcionar un elevado rechazo en la banda de recepción del PIM.

Los bancos de medida de PIM conducido por onda reflejada, sin embargo, están expuestos al PIM generado por la carga empleada para absorber las portadoras de alta potencia. Para resolver esta situación, se han propuesto unas nuevas cargas de bajo PIM en tecnología guiada, que han proporcionado en tests experimentales una importante reducción en el nivel de PIM residual de estos sistemas de medida. Así mismo, se ha elaborado un nuevo tipo de transiciones para mitigar el nivel de PIM generado en interconexiones que involucren a flanges estándar. Finalmente, para escenarios radiados, se ha desarrollado un nueva formulación capaz de relacionar densidades de potencia en el dispositivo bajo test con los niveles detectados en el banco de medida, y que por tanto permiten trasladar especificaciones de PIM de la carga útil al sistema de medida de PIM.

Por último, pero no por ello menos importante, se han mostrado varias campañas de medida de PIM realizadas con bancos de medida implementados acorde a la nueva arquitectura propuesta en esta Tesis Doctoral. Estas medidas cubren varios rangos de frecuencia (bandas C, Ku, K y Ka) y diferentes escenarios de medida de PIM, tanto conducido (en dirección progresiva y regresiva) como radiado. Se ha determinado, en primer lugar, el excepcional nivel de fondo de ruido de PIM logrado en cada banco de medida. Además, se han mostrado los resultados obtenidos para medidas de PIM realizadas sobre una cámara anecoica, capas aislantes multicapa (MLIs) y mallas reflectoras, obteniendo interesantes conclusiones en cuanto a la geometría de las estructuras y el impacto que tienen a nivel de PIM elementos tan típicos como los bordes serrados y los remaches. Finalmente, se muestra un estudio de PIM asociado a una anomalía observada durante el enganche del vehículo ATV-3 a la Estación Espacial Internacional (ISS). Dicho estudio ha permitido localizar una fuente de PIM significativa en la capa aislante térmica del ATV-3, dando lugar a una serie de recomendaciones para mitigar el PIM en las próximas generaciones de vehículos ATV.

Resum

Les càrregues útils dels satèl·lits de telecomunicació actuals operen en entorns multiportadora, sota una demanda contínua de majors capacitats de transmissió. Això ha originat un augment en els nivells de potència de RF, en les freqüències de treball, i en el nombre de canals transmesos, estimulant l'aparició d'efectes no lineals d'alta potència, com Multipactor, Corona, tèrmics i la Intermodulació Passiva (PIM).

D'entre tots els efectes anteriors, la intermodulació passiva és el menys estudiat, o, com a mínim, el menys comprés. Això es deu al seu caràcter àmpliament no lineal i la seua estreta relació amb la qualitat del treball realitzat pels operaris, la qual cosa dificulta el desenvolupament de models capaços de predir i explicar fidelment les degradacions associades a aquest efecte del PIM. Els termes de PIM generats en l'enllaç descendent, de fet, poden interferir al feble senyal a detectar a través del canal de recepció, amenaçant per tant la capacitat de transmissió de l'enllaç ascendent.

Els models tradicionals de PIM solen basar-se en una excitació formada per dues portadores. Encara que es tracta d'un cas simple però bastant representatiu, presenta en qualsevol cas diferències importants amb l'escenari real multiportadora. El treball realitzat en aquesta Tesi Doctoral intenta reduir aquestes diferències. Per a aconseguir-ho, es realitzen dues noves contribucions de rellevància per a les condicions reals d'operació dels satèl·lits. En primer lloc, s'ha investigat de manera teòrica el paper de les fases de les portadores en el PIM (que es menysprea per a una excitació mitjançant dues portadores). En segon lloc, s'ha proposat un nou model capaç de tindre en compte l'efecte de les portadores no contribuents en un cert terme de PIM, aplicant un nou principi de conservació d'energia. Els resultats obtinguts amb els dos nous models teòrics desenvolupats s'ajusten perfectament a les dades experimentals.

A causa de la complexa naturalesa del PIM, la validació dels components de RF de les càrregues útils dels satèl·lits es realitza exclusivament mitjançant tests experimentals. Per tant, la disponibilitat de bancs de mesura de PIM és un tema de gran interés per a la industría i les agències espacials. No obstant això, el disseny de bancs d'altes prestacions és un desafiament, ja que el seu nivell de PIM

residual ha de ser bastant inferior al requerit per a validar els dispositius de RF. Per a maquinari embarcat en satèl·lits, la diferència entre el nivell de les portadores a transmetre (enllaç descendent) i el senyal de RF a detectar (enllaç ascendent) pot arribar a ser de l'ordre dels 185 dBc.

En aquesta Tesi Doctoral es proposen unes noves arquitectures integrades de bancs de mesura de PIM, implementables mitjançant tecnologia en guia d'ones. S'han desenvolupat arquitectures tant per a PIM conduït (en direcció progressiva i regressiva) com radiat. Aquestes arquitectures permeten una reducció important del nivell de PIM residual del sistema de mesura, sent a més flexibles, capaces de manejar elevats nivells de potència, i lliures de ressonàncies i interaccions indesitjades. Els elements claus d'aquests bancs de mesures són uns multiplexors de baix PIM, que poden incorporar dues famílies de filtres d'alta potència que admeten un elevat nombre de zeros de transmissió, i per tant, capaces de proporcionar un elevat rebuig en la banda de recepció del PIM.

Els bancs de mesura de PIM conduït per ona reflectida, no obstant això, estan exposats al PIM generat per la càrrega emprada per a absorbir les portadores d'alta potència. Per a resoldre aquesta situació, s'han proposat unes noves càrregues de baix PIM en tecnologia guiada, que han proporcionat en tests experimentals una important reducció en el nivell de PIM residual d'aquests sistemes de mesura. Així mateix, s'ha elaborat un nou tipus de transicions per a mitigar el nivell de PIM generat en interconnexions que involucren a flanges estàndard. Finalment, per a escenaris radiats, s'ha desenvolupat un nova formulació capaç de relacionar densitats de potència en el dispositiu sota test amb els nivells detectats en el banc de mesura, i que per tant permeten traslladar especificacions de PIM de la càrrega útil al sistema de mesura de PIM.

Per últim, però no per això menys important, s'han mostrat diverses campanyes de mesura de PIM realitzades amb bancs de mesura implementats concorde a la nova arquitectura proposada en aquesta Tesi Doctoral. Aquestes mesures cobreixen diversos rangs de freqüència (bandes C, Ku, K i Ca) i diferents escenaris de mesura de PIM, tant conduït (en direcció progressiva i regressiva) com radiat. S'ha determinat, en primer lloc, l'excepcional nivell de fons de soroll de PIM reeixit en cada banc de mesura. A més, s'han mostrat els resultats obtinguts per a mesures de PIM realitzades sobre una cambra anecoica, capes aïllants multicapa (MLIs) i malles reflectores, obtenint interessants conclusions quant a la geometria de les estructures i l'impacte que tenen a nivell de PIM elements tan típics com les vores serrades i els reblons. Finalment, es mostra un estudi de PIM associat a una anomalia observada durant l'enganxament del vehicle ATV-3 a l'Estació Espacial Internacional (ISS). Aquest estudi ha permés localitzar una font de PIM significativa en la capa aïllant tèrmica del ATV-3, que ha donat lloc a una sèrie de recomanacions per a mitigar el PIM en les pròximes generacions de vehicles ATV.

Contents

Acronyms

AF Amplitude Factor

AIM Active Inter-Modulation

ARTES Advance Research in Telecommunication Systems

ATV Automatic Transfer Vehicle

BPF Band-Pass Filter

CAD Computer-Aided Design

CATR Compact Antenna Test Range

CW Continuous Wave

DUT Device Under Test

EM Electro-Magnetic

ESA European Space Agency

ESTEC European Space Research and Technology Centre

FFT Fast Fourier Transform

GAM Microwave Applications Group

GFRP Graphite Fiber Reinforced Plastic

GNSS Global Navigation Satellite System

HFRW Hybrid Folded Rectangular Waveguide

HMOM High Magnification Optical Microscope

HPA High Power Amplifier

HPF High-Pass Filter

HTS High Throughput Satellite

IMS International Microwave Symposium

IPR Input Power Ratio

ISS International Space Station

ITU International Telecommunication Union

LNA Low Noise Amplifier

LPF Low-Pass Filter

MHFRW Modified Hybrid Folded Rectangular Waveguide

MLI Multi-Layer Insulation

MUX Multiplexer

NF Noise Figure

OP Overall PIM Output Power

PFD Power Flux Density

PFM Proto-Flight Model

PIM Passive Inter-Modulation

PNT Power Thermal Noise Floor

RBW Resolution Bandwidth

RF Radio Frequency

SA Spectrum Analyzer

SF Slope Factor

SIR Stepped-Impedance Resonator

SSL Space Systems Loral

TDRS Tracking and Data Relay System

TE Transverse-Electric

TZ Transmission Zero

UPV	Universitat Politècnica de València
VDA	Vacuum Deposited Aluminum
VNA	Vector Network Analyzer
VSC	Val-Space Consortium

Chapter 1

Introduction

Passive Inter-Modulation (PIM) interference is a well known issue for the space industry.

This unwanted interference was historically faced since the seventies of the 20^{th} century, when Fltsatcom (US Fleet Communications Satellite) payloads were the first to suffer PIM issues at the lowest and critical PIM order, the third, during the test phase before launching. Other payloads like LES6, MARISAR (US Marine Satellite), MARECS (European Maritime Satellite) and IS-V (International communication satellite number V) also faced PIM issues at higher PIM orders during their test phases.

In all these programs, PIM caused a huge effort in the re-design of part of the payload architecture and components, with consequent noticeable slippage in the satellite schedule (1-2 years depending on the program) and increase of the program cost due to the rework and the retest involved [1–3]. Other payloads like INTELSAT V MCS did not show PIM issues in the test phase, however once in orbit the payload exhibited random noise due to PIM generation [1].

Looking at the above-mentioned programs, the common denominator of all these payloads was that they shared in the same antenna both transmission and reception channels. The problem was mitigated by re-designing the architecture of the payload by using two separated antennas for transmission and reception channels, respectively. However, this causes a significant increase in the payload dimension and weight, with consequent added cost to the missions.

Nowadays, despite some heritage and lessons learned from the past, PIM issue is still alive and represents a threat for the space industry. In fact, common satellite payloads have a high number of channels in order to improve flexibility and bandwidth usage, thus leading to a multicarrier scenario which fosters inter-modulation issues [4, 5]. The situation is even worse in modern HTS (High Throughput Satellites) operating at higher frequency bands [6, 7], on which the

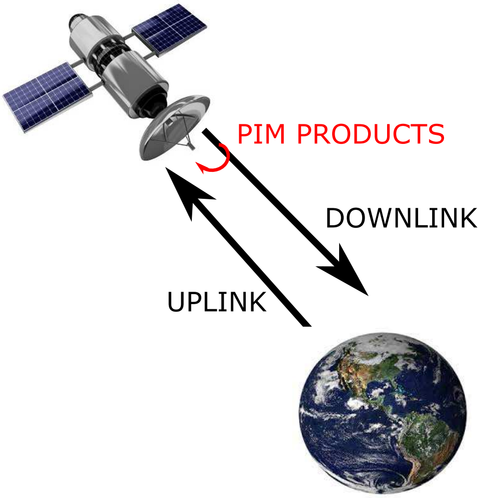

Figure 1.1: PIM products generated by on-board equipment in satellite downlink.

compact sizes of these payloads (due to the reduced wavelength), combined with the higher throughput, leads to adopt architectures which are in conflict with classical PIM mitigation techniques (basically based on splitting the reception path from the transmission one).

PIM is not the only electrical issue for modern payloads. Indeed, the employment of increased RF power levels and number of channels involved in the transmission channel (downlink) stimulates other non-linear effects in the payload, such as Multipactor, Corona and thermal issues (Power Handling) in addition to Passive Inter-Modulation (PIM) [8,9]. However, among the above-mentioned phenomena, PIM is largely the less studied, or, at least, understood. This is due to its extreme non-linear nature and strong relation with workmanship, which makes very difficult the development of models able to predict and explain PIM-related impairments.

How PIM acts in payloads?

PIM non-linearities may be critical in satellite payloads with transponders operating simultaneously in transmission (downlink) and in reception (uplink). Under this scenario, the RF multichannel transmitted signal in the downlink can generate spurious inter-modulation terms, which could interfere with the extremely weak incoming signal to be detected by the uplink RF chain of the satellite front-end, as depicted in Figure 1.1.

In a high-power scenario, this undesired effect can affect the throughput of the uplink and even cause, in extreme cases, the disruption of the reception channel.

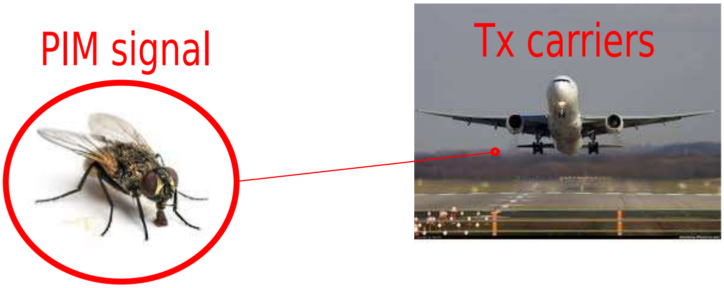

Figure 1.2: PIM interference versus transmission carriers, analogy.

For this reason PIM is a key limiting factor of satellite payload performance [10–15].

PIM quantification

A typical characteristic of PIM interference is its very weak intensity and non-destructive nature. The latter is a main difference from other high-power RF breakdown phenomena in satellite payloads, such as Multipactor and Corona effects [8].

The main focus has to be at the reception channel of the payload, because of the weak level of the signal received which can be threatened by the PIM interference.

In modern satellites the difference between the transmitted and the received RF power levels is huge, typically above 150 dBc. Thus, even low-power inter-modulation terms originated from passive components may be comparable to the received signal [12, 13, 16–19].

In order to give an analogy, the amplitude of PIM interferences respect to the transmission carriers is similar to the difference of noise between the one generated by a fly and the one generated by a modern Boeing 737 during its take-off (i.e. having the engines at their maximum power), as depicted in Figure 1.2. In other words, the same payload must be able to distinguish the buzzing of the fly, while it is emitting the sound level of an aircraft take-off at a closer transmission frequency.

In the following subsections several aspects of PIM will be treated, such as the physics associated to the phenomenon and the classical PIM models present in technical literature. An additional subsection will be dedicated to the traditional PIM set-ups employed to measure passive inter-modulation in RF laboratories. The purpose of these subsections is to provide a clear picture of the state-of-art about the PIM phenomenon, highlighting the limitations observed so far and the motivations which guides the objectives and tasks carried out during this Ph.D. thesis work.

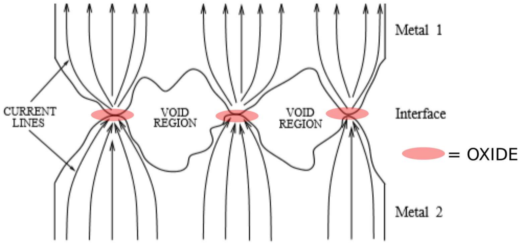

Figure 1.3: Non ideal contact, typical PIM source.

1.1 Physics of PIM

Inter-modulation distortion requires at least two carriers or signals at different frequencies [20]. As a result, PIM has to be investigated in the front-end of the payload once the high power RF channels are mixed, thus generating a multicarrier signal.

The front-end is typically composed by metallic components, such as couplers, filters, multiplexers, orthomode transducers, antennas, routing waveguides, etc. The materials employed tend to be aluminium alloys, often with a silver or golden coating of the surfaces to improve, among others characteristics, the electrical conductivity and therefore reduce insertion losses.

As a consequence, the physics of PIM was historically focused on three main branches:

- Investigate the metallic contacts at the interconnections.
- Investigate the materials involved.
- Investigate the geometry of the RF devices.

This distinction leads to classify the PIM sources into two main categories, named as PIM contact non-linearities and PIM material non-linearities [21].

Note also that multicarrier signals (typical case for satellite payloads) may generate a large number of non-linear contributions, namely harmonics and inter-modulation terms. This topic will be treated in more depth in the subsection dedicated to the PIM modeling (see Section 1.2).

PIM due to contact non-linearities

A non-ideal metal is composed by imperfections at the mating area. As a result, an ideal metal-to-metal contact is transformed in an inhomogeneous metal-oxide-metal contact, on which the layer of oxide is very thin (see sketch in Figure 1.3).

A class of diodes based on a metal-oxide-metal contact has been known and investigated for decades [22–24], thus justifying the non-linearity associated to the PIM phenomenon.

As a consequence, a metal-oxide-metal contact may be source of passive intermodulation [17], since the high power multicarrier RF signal passing through the non-ideal contact induces several effects which ignite PIM generation, such as:

- Tunnel effect at the critical contact (oxide perforation and high density currents). The oxide creates a thin barrier layer for electrons (10-1000 Angstroms [25]) not easy to cross. The electron accumulation produces a distribution of charge along the surface which leads to a potential barrier. As a consequence, the junction is not symmetrical to the current flow. Depending on the oxide layer thickness (thus on the pressure at the contact area) and the voltage applied, there is a finite electron probability that the electrons cross the oxide, which implies that the current is non-linear function of the voltage (as in a Schottky's diode) [26–28].
- Thermionic emission at the critical contact (oxide perforation). This phenomenon is associated to the emission of 'hot' electrons from the metal. As the temperature increases due to the RF signal, the electrons accumulated at the contact surface gain energy. When the energy is high enough, the electrons may move a short distance off the surface so crossing the oxide layer gap (emission) [28, 29].
- Micro-discharges at the critical area. This phenomenon is also known as 'filamental conduction' and it is attributed to microscopic filaments (whiskers). These whiskers, due to the high electron density accumulated, may ignite a micro-discharge and/or an exceptional tunnelling effect in case the filaments are covered with a thin oxide layer [25].
- Non-linearities associated to metallic debris (contamination) at the critical contact. Materials, if not properly cleaned from contaminants (e.g. Kevlar), may present strong PIM non-linearity [25].
- Loose contacts at the mating areas. If the mating pressure at the flanges/RF connectors is not properly applied and the contact is loose, high levels of PIM may be observed [30].
- Poor workmanship and finishing of the surfaces at the contact area. Different contact junctions, having theoretically the same design, may show very different measured PIM performance [26, 31].
- Temperature gradient (both due to external environment or due to the applied RF power). Thermal effects due to the RF power dissipation may cause a non-linear variation on metal conductivity [32].

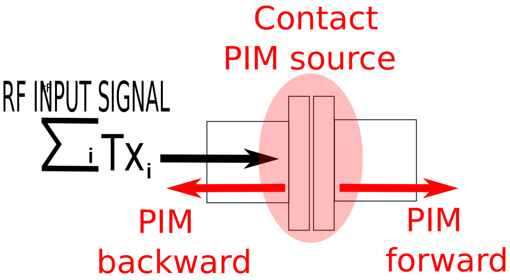

Figure 1.4: Non ideal contact, contact PIM source in waveguide technology.

- Surface abrasion (roughness) at the contact area [26, 33]. It was demonstrated that conductor abrasions which are orthogonal to the direction of the surface currents tend to produce stronger PIM terms than the longitudinal ones (10 dB difference or more). This happens for different class of materials such as pure aluminium, aluminium alloy 6061, copper and beryllium copper.

- Skin effect related to coating thickness. Many metal coatings over aluminium use nickel as prime material to limit galvanic corrosion. Nickel has been proved as a strong PIM source due to its intrinsic ferromagnetic nature, thus the thickness of the coating has to be enough to avoid that the RF field reaches the nickel. For silver plating, it has been demonstrated that a coating of around 8 times the skin-depth is enough to avoid PIM ignition [33, 34]. Since the skin-depth is frequency-dependent, PIM tends to be more critical at lower frequencies for a given thickness [35]. For reflector antennas based on graphite fiber reinforced plastic (GFRP), a classical treatment to improve the polarization purity is through vacuum deposited aluminium (VDA) surface coating, however this solution was demonstrated to be prone to stimulate PIM [25].

PIM contact non-linearities are the most common ones in waveguide technology, typically associated to the flanged connection among different RF components that, for the architecture of the payload, have to be mated. The same type of non-linearity is present in coaxial technology, typically located at the coaxial male-to-female connection. A sketch of a typical PIM contact in waveguide technology is depicted in Figure 1.4.

The PIM interference, once ignited, is isotropic. The PIM component that travels in the same direction of the RF signal is named forward PIM, whereas backward PIM travels in the opposite direction.

Loose flanges have been observed to be a strong PIM source [30]. The design of dedicated waveguide flanges able to distribute the pressure homogeneously along the contact region (and, if present, able to break the oxide layer at the contact) can be useful to mitigate PIM [18, 25].

For coaxial technology, similar considerations are valid and particular care must be taken in the application of the correct torque at the connectors. In addition, PIM is particularly sensible to the mating-demating mechanism at the connector interfaces, which should be minimized. Indeed, it was observed that repeated mate-demates cause a degradation of PIM performance, due to abrasion and the deposition of metallic debris at the mated area.

The way the device is split in parts for manufacturing and assembly also plays a fundamental role in the PIM generation. Geometries allowing to manufacture the devices under test in one-piece are preferred, when possible, to minimize PIM generation [25]. If a monolithic solution is not a suitable option in terms of manufacturing, geometries which ensure minimal or very low electrical current across the contact interface between the device parts, have been demonstrated to diminish internal PIM generation.

In rectangular waveguide technology for fundamental mode excitation, symmetrical in width structures have a negligible surface density current through the symmetry plane. As a result, they can be split in two identical halves with a cut in the broad side of the guide, referred as a clam-shell assembly, without a significant PIM generation [36]. For antenna reflectors based on graphite fiber reinforced plastic (GFRP) the same guidelines are valid: geometries having the fibers oriented parallel to the incoming electric field vector (and thus not cutting the electric field) demonstrate a clear benefit in terms of PIM mitigation [25].

Moving parts in a device, related to a loose electrical metal contact, are also a relevant source of PIM. In addition to coaxial connectors, tuning elements are a clear example. Geometries involving tuning elements provides much higher PIM levels than tuning-less devices [12]. This also explains the poor PIM performance observed in flexible waveguides, where the flex parts tend to stimulate PIM generation [30].

For radiator elements as Multi-Layer Insulation (MLI) and reflector mesh surfaces, the presence of irregularities in the structure like sawing areas, borders or metallic rivets can be a strong source of PIM contact non-linearity [25, 37, 38]. The PIM igniting mechanism is associated to an inhomogeneous pressure contact at those areas, when compared with the nearby environment. In addition, these critical areas can suffer a deposit of metallic debris due to the machining. If the debris is not properly removed, a relevant source of PIM is created.

PIM due to material non-linearities

The characteristics of the materials interacting with the RF electromagnetic fields are also of relevance to the level of PIM generated.

Ferromagnetic materials have been seen to be prone to generate relatively high PIM terms, due to their inherent non-linear behaviour and hysteresis [13,30,39,40]. As a result, some metallic materials can be significant PIM sources. High PIM contribution was measured for cold-rolled steel and nickel [41], associated to their intrinsic non-linear ferromagnetic permeability. Also graphite was shown prone to produce PIM terms, in this case as a consequence of its non-linear resistivity [41].

Conductors like aluminium, brass, copper, and beryllium-copper are all related with low PIM contributions [41]. PIM non-linearity of non-magnetic stainless steel was also measured, but it was shown to have worse PIM contributions (about 10 to 15 dB higher) than the above-mentioned good conductors [41].

Besides the intrinsic PIM performances, some metals may generate PIM source in the interconnects. This is the case of aluminium, which is prone to generate a poorly-conductive oxide layer when exposed to air. This characteristic of oxide deposition links material non-linearities to contact non-linearities, since the part exposed to air are typically the ones to be mated [16]. Corrosion of metal surfaces is indeed a relevant cause of PIM interference, due to the generation of a metal-oxide-metal junction [11, 42, 43]. On the other hand, noble materials like silver and gold show good PIM performance also in the interconnects, because their exposition with air generate a conductive sulphide layer which does not add a significant PIM contribution. Moreover, this layer can be easily penetrated with a lower contact pressure [18, 36, 44].

Alocrom 1200 also deserves a particular note. It is a typical surface treatment employed in space sector to enhance the corrosion resistance of aluminium and aluminium-alloys, as well as to improve the multipactor performance of RF devices. Alocrom-treated material showed to have a small impact in PIM degradation when compared with aluminium [33]. However, when the same material is employed in contact junctions, it has been measured as a strong PIM source [33].

In addition, mixing different materials in a contact area is not a good idea in terms of PIM mitigation. First, the galvanic reaction between both materials will cause a long-term corrosion that stimulates PIM [45]. In addition, the different thermal expansion coefficients will bring a variation on the contact area pressure when exposed to RF signals and/or thermal cycles, thus fostering PIM generation.

1.2 PIM modeling

In agreement with the physics of PIM, a PIM source can be characterized by a metal-thin oxide-metal contact. As a result, the PIM source acts as a Schottky's diode, where the relationship between the input and the output signal is non-linear.

The classical model to describe this behaviour is a pure polynomial expansion of a two-carriers excitation, having both tones the same amplitude [13, 19, 20, 26, 44, 46].

This reduced model is easier to analyze and requires less effort for testing, whilst being quite representative of the real multicarrier scenario normally composed of several channels with similar amplitude levels. Thus, the input signal expressed

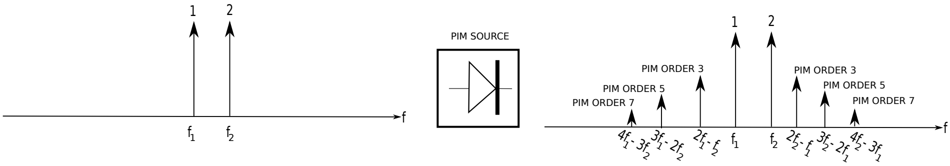

Figure 1.5: PIM terms from a two-carriers excitation in the frequency domain. It can be observed that only some particular odd order PIM terms fall at frequencies close to the transmission carriers.

in voltage terms can be modeled as:

$$V_{\text{in}}(t) = A\cos(\omega_1 t) + A\cos(\omega_2 t) \tag{1.1}$$

Due to the non-linear behaviour of the PIM source, the output voltage can be expressed as a polynomial expansion of the input voltage, where a large number of contributions is generated:

$$V_{\text{out}}(t) = \alpha V_{\text{in}}(t) + \beta V_{\text{in}}^2(t) + \gamma V_{\text{in}}^3(t) + \delta V_{\text{in}}^4(t) + ... \tag{1.2}$$

so that the exponentiation generates different non-linear orders as follows: second order PIM for βV_{in}^2, third order PIM for γV_{in}^3, and so on. The first term, corresponding to αV_{in} is the linear term.

If we expand each PIM order term and analyze $V_{\text{out}}(t)$ in the frequency domain, the noising caused by passive inter-modulation can be clearly seen (see Figure 1.5). Indeed, PIM is composed by several contributions, each one falling at a different frequency [13]. In addition, it can be noticed that the odd orders of inter-modulation may fall at spurious frequencies close to the carriers, whereas the even ones and the harmonics are very far from the transmission channels. Since the reception and transmission channels of a system are normally relatively close (in order to share the same antenna and antenna components, using a single transceiver), odd PIM terms tend to be the most critical ones for satellite payloads, as they can fall at the reception frequency band, interfering the weak received signal [13].

It is easy to verify that the frequency of an inter-modulation term is linked to the main non-linear order generating such an undesired contribution. For a two-carriers case, the relationship is the following one:

$$f_{\text{PIM}} = |\pm m_i f_1 \pm n_j f_2| \tag{1.3}$$

$$\text{PIM}_{\text{order}} = m_i + n_j \tag{1.4}$$

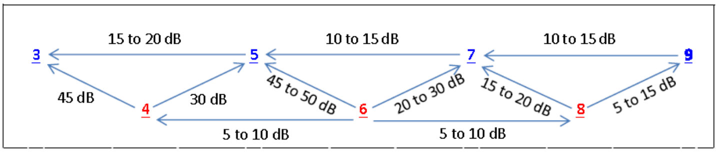

Figure 1.6: PIM order relationship, from [47].

where m_i and n_j are positive integers associated to f_1 and f_2, respectively. Theoretically, an increase of 1 dB in the amplitude of the input carriers cause an increase of $m_i + n_j$ dB in the non-linear term.

Another characteristic of PIM is that the amplitude is not the same for all the orders. In fact, PIM intensity fades as the PIM order grows [13, 47, 48]. Moreover, it was demonstrated in real test scenarios that odd PIM orders tend to be stronger than the even ones, at least for similar PIM orders [47] (see Figure 1.6).

Among the odd orders, the third order PIM is therefore the strongest and the one falling closest to the corresponding transmission carriers, thus being assumed to be the most critical one [13, 16–18, 25]. In fact, some systems increase the separation between transmission and reception bands to avoid that third order PIM terms of the transmission channel may fall into the reception band. In such a case, the fifth or even the seventh order terms should be the limiting ones. An example is the Ka-band channelization for satellite links [6, 49].

Further, it was investigated in technical literature the PIM dependence versus the amplitude of the carriers involved. Despite typical payload architectures consider a multicarrier operation on which all signals deliver the same amount of RF power, measurements of the third order PIM contribution with two tones having different amplitudes have been conducted [17]. The PIM has been shown to be slightly dependent on the amplitude of the carriers, and the worst case is the one which follows the m/n rule (i.e. if we consider the term $2f_2 - f_1$, the maximum will be when the power associated to f_2 is twice the one associated to f_1). Nevertheless, the difference between the maximum PIM detected and the one having both carriers at the same amplitude can be considered negligible (less than 1 dB) [17]. For this reason the case with equal carriers amplitude will be the baseline for the work considered in this thesis. This also represents the most usual situation in practice (all channels with similar amplitudes) and in testing [46].

Another characteristic of PIM, largely analyzed in technical literature, is the dependence of the PIM term power with the input signal power. Looking at the polynomial expansion, for each dB of increase in the transmission carriers power, an n-th order PIM term power should present an increase of n dB, thus resulting in a slope factor equal to n (i.e., an increase of n dB/1 dB). However, measurements conducted for several PIM orders and at different bandwidths showed that this dependence is significantly lower [13, 47, 50]. In addition, it was observed that the PIM power dependence between successive PIM orders are roughly the same, thus an increase of the input power into the system should increase the PIM contributions roughly by the same factor [48, 51].

Mathematical models able to explain this reduction in the slope factor for the third order PIM (the most critical one) have been presented, on which the PIM source was modeled as a series connection of a linear resistance plus a non-linear resistance [52]. The effect of higher-order non-linear terms has also been used to partly explain this discrepancy (at the third-order PIM term frequency, five-order non-linear terms may also fall, which may be in opposite phase, and theoretically have a higher increase rate with power) [53].

Besides the analytical models, recently a much more complex behavioural model based on a non-analytic theory has been published [51]. Such a model was formulated under the small signal assumption for a two-carriers scenario, showing good agreement for third and fifth PIM orders once adjusted to real PIM measurements conducted in laboratory.

It is evident that the classical polynomial expansion of only two input carriers may not be fully representative of the real multicarrier scenario. The number of non-linear terms increases exponentially with the number of carriers. Even for a third-order non-linearity, the PIM contributions at frequencies of the form $f_i \pm f_j \pm f_k$ are not considered in the two-carrier model. As it will be shown in Section 2.1, the two-carrier model can be extended for a higher number of carriers. However, even in the general case, a particular PIM term only depends on the frequencies involved in its generation. Namely, the PIM term at $2f_2 - f_1$ should depend only on the amplitude of the contributions at f_1 and f_2, and should be independent from the input carriers at f_3, f_4, etc. However, real measurements at payload level belies this assumption. In an empirical and thorough study recently published [50], it was demonstrated that the presence of additional carriers in the mainstream decreases the power of particular PIM tones which should not be affected. The work in [50], which is plenty of useful data, does not provide however an explanation for such a PIM reduction effect.

As it can be pointed out, the theoretical model based on the polynomial expansion of the input signal is able to provide insights for the non-linear PIM contributions. However, it exhibits relevant discrepancies with the experimental results, such as the smaller slope factor for the PIM power dependence, and the effect of non-contributing carriers on theoretically unrelated PIM terms. Therefore, more research is requested in this area to develop improved non-linear models able to characterize the real effects observed in experimental campaigns. In the same vein, an analysis on how the carrier phases affects to the power of the PIM terms can also be of interest. Although this effect has been shown to be irrelevant for standard PIM tests carried out with two high-power carriers, it could play a role in a more general multicarrier scenario.

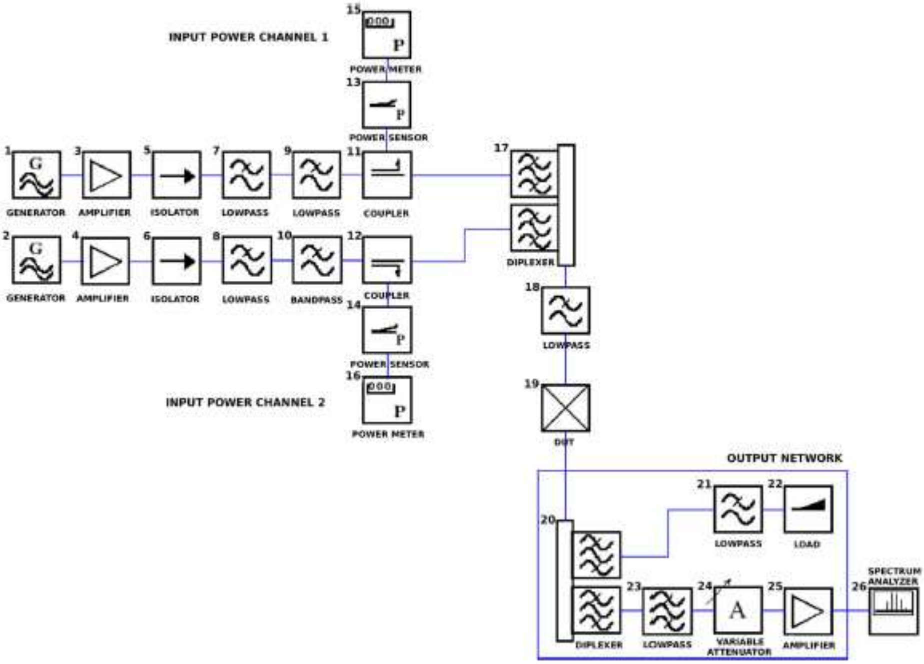

Figure 1.7: Classical PIM set-up for a conducted scenario, composed by a cascade of elements (from [18]).

1.3 PIM testing

The most common way to conduct a validation of RF devices is entrusted to testing, due to the intrincated nature and very complex modeling of PIM phenomena [54]. As a result, the availability of low PIM test set-ups is of great interest for industry and space agencies, because in many cases they are the only way to validate the PIM performance of satellite payloads. The importance of PIM testing can also be extended to other applications limited by PIM interferences, such as cellular telecommunications systems [53, 55, 56].

The design of low PIM test benches, however, is very challenging, since the components involved in the set-up can also be a PIM source. Obviously, the intrinsic residual PIM (noise floor) of the set-up has to be well below the level requested to validate the required PIM performance for the test devices. To give a rule of thumb, PIM specifications for telecom and military payloads can be as low as -130/-135 dBm whilst the satellite delivers 100 W CW/carrier (or, equivalently, 50 dBm). Therefore, the dynamic margin is as huge as 180/185 dBc, and the residual noise of the low PIM measurement system must be 5-10 dB lower, as a minimum.

Classical low PIM test set-ups are based on a cascade of several RF devices, such as multiplexers, couplers, cables and so on [13, 17, 18, 25, 57–59], both for coaxial and waveguide technologies. A schematic of a classical PIM test bench, extracted from [18], is provided in Figure 1.7.

This solution presents several drawbacks. The presence of several blocks leads to a degradation of the overall return loss of the bench. Also, the overall insertion loss of the measurement system is not negligible, as it suffers an accumulation of losses of the involved elements. In addition, the high number of interconnections may add potential PIM sources, able to degrade the overall PIM performances of the bench [59, 60]. Furthermore, these benches lack flexibility, since they are designed only for a particular scenario composed by two input channels and one specific $|m| \pm |n|$ PIM term. The latter can be critical for testing laboratories supporting several classes of space programs, since each program may require a dedicated set-up with consequent added cost for the associated design, manufacturing and assembling.

As far as radiated set-up concerns, the same drawback given by the connection in cascade of several devices is present. This can be particularly critical if the test benches are designed to combine the carriers before their radiation towards the device under test (e.g. multi-layer insulations (MLIs), deployable meshes, thermal blankets, to cite a few).

Typical radiated test beds combine the transmission carriers through a manifold and radiate the signal through a single antenna, being the PIM signal collected by a sniffer antenna [47, 61]. A classical PIM test bench for a radiated scenario, extracted from [47], is shown in Figure 1.8. Some other test beds omit the manifold, radiating each carrier independently towards the device under test through dedicated antennas, and collecting the backward PIM signal by an additional antenna.

Both solutions, however, are prone to measurement errors/instabilities due to the coupling factor between the different antennas involved in the set-up [47].

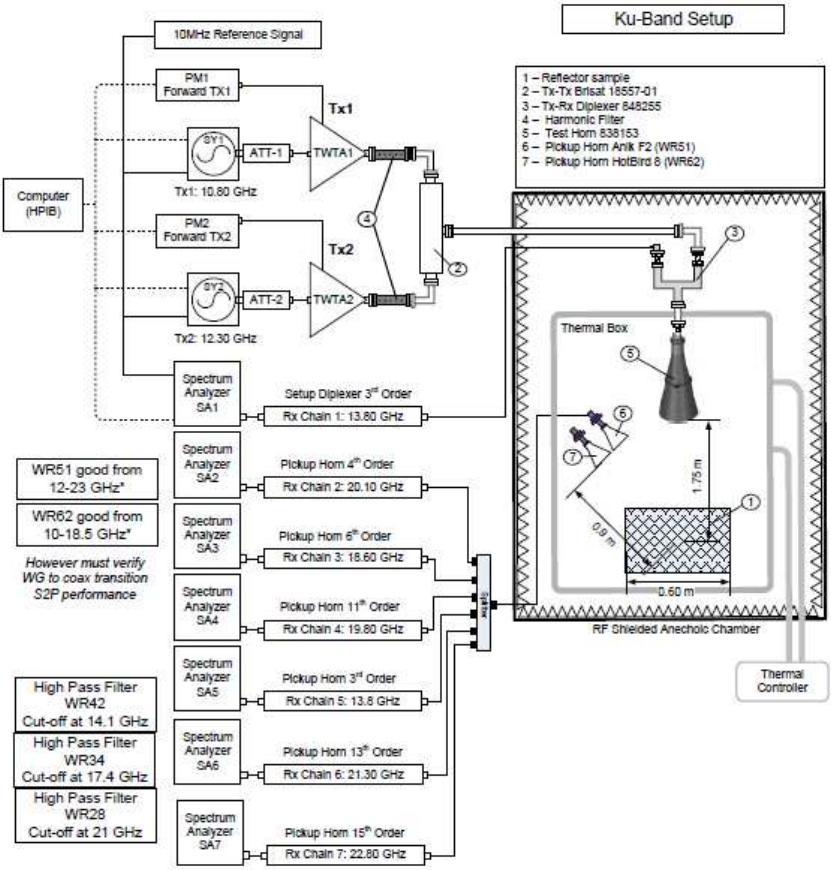

Figure 1.8: Classical PIM set-up for a radiated scenario, from [47].

1.4 Objectives

The aim of this Ph.D. thesis work is to provide a step forward in several aspects related to PIM, both theoretically and experimentally.

From a theoretical point of view, it would be useful to expand the traditional polynomial model from a two-carriers excitation to a general multicarrier excitation. Given the complexity of the calculations for a high number of carriers and several non-linear orders, the availability of a mathematical closed expression able to provide all the PIM contributions can also be of help for a wide range of applications.

Although PIM generates non-linear terms of several orders, the most critical ones in practice are normally those related to third order contributions [13, 16, 44, 47]. As a result, most of the work carried out in this thesis will be focused on third order PIM terms.

The effect of the phase of the carriers in PIM will be also investigated. In addition to the practical use of carriers with different phases (for instance, in a quadrature or phase modulation), this effect is also worth of consideration due to the drift of the high power amplifiers (HPAs) employed for the RF power amplification of the signals. It would be of interest to find out when the phases of the carriers are relevant in third order PIM contributions, and try to quantify its effect in the level of the undesired PIM term. It is expected that the phase of the carriers will be of relevance in multicarriers scenarios, in contrast to the two-carriers case normally used for testing.

Multicarriers scenarios also involve the presence of non-contributing carriers (i.e. carriers not directly involved in the PIM term under analysis). In contrast to theoretical models, experimental results have shown that the number of non-contributing carriers play a role in the level of the PIM signal. As a result, an additional objective of this thesis work is identifying a simple model able to explain the effects observed in the plentiful and detailed set of data reported in [50]. Another goal for the multicarriers case consists on establishing the link between the real multicarriers scenario and the typical one for testing, which is limited to two-carriers excitation (due to the increase in equipment cost and assembly complexity). The development of expressions to estimate the PIM level in a multicarriers scenario from measurements performed in the two-carriers case would be extremely useful for practical applications.

With regard to the experimental point of view, this thesis is aimed at developing a new class of highly-performing low PIM test set-ups. To avoid the limitations of classic test beds, the new ones should share the following guidelines: integrated and compact solutions, on which the number of mechanical connections is squeezed to its limit, thus avoiding potential contact PIM sources. This kind of solutions would also have a better return loss characteristics than a cascade connection of several devices, avoiding also spurious resonances typical of filter connections in cascade. The insertion losses should also be kept low, being this a benefit since the set-up will not suffer overheating issues. In addition, the filters implemented should be tuning-less (since tuning elements are typically strong PIM sources) and with relatively wide passband bandwidths (6-8% for each channel) to consent to cover several PIM orders and frequencies, thus giving a degree of flexibility much higher than classical low PIM assemblies [13,18]. The proposed solutions must be flexible also in terms of scenarios, namely, the same low PIM assembly should be suitable for both conducted and radiated PIM tests.

As far as conducted scenario concerns, both backward PIM and forward PIM test beds will be considered [54]. Each test bed topology and architecture will be chosen depending on the channel frequencies and PIM orders involved. A wide range of PIM measurements will be conducted, demonstrating the benefits of having flexible and highly performing low PIM set-ups. In addition, an effort will be done in developing a new methodology to design low PIM terminations in waveguide technology for measuring conducted PIM, an essential point to reduce the residual noise floor of low PIM set-ups for detecting backward PIM at C- and higher frequency bands.

On the other hand, radiated PIM set-ups are able to measure the power delivered to the transmission antenna(s) and the one provided by the receiver antenna. However, in terms of electromagnetic characterization, it would be more useful to determine the ratio between the PIM power flux density emitted from the DUT and the one incident to the DUT corresponding to the transmitted carriers.

1.5 Thesis structure

The thesis is organized in six chapters. This first chapter provides an overview of the passive inter-modulation topic, highlighting the paramount importance of the PIM issue for the space industry. Next, the main physics concepts behind the ignition of the PIM phenomenon are described. Then, a state-of-art, both for modeling and testing, is given, on which the limitations and drawbacks of the actual solutions are stressed out. The objectives which have guided this work are also presented. The goal of this chapter is providing the reader a perspective into the strategic value of new models and test set-ups, which will allow to describe and measure more efficiently the PIM non-linearity in passive microwave components.

Chapter 2 is focused on the improvement of the available theoretical models describing the passive inter-modulation. First, a full polynomial expression which compacts the PIM formulation for a generic multicarriers scenario and PIM order contribution is derived. Next, the effect of the carrier phase on the PIM contributions will be analyzed. For a two-carriers excitation it will be shown that the average PIM power does not depend on the carrier phases. However, for a more general case (i.e. multicarrier excitation), it will be proved that the measured PIM level may fluctuate if two different PIM contributions fall at the same frequency. Finally, a new model will be also presented; which is able to estimate, from a two-carriers standard test, the third order PIM behaviour (the most critical one in real tests) in a multicarrier scenario with non-contributing carriers.

In Chapter 3, novel low PIM measurement set-up architectures will be presented. The proposed solutions will cover the conducted scenario, both for forward and reflected PIM, as well as the radiated scenario. The advantages of the new class of test benches when compared with classical solution will be spotted, as well as the resulting drawbacks. In addition, guidelines to choose the best configuration will be detailed, depending on the nature of the scenario, PIM order and signal frequencies. Backward set-up architectures are highly exposed to residual PIM level generated by the dummy load used for dissipating the high-power carriers. In order to solve this issue, a simple way to design waveguide terminations having low passive inter-modulation properties will be described and experimentally verified. Finally, some useful expressions will be derived to transform the PIM level measured at the receiver antenna in radiated scenarios into the PIM flux density radiated by the DUT.

Chapter 4 is focused on describing the filter topologies for low PIM test beds, in order to get the extremely high rejections required for both the transmission and the reception channels. In particular, for the transmission channels, two novel topologies are employed, called respectively Hybrid Folded Rectangular Waveguide (HFRW) and Modified Hybrid Folded Rectangular Waveguide (MHFRW), which consent the placement of a high number of independently tunable transmission zeros in the PIM band. In the reception (PIM) band, given the different requirements (wider channel but with less demanding rejection), more traditional solutions based on a combination of a band-pass filter plus a high-pass/low-pass sections are employed. In addition, an output diplexer designed for K/Ka bands, able to separate the conducted forward PIM from the transmission carriers, will be presented.

Chapter 5 is dedicated to real PIM measurements. The PIM performances of several test beds designed following the novel architectures introduced in Chapter 3 will be described. Both conducted PIM (forward and backward) as well as radiated PIM examples will be treated at several frequency bands. The residual PIM level of the facilities will demonstrate an outstanding dynamic range between carriers and PIM of about 190/210 dBc. In addition, an interesting investigation carried out as a consequence of one on-board anomaly during the docking between the Automatic Transfer Vehicle 003 (ATV-003) and the International Space Station (ISS) will be described, showing probable PIM ignition factors which were prevented for the subsequent launch of the ATV-004.

Chapter 6 summarizes the conclusions of this work and analyzes the goals attained. Likewise, it describes potential future research and development lines associated with the work performed in the framework of this thesis work.

Chapter 2

New models for passive inter-modulation

This chapter describes new theoretical models developed along this Ph.D. thesis work for PIM characterization. First, a polynomial model for passive inter-modulation under a generic multicarrier excitation is developed, thus obtaining general mathematical expressions. Using this model, the role of the carrier phases is analyzed. The phases of the carriers have been traditionally set to zero in PIM, as they do not affect to the measured PIM level in the classic two-carriers case. In this chapter, however, it is proved that the value of the phases is of high relevance when more than one PIM term fall at the same frequency. In fact, this may be a typical situation for practical multicarrier scenarios composed of several equally-spaced channels. Using the proposed theoretical model, the PIM variation due to the effect of the carrier phases is evaluated, providing closed expressions for the cases where several PIM contributions coincide at the same frequency.

On the other hand, and in contrast to classic models, practical results show that the presence of non-contributing carriers tends to reduce the PIM level of theoretically unrelated PIM terms. In the last section of this chapter, a theoretical model has been developed able to represent this effect. This method assumes that the overall PIM power for a given order only depends on the amount of power at the system input, in a similar way that the output power of an amplifier is mainly governed by the overall input power, providing a excellent agreement with available experimental data. The resulting expressions also allow to link the standard two-carrier case with a generic multicarrier scenario.

The developed models have been mainly applied for 3^{rd} order PIM contributions, as it represents the worst-case in terms of PIM amplitude and is normally the limiting case in practice. The theoretical results are compared with software and experimental data, fully validating the proposed models.

2.1 General polynomial model

Let us consider a general non-linear system whose voltage output, $V_{\text{out}}(t)$, can be expressed in terms of its input voltage, $V_{\text{in}}(t)$, in the form:

$$V_{\text{out}}(t) = C + \alpha V_{\text{in}}(t) + \beta V_{\text{in}}^{2}(t) + \gamma V_{\text{in}}^{3}(t) + \delta V_{\text{in}}^{4}(t) + \epsilon V_{\text{in}}^{5}(t) + \ldots \tag{2.1}$$

where $V_{\text{in}}^{p}(t)$ generates the p-th order non-linear contributions (namely, the ones which increase p dB for an increase of 1 dB in the input signal amplitude). Since Passive Inter-Modulation (PIM) is a non-linear effect, this term produces all the p-th order PIM contributions.

To the author's knowledge, it lacks a general expression for a particular N-th order non-linear contribution in the case of an excitation composed of an arbitrary number M of carriers. Only some particular cases have been considered in the technical literature, most of them corresponding to the two-carriers case [13, 16, 26, 62].

In a general way, for a generic scenario composed by the sum of M carriers we have:

$$V_{\text{in}}(t) = \sum_{m=1}^{M} A_m \cos(\omega_m t + \Phi_m) = \sum_{m=1}^{M} c_m \tag{2.2}$$

where c_m expresses, in a compact form, the time varying m-th input carrier.

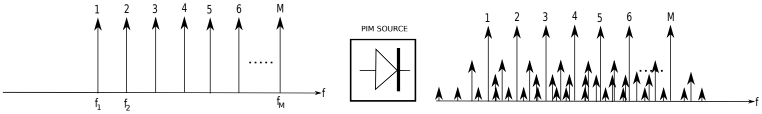

Figure 2.1: PIM order relationship for an M-carriers scenario, frequency domain. Each carrier is assumed to be a tone.

Let us obtain the closed form expression for $V_{\text{in}}^{N}(t)$ in (2.1) for a generic M-carriers excitation case (see Fig. 2.1). For the standard two-carriers scenario, $M = 2$, with carriers x and y to simplify the notation, the N^{th} order PIM terms can be expressed as:

$$V_{\text{in}}^{N} = (x+y)^{N} = \sum_{i=0}^{N} \binom{N}{i} x^{i} y^{N-i} = \sum_{i=0}^{N} \frac{N!}{i!\,(N-i)!} x^{i} y^{N-i} \tag{2.3}$$

Analogously, for a three-carriers scenario ($M = 3$), being x, y and z the carriers, we would obtain:

$$\begin{aligned} V_{in}^N &= (x+y+z)^N = (x+(y+z))^N = \sum_{i=0}^{N}\binom{N}{i}x^i(y+z)^{N-i} = \\ &= \sum_{i=0}^{N}\binom{N}{i}x^i\left[\sum_{j=0}^{N-i}\binom{N-i}{j}y^j z^{N-i-j}\right] = \\ &= \sum_{i=0}^{N}\sum_{j=0}^{N-i}\frac{N!}{i!j!\,(N-i-j)!}x^i y^j z^{N-i-j} = \sum_{i+j+k=N}\frac{N!}{i!j!k!}x^i y^j z^k \end{aligned} \tag{2.4}$$

where the last series represent all the possible combinations for the integer numbers i, j and k whose summation is equal to N.

Applying induction rules, the expression for the general case can be extracted:

$$V_{\text{in}}^N = \left(\sum_{m=1}^{M} c_m\right)^N = \sum_{i_1+i_2+\ldots+i_M=N}\frac{N!}{i_1!i_2!\ldots i_M!}c_1^{i_1}c_2^{i_2}\ldots c_M^{i_M} \tag{2.5}$$

and substituting c_m by its corresponding carrier (see (2.2)), we obtain the final closed expression:

$$V_{\text{in}}^N(t) = \sum_{i_1+i_2+\ldots+i_M=N}\frac{N!}{i_1!i_2!\ldots i_M!}\prod_{j=1}^{M}\left[A_j\cos\left(\omega_j t+\Phi_j\right)\right]^{i_j} \tag{2.6}$$

Equation (2.6) expresses the general polynomial expansion for the N^{th} order PIM terms in a given multicarrier scenario composed of M carriers. The trigonometric rules to express a product of cosine functions into a summation may be used next to separate the contributions at each particular frequency.

Example: Third order PIM (N=3) in multicarrier scenario (M carriers)

Since the summation of the carrier indexes must be equal to the PIM order $N = 3$, the general expression (2.6) may have three types of potential terms.

Term 1: one carrier index equal to 3 and the remaining set to 0.

Let us suppose $i_p = 3$ and the remaining indexes equal to 0, for a generic p. The resulting term for $V_{\text{in}}^3(t)$ will take the form:

$$\frac{3!}{3!0!\ldots0!}\left[A_p\cos\left(\omega_p t+\Phi_p\right)\right]^3 = A_p^3\left[\frac{3}{4}\cos(\omega_p t+\Phi_p)+\frac{1}{4}\cos(3\omega_p t+3\Phi_p)\right] \tag{2.7}$$

Term 2: one carrier index equal to 2, other equal to 1 and the remaining set to 0.

Let us suppose $i_p = 2$, $i_q = 1$, and the remaining indexes equal to 0, for generic p and q indexes $(p \neq q)$. The corresponding term for $V_{\text{in}}^3(t)$ is:

$$\begin{aligned}\frac{3!}{2!1!0!...0!}\left[A_p\cos\left(\omega_p t+\Phi_p\right)\right]^2 A_q\cos\left(\omega_q t+\Phi_q\right) =&\\ A_p^2A_q\left[\frac{3}{4}\cos((2\omega_p+\omega_q)t+(2\Phi_p+\Phi_q))+\right.&\\ \left.\frac{3}{4}\cos((2\omega_p-\omega_q)t+(2\Phi_p-\Phi_q))+\frac{3}{2}\cos(\omega_q t+\Phi_q)\right]&\end{aligned} \tag{2.8}$$

Term 3: three carrier indexes equal to 1, and the remaining set to 0.

Let us suppose $i_p = 1$, $i_q = 1$, $i_r = 1$, and the remaining indexes equal to 0, for generic p, q and r indexes $(p \neq q \neq r)$. The related term for $V_{\text{in}}^3(t)$ can be expressed as:

$$\begin{aligned}\frac{3!}{1!1!1!0!...0!}A_p\cos\left(\omega_p t+\Phi_p\right)A_q\cos\left(\omega_q t+\Phi_q\right)A_r\cos\left(\omega_r t+\Phi_r\right) =&\\ A_pA_qA_r\left[\frac{3}{2}\cos((\omega_p+\omega_q+\omega_r)t+(\Phi_p+\Phi_q+\Phi_r))+\right.&\\ \frac{3}{2}\cos((\omega_p+\omega_q-\omega_r)t+(\Phi_p+\Phi_q-\Phi_r))+&\\ \frac{3}{2}\cos((\omega_p-\omega_q+\omega_r)t+(\Phi_p-\Phi_q+\Phi_r))+&\\ \left.\frac{3}{2}\cos((\omega_p-\omega_q-\omega_r)t+(\Phi_p-\Phi_q-\Phi_r))\right]&\end{aligned} \tag{2.9}$$

After aggregating all the possible terms, the spectrum corresponding to the 3rd order PIM contributions can be easily obtained.

2.2 The effect of the carrier phase in passive intermodulation

In passive inter-modulation studies with an excitation formed by continuous wave (CW) tones, the effect of the carrier phase has been traditionally neglected. It has been observed experimentally that, for the standard PIM test based on two equal-amplitude input tones [46], the PIM term, when present, is independent from the carrier phases. In fact, its measured level is kept over time despite the phase drift which may suffer the High Power Amplifiers (HPAs) due to their heating-up. This has leaded to forgive the effect of the phase in the modeling for a two-carriers PIM scenario, which is assumed to be zero on both carriers for the sake of simplicity. This same assumption can also be considered for multicarrier models assuming that the carrier frequencies are chosen in such a way that each PIM contribution falls at a different frequency [50].

However, should the phase of the carriers always be neglected in PIM? What happens in multicarrier scenarios where different PIM terms fall at the same frequency? This section aims at covering this actual gap, which, at the author's knowledge, has not been treated in the technical literature so far.

In this section, for 3rd order PIM, the two-carriers scenario (the typical one for testing) will be considered first, and then a generic multicarrier case will be deeply analyzed. The theoretical results will be verified, for some particular cases, using the multicarrier facility available at the ESA-VSC European High Power RF Space Laboratory.

2.2.1 PIM phase effect in a two-carriers scenario

For a classic excitation composed by two generic input carriers having each one a different time-varying phase:

$$\begin{aligned} V_{\text{in}-1}(t) &= A_1 \cos(\omega_1 t + \Phi_1(t)) \\ V_{\text{in}-2}(t) &= A_2 \cos(\omega_2 t + \Phi_2(t)) \end{aligned} \tag{2.10}$$

on a non-linear system with only 3rd order PIM contribution:

$$V_{\text{out}}(t) = C + \alpha V_{\text{in}} + \gamma V_{\text{in}}^3 \tag{2.11}$$

the ignited PIM will be composed of terms of the forms (2.7) and (2.8) at frequencies ω_1, ω_2, $3\omega_1$, $3\omega_2$, $2\omega_1 \pm \omega_2$ and $2\omega_2 \pm \omega_1$. In practice, the third order PIM contributions are usually the limiting ones in terms of non-linear distortion due to their higher amplitude levels.

Let us focus on the PIM term at $2\omega_2 - \omega_1$, which tends to be most problematic one in many satellite payloads due to its closeness to the carrier frequencies. According to (2.6), (2.8), (2.10) and (2.11), the voltage associated to this PIM contribution will be:

$$V_{3-2}(t) = \gamma \frac{3}{4} A_1 A_2^2 \cos\left[(2\omega_2 - \omega_1)\, t + 2\Phi_2(t) - \Phi_1(t)\right] \tag{2.12}$$

where the sub-index $3-2$ denotes the third order contribution for a two-carriers scenario.

The mean power associated to this term (i.e., what is measured by the spectrum analyzer) will be related to the average value (E function) of the square of the voltage divided by the impedance of the system Z_0:

$$\begin{aligned} P_{3-2}(t) &= E\left\{\frac{|V_{3-2}(t)|^2}{Z_0}\right\} \\ &= \left(\frac{3}{4}\right)^2 \frac{\left(\gamma A_1 A_2^2\right)^2}{Z_0} \frac{1}{T}\int_0^T \cos^2\left[(2\omega_2-\omega_1)t + 2\Phi_2(t) - \Phi_1(t)\right] \mathrm{d}t \end{aligned} \tag{2.13}$$

For continuous wave signals, the phases of the carriers vary extremely slowly when compared with the RF signal. As a result, in a typical integration period T the phases barely change and can be considered as constants, namely $\Phi_1(t) = \Phi_1$ and $\Phi_2(t) = \Phi_2$, thus obtaining

$$P_{3-2}(t) = \left(\frac{3}{4}\right)^2 \frac{\left(\gamma A_1 A_2^2\right)^2}{Z_0} \frac{1}{T}\int_0^T \cos^2\left[(2\omega_2-\omega_1)t + 2\Phi_2 - \Phi_1\right] \mathrm{d}t \tag{2.14}$$

and, for an integration period T which covers several cycles of the PIM frequency $\omega_{\text{PIM}} = 2\omega_2 - \omega_1$ to get an average value regardless of the integration starting and ending point (as already happens in a spectrum analyzer measurement), we obtain:

$$P_{3-2}(t) = \left(\frac{3}{4}\right)^2 \frac{\left(\gamma A_1 A_2^2\right)^2}{2Z_0} \tag{2.15}$$

As it can be observed in (2.15), the power associated to this particular PIM term is independent from the value of the phase of each carrier, demonstrating that in a two-tones scenario the phase of each carrier does not play a significant role in the measured level of the inter-modulation term. This effect will be confirmed in the practical PIM measurements with two-carriers excitation shown in Section 2.2.3.

2.2.2 PIM phase effect in a generic multicarrier scenario

The effect of the phase of the carriers has been demonstrated not to play a role in classic two-tones tests. This is due to the fact that only one PIM contribution can

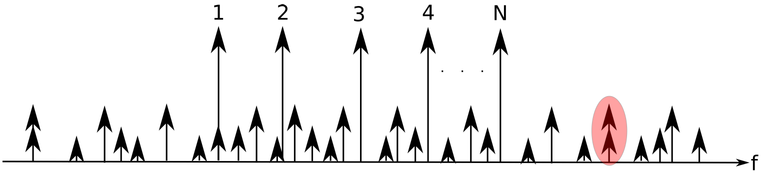

Figure 2.2: Multicarrier scenario in which two different PIM tones fall at the same frequency.

fall at each problematic frequency. This is the case for 3rd order PIM under two-carriers excitation at the frequencies $2\omega_1 \pm \omega_2$ and $2\omega_2 \pm \omega_1$. The same assumption of phase-independence is still valid in a generic multicarrier scenario, under the assumption that the carriers are chosen in such a way that at a given frequency only falls one PIM term. This is the case considered in the large set of measurements conducted at Space Systems Loral (SSL) facilities reported in [50], and the non-contributing carrier model developed in Section 2.3 [63].

But what happens if at a given frequency falls more than one PIM contribution (see Fig. 2.2)? Are the carrier phases playing a role this time?

For two different 3rd order PIM terms with different amplitudes and phases beating at the same PIM frequency ω_{PIM}, the overall PIM contribution at this particular frequency can be modeled as:

$$\begin{aligned} V_{\mathrm{PIM}}(t) &= A_{\mathrm{PIM},1}\cos(\omega_{\mathrm{PIM}}t + \Phi_{\mathrm{PIM},1}) + A_{\mathrm{PIM},2}\cos(\omega_{\mathrm{PIM}}t + \Phi_{\mathrm{PIM},2}) \\ &= \Re\left\{\left(A_{\mathrm{PIM},1}e^{\mathrm{j}\Phi_{\mathrm{PIM},1}} + A_{\mathrm{PIM},2}e^{\mathrm{j}\Phi_{\mathrm{PIM},2}}\right)e^{\mathrm{j}\omega_{\mathrm{PIM}}t}\right\} \end{aligned} \tag{2.16}$$

being $A_{\mathrm{PIM},i}$, $\Phi_{\mathrm{PIM},i}$ and ω_{PIM} real numbers. Note that the phase of the carriers are assumed to have a very slow time variation and, therefore, are treated as constants. The associated mean PIM power at ω_{PIM} is:

$$\begin{aligned} P_{\mathrm{PIM}} &= \frac{1}{2Z_0}\left|A_{\mathrm{PIM},1}e^{\mathrm{j}\Phi_{\mathrm{PIM},1}} + A_{\mathrm{PIM},2}e^{\mathrm{j}\Phi_{\mathrm{PIM},2}}\right|^2 \\ &= \frac{\left|A_{\mathrm{PIM},1}\right|^2}{2Z_0}\left|1 + \frac{A_{\mathrm{PIM},2}}{A_{\mathrm{PIM},1}}e^{\mathrm{j}(\Phi_{\mathrm{PIM},2}-\Phi_{\mathrm{PIM},1})}\right|^2 \\ &= \frac{A_{\mathrm{PIM},1}^2}{2Z_0}\left(1 + \left(\frac{A_{\mathrm{PIM},2}}{A_{\mathrm{PIM},1}}\right)^2 + 2\left(\frac{A_{\mathrm{PIM},2}}{A_{\mathrm{PIM},1}}\right)\cos\left(\Phi_{\mathrm{PIM},2} - \Phi_{\mathrm{PIM},1}\right)\right) \\ &= \frac{1}{2Z_0}\left(A_{\mathrm{PIM},1}^2 + A_{\mathrm{PIM},2}^2 + 2A_{\mathrm{PIM},1}A_{\mathrm{PIM},2}\cos\left(\Phi_{\mathrm{PIM},2} - \Phi_{\mathrm{PIM},1}\right)\right) \end{aligned} \tag{2.17}$$

or, in logarithm terms:

$$P_{\mathrm{PIM}}\ (\mathrm{dBm}) \propto 10\log_{10}\left(A_{\mathrm{PIM},1}^2 + A_{\mathrm{PIM},2}^2 + 2A_{\mathrm{PIM},1}A_{\mathrm{PIM},2}\cos\left(\Phi_{\mathrm{PIM},2} - \Phi_{\mathrm{PIM},1}\right)\right) \tag{2.18}$$

Note that the phase difference between both carriers, $\Delta\Phi_{2,1} = \Phi_{\mathrm{PIM},2} - \Phi_{\mathrm{PIM},1}$, has a relevant effect on the mean power level of the overall PIM at ω_{PIM}. The maximum value is obtained when both PIM contributions are in phase, resulting in a voltage summation ($P_{\mathrm{PIM}} \propto (A_{\mathrm{PIM},1} + A_{\mathrm{PIM},2})^2$). This is the worst situation in terms of PIM. On the contrary, if both PIM terms are in opposite phase, they tend to subtract leading to a PIM power level $\propto |A_{\mathrm{PIM},1} - A_{\mathrm{PIM},2}|^2$. Table 2.1 represents the fluctuation that can be observed in the PIM power level at ω_{PIM} compared with the case where only the first contribution (of amplitude $A_{\mathrm{PIM},1}$

$A_{\mathbf{PIM},2}/A_{\mathbf{PIM},1}$	**Max. power**	**Min. power**	**Fluctuation range**
0	0 dB	0 dB	0 dB
1/10	+0.83 dB	−0.92 dB	1.74 dB
1/4	+1.94 dB	−2.50 dB	4.44 dB
1/2	+3.52 dB	−6.02 dB	9.54 dB
1	+6.02 dB	$-\infty$ dB	∞ dB
2	+9.54 dB	0 dB	9.54 dB
4	+13.98 dB	+9.54 dB	4.44 dB
10	+20.83 dB	+19.08 dB	1.74 dB

Table 2.1: Influence of the carrier phases for two PIM terms falling at the same frequency. The maximum and minimum power is obtained when both contributions are in-phase and in opposite phase, respectively.

and phase $\Phi_{\mathrm{PIM},1}$) is present. As it can be observed, a variation in the carrier phases (including a slow variation) may cause a severe fluctuation in the PIM level reading.

The expressions (2.16) and (2.17) can be easily generalized for the case of P PIM contributions falling at the same angular frequency ω_{PIM}, obtaining:

$$V_{\mathrm{PIM}}(t) = \Re\left\{\sum_{i=1}^{P}\left(A_{\mathrm{PIM},i}e^{\mathrm{j}\Phi_{\mathrm{PIM},i}}\right)e^{\mathrm{j}\omega_{\mathrm{PIM}}t}\right\} \tag{2.19}$$

and:

$$P_{\mathrm{PIM}} = \frac{1}{2Z_0}\left(\sum_{i=1}^{P}\left[A_{\mathrm{PIM},i}^2 + \sum_{j=i+1}^{P} 2A_{\mathrm{PIM},i}A_{\mathrm{PIM},j}\cos\left(\Phi_{\mathrm{PIM},j} - \Phi_{\mathrm{PIM},i}\right)\right]\right) \tag{2.20}$$

Equation (2.20) indicates that when several PIM tones beat at the same frequency, depending on the phase of the carriers, their overall contribution may fluctuate between the worst case of all PIM tones in phase (and therefore added in voltage terms) and the best case of the PIM terms combined in such a way the PIM amplitude is minimized.

Since the amplitude of the PIM terms decays with the PIM order [13,25,47,50], the higher fluctuation is normally observed when several PIM terms of the same or very similar orders fall at the same frequency. In the next section, some examples are considered and verified with software or experimental data.

2.2.3 Application examples

Example 1: three equally-spaced carriers of the same amplitude

Let us consider the case of three carriers of the same amplitude A and placed at equally-spaced frequencies f_1, $f_2 = f_1 + \Delta f$, $f_3 = f_1 + 2\Delta f$. For this case, it is easy to prove that two third-order PIM contributions are falling at the frequency $f_{\mathrm{PIM}} = f_1 + 3\Delta f$, namely:

$$\begin{aligned} &\text{PIM Term 1: } f_3 + f_2 - f_1 = f_1 + 2\Delta f + (f_1 + \Delta f) - f_1 = f_1 + 3\Delta f \\ &\text{PIM Term 2: } 2f_3 - f_2 = 2\,(f_1 + 2\Delta f) - (f_1 + \Delta f) = f_1 + 3\Delta f \end{aligned} \tag{2.21}$$

whose voltages, according to (2.9) and (2.8), are given by:

$$\begin{aligned} V_{\mathrm{PIM},1}(t) &= \frac{3\gamma A^3}{2}\cos\left(2\pi f_{\mathrm{PIM}} t + \Phi_3 + \Phi_2 - \Phi_1\right) \\ V_{\mathrm{PIM},2}(t) &= \frac{3\gamma A^3}{4}\cos\left(2\pi f_{\mathrm{PIM}} t + 2\Phi_3 - \Phi_2\right) \end{aligned} \tag{2.22}$$

Applying (2.20), or its particular case (2.17), the overall PIM mean power at f_{PIM} is:

$$\begin{aligned} P_{\mathrm{PIM}} &= \frac{\left(\gamma A^3\right)^2}{2Z_0}\left(\frac{3}{2}\right)^2\left(1 + \frac{1}{4} + \cos\left(\Phi_3 - 2\Phi_2 + \Phi_1\right)\right) \\ &= P_{\mathrm{PIM},1}\left(1 + \frac{1}{4} + \cos\left(\Phi_{\mathrm{PIM},2} - \Phi_{\mathrm{PIM},1}\right)\right) \end{aligned} \tag{2.23}$$

which has a range of variation of 9.54 dB between $9P_{\mathrm{PIM},1}/4$ (+3.52 dB) and $P_{\mathrm{PIM},1}/4$ (−6.02 dB) depending on the difference of phase between the involved PIM terms, $\Phi_{\mathrm{PIM},2} - \Phi_{\mathrm{PIM},1} = \Phi_3 - 2\Phi_2 + \Phi_1$, as corresponds to the case in Table 2.1 in which the lower-amplitude PIM term is half the amplitude of the higher PIM term.

The effect of phase on PIM was checked by a simple software code implemented in Matlab [64]. The user can define the number M of carriers, their frequencies, the PIM order N of interest and the PIM frequency under analysis. For each carrier, a loop in phase is carried out in steps of 10°. For each phase combination of the carriers, the N^{th} order non-linear contribution is computed in the time domain, and a Fast Fourier Transform (FFT) is applied in order to move to the frequency domain [65]. Finally, at the PIM frequency under analysis, the power associated to the N^{th} order PIM contribution is computed. The software returns the maximum and the minimum values obtained (for the worst and best combinations of the carrier phases), and the difference between both values is expressed in logarithm scale. The resulting value is the PIM fluctuation range due to the effect of the phases of the carriers.

A few application examples of the software and their comparison with the model derived in this section are provided in Table 2.2 and Fig. 2.3. As it can be seen, for the case where the carrier frequencies are set to $f_1 = 1$ GHz, $f_2 = 1.2$ GHz and $f_3 = 1.4$ GHz, being $f_{\mathrm{PIM}} = 1.6$ GHz, a variation of 9.54 dB is observed according to the previous theoretical calculations. For all the other cases, only one PIM term falls at $f_{\mathrm{PIM}} = 1.6$ GHz (the one corresponding to $2f_3 - f_2$), so the PIM level is predicted to be constant regardless of the phase of the carriers.

f_1 **[GHz]**	f_2 **[GHz]**	f_3 **[GHz]**	f_4 **[GHz]**	f_5 **[GHz]**	$f_{\mathbf{PIM}}$ **[GHz]**	**PIM order**	**Fluctuation** **Model [dB]**	**Software [dB]**
1.0	1.2	1.4	-	-	1.6	3	9.54	9.54 Fig. 2.3(a)
1.02	1.2	1.4	-	-	1.6	3	0	0 Fig. 2.3(b)
1.02	1.2	1.4	1.43		1.6	3	0	0 Fig. 2.3(c)
1.02	1.2	1.4	1.43	1.452	1.6	3	0	0 Fig. 2.3(d)

Table 2.2: Comparison between theoretical and predicted (software) PIM fluctuation ranges in terms of the carrier phases for selected 3$^{\text{rd}}$ order PIM scenarios.

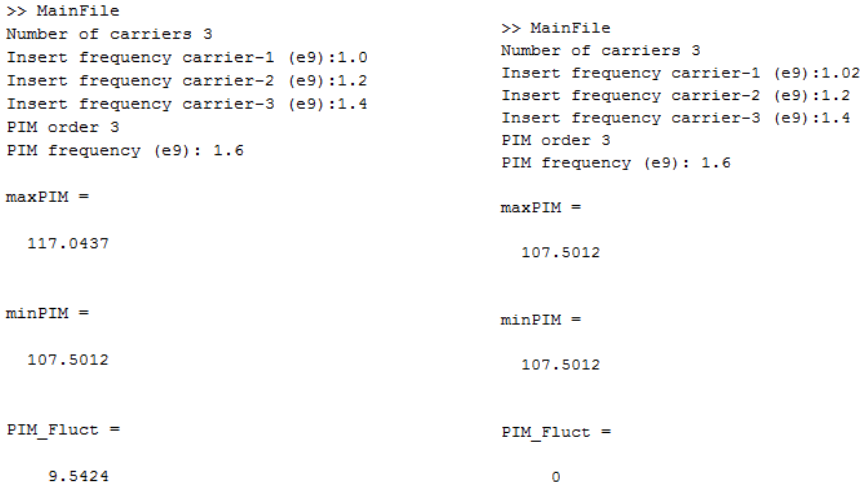

```
>> MainFile
Number of carriers 3
Insert frequency carrier-1 (e9):1.0
Insert frequency carrier-2 (e9):1.2
Insert frequency carrier-3 (e9):1.4
PIM order 3
PIM frequency (e9): 1.6

maxPIM =

  117.0437


minPIM =

  107.5012


PIM_Fluct =

    9.5424
```

(a) Case 1

```
>> MainFile
Number of carriers 3
Insert frequency carrier-1 (e9):1.02
Insert frequency carrier-2 (e9):1.2
Insert frequency carrier-3 (e9):1.4
PIM order 3
PIM frequency (e9): 1.6

maxPIM =

  107.5012


minPIM =

  107.5012


PIM_Fluct =

     0
```

(b) Case 2

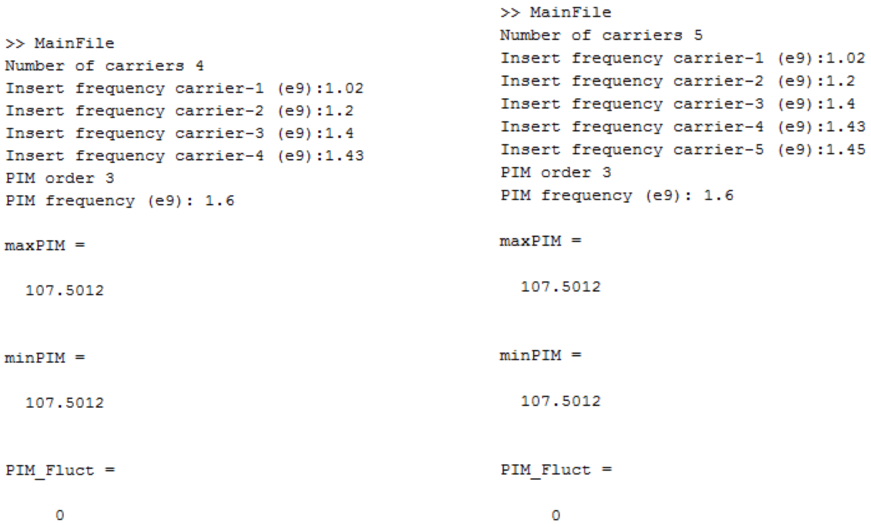

```
>> MainFile
Number of carriers 4
Insert frequency carrier-1 (e9):1.02
Insert frequency carrier-2 (e9):1.2
Insert frequency carrier-3 (e9):1.4
Insert frequency carrier-4 (e9):1.43
PIM order 3
PIM frequency (e9): 1.6

maxPIM =

  107.5012


minPIM =

  107.5012


PIM_Fluct =

     0
```

(c) Case 3

```
>> MainFile
Number of carriers 5
Insert frequency carrier-1 (e9):1.02
Insert frequency carrier-2 (e9):1.2
Insert frequency carrier-3 (e9):1.4
Insert frequency carrier-4 (e9):1.43
Insert frequency carrier-5 (e9):1.45
PIM order 3
PIM frequency (e9): 1.6

maxPIM =

  107.5012


minPIM =

  107.5012


PIM_Fluct =

     0
```

(d) Case 4

Figure 2.3: Software runs for the examples detailed in Table 2.2.

Example 2: four non equally-spaced carriers of the same amplitude

Let us consider next the case of four carriers of same amplitude A and non equally-spaced frequencies f_1, f_2, f_3 and f_4. Let us suppose first that $f_4 = f_3 + (f_2 - f_1)/2$. In this scenario, there are two third-order PIM contributions of the same amplitude coinciding at the frequency $f_{\mathrm{PIM}} = 2f_3 - f_1$, since $2f_4 - f_2 = 2f_3 + f_2 - f_1 - f_2 = 2f_3 - f_1$. For this case, both PIM terms have the form provided by (2.8):

$$\begin{aligned} V_{\mathrm{PIM},1}(t) &= \frac{3\gamma A^3}{4}\cos\left(2\pi f_{\mathrm{PIM}} t + 2\Phi_3 - \Phi_1\right) \\ V_{\mathrm{PIM},2}(t) &= \frac{3\gamma A^3}{4}\cos\left(2\pi f_{\mathrm{PIM}} t + 2\Phi_4 - \Phi_2\right) \end{aligned} \tag{2.24}$$

From (2.20), the overall mean power of the PIM term at f_{PIM} can be expressed in closed form as:

$$\begin{aligned} P_{\mathrm{PIM}} &= \frac{\left(\gamma A^3\right)^2}{2Z_0}\left(\frac{3}{4}\right)^2\left(1 + 1 + 2\cos\left(\Phi_{\mathrm{PIM},2} - \Phi_{\mathrm{PIM},1}\right)\right) \\ &= 4P_{\mathrm{PIM},i}\cos^2\left(\frac{\Phi_{\mathrm{PIM},2} - \Phi_{\mathrm{PIM},1}}{2}\right) \end{aligned} \tag{2.25}$$

so that, depending on the phase difference $\Phi_{\mathrm{PIM},2} - \Phi_{\mathrm{PIM},1} = 2\left(\Phi_4 - \Phi_3\right) - \Phi_2 + \Phi_1$, the amplitude of the overall PIM component at f_{PIM} can be increased in 6 dB with respect to the level corresponding to only one of the contributions (in-phase terms) or even disappear (opposite-phase terms).

A different situation is obtained if the frequency f_4 is set to be equal to $f_3 + f_2 - f_1$. Under such circumstances, the two PIM terms at $f_4 + f_3 - f_1$ and $2f_4 - f_2$ falls at the same frequency f_{PIM}. These PIM terms can be expressed according to (2.9) and (2.8), respectively, thus obtaining:

$$\begin{aligned} V_{\mathrm{PIM},1}(t) &= \frac{3\gamma A^3}{2}\cos\left(2\pi f_{\mathrm{PIM}} t + \Phi_4 + \Phi_3 - \Phi_1\right) \\ V_{\mathrm{PIM},2}(t) &= \frac{3\gamma A^3}{4}\cos\left(2\pi f_{\mathrm{PIM}} t + 2\Phi_4 - \Phi_2\right) \end{aligned} \tag{2.26}$$

providing a mean power of the overall PIM component at f_{PIM}:

$$\begin{aligned} P_{\mathrm{PIM}} &= \frac{\left(\gamma A^3\right)^2}{2Z_0}\left(\frac{3}{2}\right)^2\left(1 + \frac{1}{4} + \cos\left(\Phi_4 - \Phi_3 - \Phi_2 + \Phi_1\right)\right) \\ &= P_{\mathrm{PIM},1}\left(1 + \frac{1}{4} + \cos\left(\Phi_{\mathrm{PIM},2} - \Phi_{\mathrm{PIM},1}\right)\right) \end{aligned} \tag{2.27}$$

resulting in a similar situation to the one of the example 1 with three carriers, with a PIM fluctuation (due to phase effect) of 9.54 dB between $9P_{\mathrm{PIM},1}/4$ (+3.52 dB with respect to $P_{\mathrm{PIM},1}$) and $P_{\mathrm{PIM},1}/4$ (-6.02 dB with respect to $P_{\mathrm{PIM},1}$).

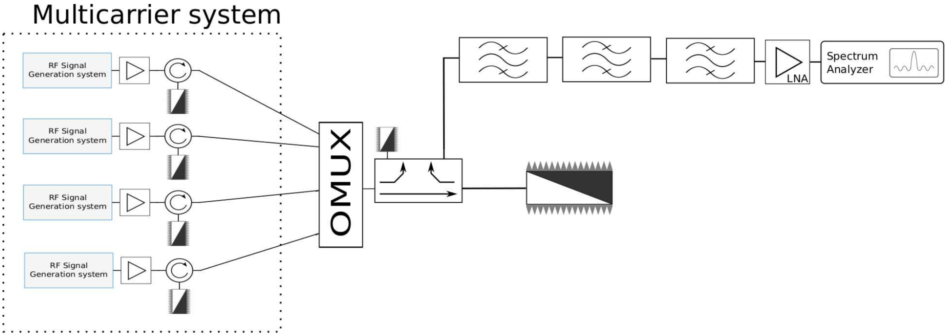

Figure 2.4: Schematic of the PIM measurement set-up based on the multicarrier facility, able to combine up to four high-power carriers at once.

Carriers				**PIM**	
f_1 **[GHz]**	f_2 **[GHz]**	f_3 **[GHz]**	f_4 **[GHz]**	**order**	f_{PIM} **[GHz]**
10.7135	10.8125	11.1095	11.2085	3	11.6045

Table 2.3: 3^{rd} order PIM fluctuation due to carrier phase variation in unequal amplitude PIM terms, test scenario.

These two cases with four carriers have been checked experimentally by conducting practical measurements in Ku-band, thanks to the multicarrier facility available at the ESA-VSC European High Power RF Space Laboratory. This facility has been adapted for third order (the most critical one) PIM measurements. Up to four continuous-wave (CW) carriers of 50 dBm each were employed at once. A schematic of the test bed is depicted in Fig. 2.4, where four carriers are combined by an output multiplexer, and injected into a load acting as a PIM source. The reflected PIM contribution is routed by a directional coupler to a filter bank and, after being amplified, is detected using an spectrum analyzer. Figure 2.5 shows some photographies of the assembled test set-up.

Two test scenarios with four carriers of the same amplitude were considered. In each scenario, the carriers were switched ON or OFF depending on the particular PIM measurement carried out.

Test scenario 1

The first test scenario is detailed in Table 2.3, and corresponds to a case where f_4 is set to be equal to $f_3 + f_2 - f_1$, so that the PIM terms at $f_4 + f_3 - f_1$ and $2f_4 - f_2$ falls at the same frequency $f_{\mathrm{PIM}} = 11.6045$ GHz. As shown in (2.26), theoretically, the PIM term amplitude at $2f_4 - f_2$ is half of the value for the term at $f_4 + f_3 - f_1$.

(a) Front View - Signal generators and HPAs.

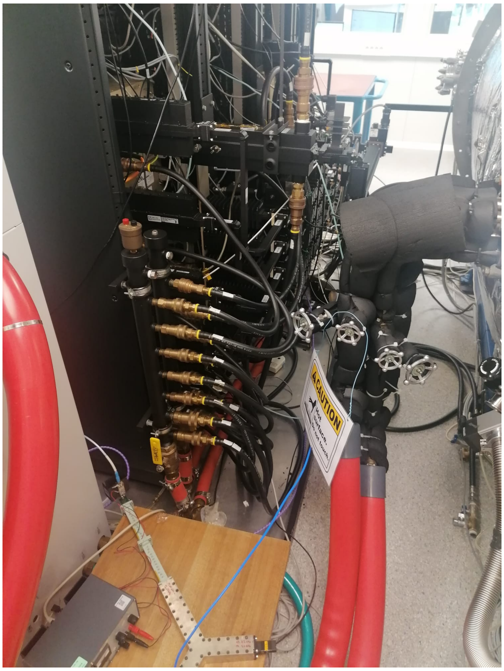

(b) Rear view - Multiplexer and PIM filters.

Figure 2.5: Assembled PIM set-up based on the multicarrier facility.

Carriers				**PIM**			**Notes**
f_1	f_2	f_3	f_4	**PIM term**	**Max**	**Min**	
-	✓ 0° – 360°	-	✓	$2f_4 - f_2$	-138.2	-138.4	constant
✓	-	✓	✓ 0° – 360°	$f_4 + f_3 - f_1$	-133.3	-133.5	constant
✓	✓ 0° – 360°	✓	✓	$f_4 + f_3 - f_1$ $2f_4 - f_2$	-130.2	-139.5	9.3 dB variation

Table 2.4: 3^{rd} order PIM fluctuation due to carrier phase variation in unequal amplitude PIM terms, experimental results.

As shown in Table 2.4, several tests were performed activating two, three or the four carriers. For each test, the phase of one of the carriers (as detailed in Table 2.4) was swept from 0° to 360°, and the highest and lowest detected PIM levels were recorded. For the first two tests, only one PIM term falls at f_{PIM}. Therefore, and according to the expression (2.15) derived in Section 2.2.1, the PIM power was not affected by the phase variation of the carriers. Note also how the level of the term corresponding to the mixing of three carriers (i.e., $f_4 + f_3 - f_1$) is around 6 dB higher than the one associated to mixing two carriers (i.e., $2f_4 - f_2$), as (2.8) and (2.9) predict. The small discrepancy can be attributed to small differences in the amplitude of the carriers at the DUT plane or inaccuracies in the PIM set-up (errors in PIM readings of about ±1 dB are not uncommon). On the other hand, for the third test case, where two PIM terms were beating at the same frequency, the phase variation in one of the carriers caused a fluctuation of the PIM level between $+3.2$ dB (worst case) and -6.1 dB (best case) when compared with the isolated PIM term at $f_4 + f_3 - f_1$, resulting in an overall variation of 9.3 dB. These results are in full agreement with the ones theoretically predicted in this section and also compiled in Table 2.1 (see the case where the ratio between the amplitudes of the second and first PIM terms is equal to 1/2).

Test scenario 2

In the second test scenario, detailed in Table 2.5, f_4 is equal to $f_3 + (f_2 - f_1)/2$, so that the PIM terms at $2f_3 - f_1$ and $2f_4 - f_2$ coincide in frequency.

Carriers				**PIM**	
f_1 **[GHz]**	f_2 **[GHz]**	f_3 **[GHz]**	f_4 **[GHz]**	**order**	f_{PIM} **[GHz]**
10.8125	11.0105	11.1095	11.2085	3	11.6045

Table 2.5: 3^{rd} order PIM fluctuation due to carrier phase variation in equal amplitude PIM terms, test scenario.

Carriers				**PIM**			**Notes**
f_1	f_2	f_3	f_4	**PIM term**	**Max**	**Min**	
-	✓ 0° – 360°	-	✓	$2f_4 - f_2$	-138.0	-138.0	constant
✓	✓ 0° – 360°	✓	✓	$2f_4 - f_2$ $2f_3 - f_1$	-132.2	≤ -150 (*)	≥ 17.8 dB variation (*)

(*) -150 dBm was the residual noise floor of the PIM facility

Table 2.6: 3^{rd} order PIM fluctuation due to carrier phase variation in equal amplitude PIM terms, experimental results.

This scenario corresponds to the four-carriers case analyzed in this section, where both PIM terms falling at the same PIM frequency have the same amplitude, as shown in (2.24). As a result, its combination can provide a PIM power increase of +6 dB or a total cancellation when compared to the presence of only one of the PIM terms. The experimental results are shown in Table 2.6, and are again in-line with the theoretical predictions. Note that the noise floor of the test facility was -150 dBm, so that only a reduction of 18 dB in the PIM term (with respect to the situation where only one PIM term falls at the PIM frequency) could be effectively measured.

In the last two cases under consideration, the experimental data have fully validated the theoretical model. As a result, the phase of the carriers must be carefully taken into account in PIM scenarios where several PIM terms coincide at the same frequency (an usual situation, in practice, in systems with several channels equally-spaced in frequency). This is a significant difference with the standard two-carriers scenario [46], where the measured PIM level is essentially independent from the carrier phases, and has leaded to neglecting the effect of such phases in PIM evaluation.

2.3 Effect of non-contributing carriers in PIM

In technical literature, classic models usually approach the passive inter-modulation issue through a limited two-carriers scenario. The mathematics used to describe the non-linear effects are based on a pure polynomial expansion (Taylor's series) of a two-carriers excitation [13–15]. This traditional model has been outlined in Section 1.2, and has been summarized through the general expressions (1.1)-(1.4).

The extension of this classical polynomial model for a multicarrier scenario (real case in practice for the space industry), implies that each PIM product should only depend on the carriers which contribute to its generation. These carriers are the so-called "contributing carriers". The power dependence of a PIM product with the power level of its contributing carriers has been widely studied, particularly for the most critical 3^{rd} order PIM contribution [13, 17, 47, 50, 52].

In the same way, and according to classic models, the amplitude of a given PIM term should not be modified by the presence of other carriers which are not directly involved in its generation. These other carriers are commonly labelled as “non-contributing carriers”, as they should not contribute to the power of the PIM term under analysis. To give an example, if we consider a generic five-carriers scenario and we focus on the third order PIM term placed at the angular frequency $2\omega_2 - \omega_1$, such a term should depend only on the amplitude of the input carriers at ω_1 and ω_2, and be independent from the amplitudes of the input carriers at angular frequencies ω_3, ω_4 and ω_5.

Practical PIM measurements conducted under multicarrier scenarios, however, bely this assumption. As a matter of fact, it was observed that the presence of non-contributing carriers affects the power of the PIM tone under analysis, which tends to decrease as the number of non-contributing carriers grows.

In particular, a detailed study on this topic was carried out by Space Systems Loral (SSL), one of the most important satellite payload manufacturers worldwide, which was recently published in [50]. Such an exhaustive work was conducted at payload level and under the utmost care in the choice of the non-contributing carriers frequencies, so that the active inter-modulation terms generated by the carriers mixing at the high power amplifiers (HPAs) do not fall at the frequency of the PIM tone. Reference [50], despite of being plenty of useful practical data, is however unable to offer an explanation for the power level reduction of the PIM term due to the increase of the number of non-contributing carriers.

The author has developed an innovative model able to provide a justification for this behaviour, which cannot be explained by traditional theories. This novel model is based on an energy conservation assumption, until now never considered in the technical literature. The assumption states that the overall PIM power for a PIM order under consideration only depends on the overall input power at the PIM source. In other words, considered a given PIM order at a given PIM source, the new model assumes that the total amount of PIM power generated is nearly constant if the overall input power at the PIM source is kept constant, regardless the number of carriers involved.

The developed model neglects interactions between successive PIM orders, and is only focused in 3^{rd} order PIM, the most critical one in practice [66, 67]. This assumption is justified by two empirical reasons observed in real laboratory measurements:

a. The power difference between consecutive PIM orders is considerable. In particular, the contribution of the 3^{rd} order PIM is at least 13 dB higher than for successive PIM orders [13, 25, 47, 51]. As a consequence, after focusing on the 3^{rd} order, contributions from successive PIM orders may be neglected as a first-order approach.

b. The power slopes of consecutive PIM orders (i.e., the power increase rate of a PIM contribution in terms of the increase rate in the input power) are roughly the same [13, 47, 48, 51]. Thus, after injecting more power into the system in a multicarrier scenario, the ratio between successive PIM orders will be nearly kept.

For the sake of simplicity, the proposed model assumes that all carriers have equal-amplitude and zero phase. The equal-amplitude assumption is representative of the real scenario for payloads (it is indeed the scenario for the measurements reported in [50]), and it is also the classic scenario considered for standard PIM testing [46]. On the other hand, the zero-phase assumption for all carriers does not affect the PIM outcome, as it is assumed that similarly to [50], the carrier frequencies are chosen in order to avoid more than one PIM contribution falling at the same frequency (see Sections 2.2.1 and 2.2.2).

With the proposed model is also possible to link, for a given 3rd order PIM contribution, the two-carriers scenario with the multicarrier one, consenting a connection between the typical (and reduced) test scenario with the results which would be observed during the normal operation of the payload. The model, recently published in [63], is fully described in the following subsections.

2.3.1 Evaluation of the overall power associated to the PIM

Let us start with a generic PIM source exposed to a two-carriers excitation. This scenario is denoted by the sub-index $2-\mathrm{c}$ in the following equations.

Thus, the input signal at the PIM source will be the sum of two carriers having angular frequencies $\omega_1 = 2\pi f_1$ and $\omega_2 = 2\pi f_2$ and the same amplitude $A_{2-\mathrm{c}}$:

$$V_{\mathrm{in}-2-\mathrm{c}}(t) = A_{2-\mathrm{c}} \cos(\omega_1 t) + A_{2-\mathrm{c}} \cos(\omega_2 t) \tag{2.28}$$

The non-linear PIM source will generate an output voltage that can be expanded in a polynomial series in the form:

$$V_{\mathrm{out}-2-\mathrm{c}}(t) = C + \alpha V_{\mathrm{in}-2-\mathrm{c}} + \beta V_{\mathrm{in}-2-\mathrm{c}}^2 + \gamma V_{\mathrm{in}-2-\mathrm{c}}^3 + \delta V_{\mathrm{in}-2-\mathrm{c}}^4 + \dots \tag{2.29}$$

If only the 3rd order PIM is considered, the overall power excited by the PIM source and associated to the contribution $\gamma V_{\mathrm{in}-2-\mathrm{c}}^3$ can be expressed by the sum of the powers of each PIM term:

$$OP_{2-\mathrm{c}}\,(\mathrm{mW}) = \sum_i PIM_{2-\mathrm{c},i}\,(\mathrm{mW}) \propto \left(\gamma V_{\mathrm{in}-2-\mathrm{c}}^3\right)^2 \tag{2.30}$$

where the sub-index i expresses each PIM contribution (e.g., $i = 1$ for the term at $2\omega_2 - \omega_1$, $i = 2$ for the term at $2\omega_1 - \omega_2$ and so on).

Likewise, if we now consider a generic multicarrier excitation composed of M carriers having the same amplitude $A_{M-\mathrm{c}}$, the associated input signal must be in the form:

$$\begin{aligned} V_{\mathrm{in}-M-\mathrm{c}}(t) = A_{M-\mathrm{c}}\cos\left(\omega_1 t\right) + A_{M-\mathrm{c}}\cos\left(\omega_2 t\right) + \\ + A_{M-\mathrm{c}}\cos\left(\omega_3 t\right) + \ldots + A_{M-\mathrm{c}}\cos\left(\omega_M t\right) \end{aligned} \tag{2.31}$$

so that the output voltage is given by:

$$V_{\mathrm{out}-M-\mathrm{c}}(t) = C + \alpha V_{\mathrm{in}-M-\mathrm{c}} + \beta V_{\mathrm{in}-M-\mathrm{c}}^2 + \gamma V_{\mathrm{in}-M-\mathrm{c}}^3 + \delta V_{\mathrm{in}-M-\mathrm{c}}^4 + \ldots \tag{2.32}$$

and the overall PIM output power excited and associated to the 3rd order can be expressed as:

$$OP_{M-\mathrm{c}}\,(\mathrm{mW}) = \sum_i PIM_{M-\mathrm{c},i}\,(\mathrm{mW}) \propto \left(\gamma V_{\mathrm{in}-M-\mathrm{c}}^3\right)^2 \tag{2.33}$$

Since the amount of PIM interference may depend on the amount of power into the system, according to the energy conservation assumption, next step is to normalize the input power levels at the PIM source for the two-carriers and the M-carriers cases. This is done by introducing a new parameter called input power ratio (IPR), which expresses, in logarithmic terms, the ratio between the input power in the multicarrier and the two-tones cases:

$$IPR\,(\mathrm{dB}) = 10\log_{10}\left(\frac{M}{2}\right) + 20\log_{10}\left(\frac{A_{M-\mathrm{c}}}{A_{2-\mathrm{c}}}\right) \tag{2.34}$$

The ratio between the PIM power versus the input carriers power is parametrized as follows. Focusing in the 3rd order PIM, an increase of x dB in the input power should imply an increase of $3 \cdot x$ dB in the PIM products according to traditional polynomial theory. However, practical measurements have shown repeatedly that this power ratio is less, in the range between 1.5 to 3 [13,47,51,52]. Thus the PIM increase for an x dB increment in the input power can be expressed in the form $SF \cdot x$ dB, where SF is the practical PIM slope factor which considers this deviation from the polynomial case. This leads that the overall PIM power for the M-carriers case will be related to the two-tones case as follows:

$$OP_{M-\mathrm{c}}\,(\mathrm{dBm}) = OP_{2-\mathrm{c}}\,(\mathrm{dBm}) + SF \cdot IPR\,(\mathrm{dB}) \tag{2.35}$$

Equation (2.35) is fundamental to understand the proposed model and deserves to be highlighted. It is based on the key-assumption that the overall PIM power of the non-linear source (i.e. sum of all 3rd order PIM contributions) depends mainly on the overall input power at the PIM source, regardless of the number of carriers involved in the PIM generation. As a consequence, if the input power is kept constant, the overall 3rd order PIM power is kept constant as well.

2.3.2 Full polynomial model for third-order PIM

Using the classic Taylor series expansion of a multicarrier case, and focusing only on the 3^{rd} order PIM, the overall PIM power in (2.33) must be distributed into the different PIM terms which are stimulated. The number of those PIM terms depends on the number of carriers M involved in the PIM generation. In addition, each term has a different amplitude factor AF (i.e., the coefficient multiplying γA^3). Such a series expansion, however, may be difficult to process as the number M of carriers grows.

Nevertheless, the example at the end of Section 2.1 presents the different 3^{rd} order non-linear terms arising from a generic M-carriers excitation. Exploiting this example, and the expressions (2.7)–(2.9), some rules can be extracted regarding the 3^{rd} order PIM terms:

- PIM terms are located at angular frequencies of the form ω_i, $3\omega_i$, $2\omega_i \pm \omega_j$ and $\omega_i \pm \omega_j \pm \omega_k$. Moreover, the terms at $\omega_i \pm \omega_j \pm \omega_k$ are only present for a number of input carriers $M \geq 3$. As maximum, only three carriers can be mixed by a third order PIM, regardless the overall number of input carriers M.

- All PIM terms placed at angular frequencies of the form $3\omega_i$ have the same amplitude factor $AF = 1/4$. The number of terms is equal to $\binom{M}{1} = M$ (one for each carrier).

- All PIM terms placed at angular frequencies $2\omega_i \pm \omega_j$ have the same amplitude factor $AF = 3/4$. Four terms appear for each pair of carriers ($2\omega_i + \omega_j$, $2\omega_i - \omega_j$, $2\omega_j + \omega_i$ and $2\omega_j - \omega_i$), so the number of terms of this type can be expressed as $4\binom{M}{2}$

- All PIM terms placed at angular frequencies $\omega_i \pm \omega_j \pm \omega_k$ have the same amplitude factor $AF = 6/4$. For each combination of three carriers, four term appears ($\omega_i + \omega_j + \omega_k$, $\omega_i - \omega_j + \omega_k$, $\omega_i + \omega_j - \omega_k$ and $\omega_i - \omega_j - \omega_k$). As a result, the overall number of terms of this type is $4\binom{M}{3}$.

- A term will appear for each carrier at angular frequencies of the form ω_i, resulting in a total number of $\binom{M}{1} = M$ terms of this type. The amplitude factor AF is obtained by adding to the term in (2.7), the $M - 1$ terms corresponding to (2.8) where the index i is set to 1, namely:

$$AF = \frac{3}{4} + (M-1)\,\frac{3}{2} = \frac{6M-3}{4} \tag{2.36}$$

The amplitude factors just derived based on theoretical considerations, have also been verified by the software used in Section 2.2.3. This software can be of

f_1 [GHz]	f_2 [GHz]	f_3 [GHz]	f_{PIM} [GHz]	Term	PIM power [dB]	AF norm.
1.0	1.1	1.12	1.20	$2f_2 - f_1$	0 (Ref.)	1
1.0	1.1	1.12	1.22	$f_3 + f_2 - f_1$	+6.02	2
1.0	1.1	1.12	3	$3f_1$	−9.54	1/3
1.0	1.1	-	1	f_1	+9.54	3
1.0	1.1	1.12	1	f_1	+13.98	5

Table 2.7: Amplitude factors AF computed by the software for some particular 3^{rd} order PIM terms, normalized to the amplitude factor of the reference term at $2f_2 - f_1$.

PIM term	AF
$2f_i \pm f_j$	3/4
$f_i \pm f_j \pm f_k$	6/4
$3f_i$	1/4
f_i	9/4, for $M = 2$ carriers
f_i	15/4, for $M = 3$ carriers

Table 2.8: Denormalized amplitude factors AF for some particular 3^{rd} order PIM terms.

help to deduce the overall PIM power at each particular frequency normalized to one PIM contribution taken as reference.

Table 2.7 shows the power level comparison of several 3^{rd} order PIM contributions normalized to the reference term taken at $2f_2 - f_1$, which have been extracted from the software tool results. The last column is the amplitude factor of each contribution compared to the reference term (obtained by transforming the power level difference from logarithmic to linear units). Taking into account that the amplitude factor of the reference term is 3/4 in virtue of (2.9), the denormalized amplitude factors AF shown in Table 2.8 are thus obtained. These values are in agreement with the ones derived theoretically.

Finally, the sum of amplitude factors (voltage summation) and squared amplitude factors (power summation) of the overall 3^{rd} order PIM terms can be computed, obtaining:

$$\begin{aligned}
\sum_i AF_i &= \left[\frac{M}{4} + 4\binom{M}{2}\frac{3}{4} + M\frac{6M-3}{4}\right] = 8 = 2^3 \quad \text{if} \quad M = 2 \\
\sum_i AF_i &= \left[\frac{M}{4} + 4\binom{M}{2}\frac{3}{4} + 4\binom{M}{3}\frac{6}{4} + M\frac{6M-3}{4}\right] = M^3 \quad \text{if} \quad M \geq 3
\end{aligned} \tag{2.37}$$

and

$$\begin{aligned}\sum_i AF_i^2 &= \left[M\left(\frac{6M-3}{4}\right)^2 + M\left(\frac{1}{4}\right)^2 + 4\binom{M}{2}\left(\frac{3}{4}\right)^2 + 4\binom{M}{3}\left(\frac{6}{4}\right)^2\right] \\ &= \frac{30M^3 - 45M^2 + 20M}{8} = 5\left[\frac{3}{4}M^3 - \frac{9}{8}M^2 + \frac{M}{2}\right]\end{aligned} \tag{2.38}$$

All the results obtained step-by-step so far are summarized in Table 2.9, which includes the full polynomial model for the 3^{rd} order PIM contribution in a generic M-carriers case.

		2 carriers		**3 carriers**		**N carriers**	
		Terms	**AF**	**Terms**	**AF**	**Terms**	**AF**
Frequencies	f_i	2	9/4	3	15/4	M	$(6M-3)/4$
	$3f_i$	2	1/4	3	1/4	M	1/4
	$2f_i \pm f_j$	4	3/4	12	3/4	$4\binom{M}{2} = 2M(M-1)$	3/4
	$f_i \pm f_j \pm f_k$	-	-	4	6/4	$4\binom{M}{3} = 2M(M-1)(M-2)/3$	6/4
Overall Voltage	$\sum_i AF_i$	8		27		M^3	
Overall Power	$\sum_i AF_i^2$	12.5		58.125		$5\left(3M^3/4 - 9M^2/8 + M/2\right)$	

Table 2.9: Number of PIM terms, amplitude factors (AF) and overall output power for 2, 3 and M carriers scenarios for 3^{rd} order PIM contributions.

2.3.3 Evaluation of the power for a particular PIM term

In general, if we now focus on one particular i-th PIM term for a generic p-carriers scenario, the third order PIM power of such a term can be expressed as:

$$PIM_{p-\mathrm{c},i}\,(\mathrm{mW}) = OP_{p-\mathrm{c}}\,(\mathrm{mW}) \cdot \frac{AF_i^2}{\sum_i AF_{p-\mathrm{c},i}^2} \tag{2.39}$$

The meaning of Eq. (2.39) is clear, namely, the power associated to the PIM contribution depends on the overall PIM power into the system, $OP_{p-\mathrm{c}}$, multiplied by the fractional power associated to such a term under consideration.

From the previous expression, it is easy to compute the ratio between the i-th PIM product in the M-carriers scenario and the j-th PIM term in the standard two-carriers case:

$$\frac{PIM_{M-\mathrm{c},i}\,(\mathrm{mW})}{PIM_{2-\mathrm{c},j}\,(\mathrm{mW})} = \frac{OP_{M-\mathrm{c}}\,(\mathrm{mW})}{OP_{2-\mathrm{c}}\,(\mathrm{mW})} \cdot \frac{\sum_j AF_{2-\mathrm{c},j}^2}{\sum_i AF_{M-\mathrm{c},i}^2} \cdot \frac{AF_i^2}{AF_j^2} \tag{2.40}$$

which, after transforming to the logarithmic scale, applying (2.35), and substituting the AF summation terms with the ones detailed in Table 2.9, can be expressed as:

$$\begin{aligned} PIM_{M-\mathrm{c},i}\,(\mathrm{dBm}) =& PIM_{2-\mathrm{c},j}\,(\mathrm{dBm}) + SF \cdot IPR\,(\mathrm{dB}) \\ & - 10\log_{10}\left(\frac{3M^3}{4} - \frac{9M^2}{8} + \frac{M}{2}\right) + 4 + 20\log_{10}\frac{AF_i}{AF_j} \end{aligned} \tag{2.41}$$

The last expression (2.41) links the PIM power associated to a given third order term in a generic M-carriers scenario to the one associated to the two-carriers scenario. In other words, thanks to (2.41) it is possible to obtain the PIM power for a generic M-carriers case from PIM measurements conducted by classic two-carriers PIM test at $2f_i - f_j$.

If we focus on a term having the form $2f_i \pm f_j$ in the M-carriers case, its amplitude factor is the same of the two-carriers case (i.e., 3/4 as shown in Table 2.9), thus the last term in (2.41) disappears. Conversely, if we consider a PIM term having an angular frequency $f_i \pm f_j \pm f_k$, the corresponding amplitude factor is doubled to the one of the term $2f_i \pm f_j$ in the two-carriers scenario, hence the last term in (2.41) involving the ratio of amplitude factors becomes 6 dB.

2.3.4 Experimental validation of the proposed model

The verification of the proposed model through direct PIM measurements is not an easy task, given the large number of carriers to be mixed at the PIM source. This implies a very complex set-up which, in practice, may only be based on PIM measurements conducted at satellite payload level.

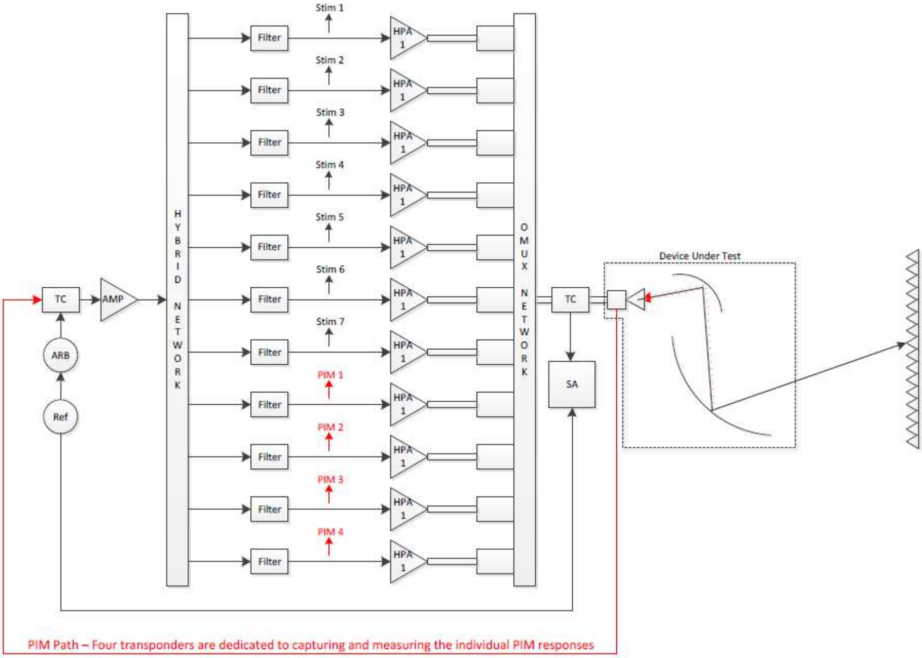

Figure 2.6: Test set-up at spacecraft level assembled by SSL for measuring the effect of non-contributing carriers in selected PIM terms, from [50].

Nevertheless, the verification of the model was possible thanks to an experimental work conducted by Space Systems Loral (SSL), one (if not the most) important satellite payload manufacturer worldwide. Indeed, SSL reported a detailed study on this topic, signed by A. Shayegani, J. Salmon, and R. Singh, published in the Mulcopim 2017 conference [50]. Such a work includes a large number of PIM measurements at payload level, and represents the most complete experimental investigation that has been ever reported so far for this particular topic.

A schematic from the test set-up assembled in SSL is shown in Figure 2.6. Referring to the measurements reported in [50], the utmost care was dedicated to the choice of the carrier frequencies, in order to obtain that all different PIM contributions fall at different frequencies. This is fully consistent with the theoretical model developed in this section.

Further, a PIM versus power sweep test was also conducted in [50], in order to obtain the slope factor SF for the 3^{rd} order PIM contribution. The result was an increase in the PIM power in the range between 2 and 2.3 dB for each dB of increment in the input power [50]. This outcome is aligned with the slope factors reported in technical literature for the same PIM order contribution [13,47,51,52].

Let us now adapt the novel general model to the particular test scenario considered in [50]. In this study, all the input carriers involved have the same amplitude. As a consequence, (2.34), which expresses the increase of the input power into the system with respect to the two-carriers scenario, can be written in the reduced form:

$$IPR\,(\text{dB}) = 10\log_{10}\left(\frac{M}{2}\right) \tag{2.42}$$

where M represents the number of input carriers into the system.

Considering as reference the power associated to one PIM term at $2f_i - f_j$ for the classic two-carriers scenario, we have that for a generic M-carriers scenario (2.41) may be taken in two different ways, depending on the PIM term under analysis:

a. For a PIM term in the M-carriers scenario of the same form $2f_i \pm f_j$:

$$\begin{aligned} PIM_{M-\text{c},i}\,(\text{dBm}) ={}& PIM_{2-\text{c},i}\,(\text{dBm}) + SF\cdot 10\log_{10}\left(\frac{M}{2}\right) + \\ & - 10\log_{10}\left(\frac{3M^3}{4} - \frac{9M^2}{8} + \frac{M}{2}\right) + 4 \end{aligned} \tag{2.43}$$

b. For a PIM term in the M-carriers scenario of the form $f_i \pm f_j \pm f_k$:

$$\begin{aligned} PIM_{M-\text{c},i}\,(\text{dBm}) ={}& PIM_{2-\text{c},i}\,(\text{dBm}) + SF\cdot 10\log_{10}\left(\frac{M}{2}\right) + \\ & - 10\log_{10}\left(\frac{3M^3}{4} - \frac{9M^2}{8} + \frac{M}{2}\right) + 10 \end{aligned} \tag{2.44}$$

To validate the model, a comparison between the test results reported in [50] at antenna level (those under a more controlled environment) and the predictions extracted from the proposed model was conducted (see Table 2.10). For this case, the reference considered is the power associated to the PIM contribution at $2f_2 - f_1$ in the two-carriers scenario. The model was checked with two different slope factors, according to the range $2.0 \leq SF \leq 2.3$ extracted from the stimulus back-off measurements carried out in [50].

Results from Table 2.10 reveals that the addition of a new carrier at f_3 increases the overall power at the input of the non-linear system, but also creates new PIM terms in the spectrum at $f_3 \pm f_2 \pm f_1$, $2f_3 \pm f_2$, $2f_3 \pm f_1$, $2f_1 \pm f_3$, $2f_2 \pm f_3$, f_3 and $3f_3$. According to the proposed model, a redistribution of this overall PIM power into a larger number of PIM contributions leads to a reduction of the power of a particular PIM term, due to the presence of the additional non-contributing carrier.

PIM Term	**2-carriers scenario (meas.)**	**3-carriers scenario**			
		Classic theory	**Predicted (SF=2.0)**	**Predicted (SF=2.3)**	**Meas.**
$2f_2 - f_1$	−115.9 (ref.)	−115.9	−119.0	−118.5	−120.1
$f_2 + f_3 - f_1$	-	−109.9	−113.0	−112.5	−112.7
Difference	-	6 dB	6 dB	6 dB	7.4 dB

Table 2.10: Comparison between predicted and measured PIM contributions for 2 and 3 carriers excitations (all power levels in dBm).

In particular, focusing on the $2f_2 - f_1$ PIM contribution, the additional non-contributing carrier at f_3 should not affect the power of the PIM term according to the classic polynomial theory. However, measurements show that the injection of the term at f_3 causes a 4.2 dB reduction in this PIM term. On the other hand, the model proposed predicts a power reduction between 2.6 dB and 3.1 dB, depending on the slope factor used (see Table 2.10). The prediction can be assumed valid, since an accuracy of ±1 dB in PIM measurements is typical due to measurement uncertainties of the spectrum analyzer.

The PIM term at $f_2 + f_3 - f_1$, on the other hand, cannot appear in a two-carriers test as it requires at least three input carriers into the system. Using the classic theory, this term should be 6 dB above the $2f_2 - f_1$ PIM contribution, because its amplitude factor is twice the one of the reference term (see Table 2.9). Practical measurements, however, show an increase of only 3.2 dB. The new model is also able to justify this reduced increase for this term, through the spreading of the overall PIM power into a higher number of PIM terms. Such an increase is estimated between 2.9 dB and 3.4 dB depending on the slope factor, as detailed in Table 2.10. For this term, the agreement between the predicted value and measurements is excellent.

The last raw of Table 2.10 also shows, for a three-carriers excitation, the difference between two different PIM terms, the one generated by the interaction of three carriers, $f_2 + f_3 - f_1$, and the one resulting from the beating of two carriers, $2f_2 - f_1$. As it can be observed, both the classic and the new model suggest a 6 dB delta, due to the difference on the amplitude factors AF associated to such contributions. Experimental results show a good agreement with the theory also in this case, with a measured difference of 7.4 dB. This implies that the proposed model enhances the traditional one, adding the assumption that if the input power at the non-linear system is kept, the overall power associated to the PIM is maintained as well, regardless the number M of input carriers involved.

Finally, a comparison between the proposed model and practical PIM measurements with a higher number of non-contributing carriers into the system (up to five) was performed. The main results are summarized in Fig. 2.7.

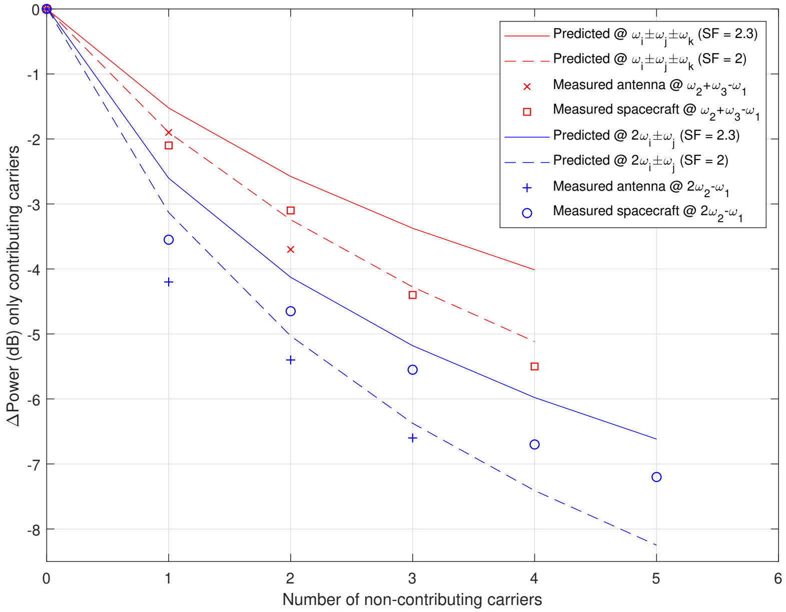

Figure 2.7: Third order PIM output power reduction in terms of the number of additional non-contributing carriers of the same amplitude.

The PIM measured results are extracted from the antenna level and spacecraft ground level scenarios considered in [50]. For the spacecraft ground level, only the results corresponding to co-polar polarization are considered. This is because the PIM terms related to the cross-polarization have lower amplitude levels, being therefore less limiting in practice.

The results reported in [50] allow to obtain the power variation of some particular PIM terms depending on the number of non-contributing carriers excited. These experimental results are compared with the predictions provided by the new theoretical model. Two PIM terms are analyzed, the ones located at $f_2 + f_3 - f_1$ (three-carriers mixing) and at $2f_2 - f_1$ (classic two-carriers mixing). As shown in Fig. 2.7, a good agreement between the predicted values provided by the proposed model and the measured power reduction is obtained. An slope factor SF of 2 seems to provide the best fit to the practical measurements conducted on this particular payload tested at SSL premises. A value of 0 dB in the figure denotes the PIM power level without non-contributing carriers for each term. It can be observed how an increase in the number of non-contributing carriers causes a sustained reduction in the power level of the terms under consideration.

The excellent agreement between predictions and measured results fully validates the proposed theoretical model. An outstanding practical benefit of the proposed model is that is able to predict, starting from measurements conducted in a standard two-tones scenario and focused on a $2f_i - f_j$ PIM contribution, the power of different class of PIM terms when additional non-contributing carriers are added to the system (usual scenario for satellite payloads under operation conditions).

Chapter 3

Novel set-up architectures for evaluating passive inter-modulation in space hardware

This chapter will present the architectures of a set of novel test beds conceived at the European High Power RF Space Laboratory of ESA-VSC (European Space Agency - Val Space Consortium), for measuring passive inter-modulation effect.

The proposed solutions are very flexible, since each architecture is designed to evaluate different PIM orders without requiring any modification of the measurement system in the main RF channel (where the carriers are mixed, thus allowing PIM generation). In addition the proposed architectures consent to mix more than two input carriers simultaneously.

Furthermore, an asset of these benches is their ability to cover both conducted and radiated test scenarios, thus giving an additional degree of flexibility for PIM evaluation.

Another key guideline for the design of these benches is based on minimizing the number of interconnecting elements. This approach has several benefits. Firstly, less interconnections means less PIM sources, since flanges have been demonstrated prone to ignite PIM [17]. In addition, the resulting structure is integrated and compact, thus avoiding mechanical stresses at the connections which may stimulate PIM generation. The compact approach play also a role in improving the electric response of the benches, because all the interactions can be controlled and taken into account during the design phase, thus avoiding a degradation of the overall return losses (related to the interconnect of several elements), and also unwanted spurious resonances which may be stimulated when narrowband elements are connected in cascade.

The references for low PIM test set-ups tend to be quite a few, due to proprietary information and industrial know-how, which refrain payload operators and test laboratories to disclose sensitive information. This limits the assessment of the state-of-the-art for PIM measurements in payload satellites. The results provided in this chapter can therefore be used as a valuable benchmark for PIM measurement test systems for the space sector.

This chapter is divided into three sections. A first section is dedicated to typical test specifications for devices operating in the space sector. This leads to define specifications for the low PIM test set-ups. In addition, practical guidelines for the low PIM design of the novel test benches developed at ESA-VSC laboratories are provided. Next, a second section presents the novel set-up architectures developed for conducted scenarios, for evaluating both backward and forward PIM. Finally, in the third section, the architecture of a new class of set-ups for radiated scenarios is introduced.

The novel contents covered in this chapter were published in [67, 68].

3.1 PIM set-ups design specifications

The PIM test requirements for RF components operating in the RF chain of satellite payloads may be very demanding. In particular, if we consider a two port device, its qualification is typically achieved by detecting a PIM signal below −120 dBm (or in some cases, even lower) after applying at the input port an excitation of two RF carriers delivering around 50 dBm each. This means at least 170 dBc between the carriers and PIM amplitudes, see Table 3.1.

Tx 1	**Tx 2**	**3^{rd} order PIM**	**5^{th} order PIM**
50 dBm	50 dBm	≤ -120 dBm ≤ -170 dBc	≤ -140 dBm ≤ -190 dBc

Table 3.1: Typical customer requirements for PIM tests in RF devices.

Tx 1	**Tx 2**	**3^{rd} PIM**	**5^{th} order PIM**
52 dBm	52 dBm	≤ -140 dBm ≤ -192 dBc	≤ -150 dBm ≤ -202 dBc

Table 3.2: Typical requirements for low PIM set-ups.

As a consequence, the low PIM test bench must provide a residual PIM level well below the one requested for qualification, typically at least 10 dB lower. Test benches are also designed to withstand higher RF power level than the ones for the devices under test. As it can observed in Table 3.2, the test set-ups must be designed to deal with a huge dynamic range between the carriers level and the PIM level (192 dBc or above). This leads to very demanding design specifications in the components composing the low PIM measurement system, such as:

- **Filters in the transmission channels.** PIM is typically evaluated at low odd orders (3^{rd}, 5^{th}), which fall at spurious frequencies close to the carriers. The carrier signals are generated by HPAs, which may work close to their saturation. An HPA in saturation can generate spurious of about −50 dBc at frequencies which are ∼10% away from the carrier. If we consider as benchmark 200 dBc between carriers and PIM (see Table 3.2), **the transmission filters must ensure a rejection higher than ∼150 dB in the PIM reception band** (namely, 200 dBc − 50 dB). This specification can be normally relaxed for higher PIM orders (7^{th}, 9^{th}, etc.), whose PIM band are placed farther away from the transmission one, since the spurious generated by the HPAs decreases sharply as we move away from the transmission carriers.

- **Filters in the reception (PIM) channel.** The PIM signal is typically of extremely weak amplitude. As a consequence, a low noise amplifier (LNA) is required at the reception port of the test set-up. If the reception (PIM) channel is not enough selective to the transmission band, a portion of the two (or more) transmission carriers may reach the LNA and therefore generate Active Inter-Modulation (AIM), which may mask the real PIM signal to detect (i.e. the test system is reading a signal due to the AIM at the LNA instead of the PIM signal). Practical laboratory tests have demonstrated that LNAs produce a negligible AIM if the amplitude of the carriers is below −80 dBm. If we consider as benchmark an amplitude of 52 dBm at the input carriers (see Table 3.2), **the reception (PIM) filter must ensure a rejection higher than ∼132 dB in the transmission band** (namely, 52 dBm − (−80 dBm)).

Another basic aspect of low PIM set-ups is the insertion losses minimization, in order to avoid thermal issues in the bench itself which are demonstrated to be a PIM ignition factor. This aspect is also of paramount importance to take full profit of the RF power of the high power amplifiers (HPAs), the most expensive items in the measurement system.

However, even if the test set-up is designed with filters compliant with the aforementioned specifications, this is typically not enough to guarantee low PIM performances of the measurement system. Indeed, extreme weakness of the PIM signal (−130 dBm or below, see Table 3.2) implies that empiric low PIM principles must be employed in the design of the bench in order to avoid the appearance of potential PIM sources. These main principles, dictated by the common experience of engineers who faced with PIM systems, are the following ones:

- **Minimization of flanged interconnections**, since each flange interconnection is a potential PIM source.
- **The flanges, when necessary, must be designed to minimize (ideally avoid) PIM generation.** This is typically obtained by grooving the surfaces at the mating connections and design the flange with an appropriate number of mating elements (screws and bolts), in order to increase the pressure at the contact area [17, 25, 69]. In addition, particular attention must be paid to the proper torquing of the flanges screws. In addition, the number of mating/demating actions should be minimized. Figure 3.1 depicts a simple geometric rule to assure high mechanical pressure at the flanged area, extracted from [17].

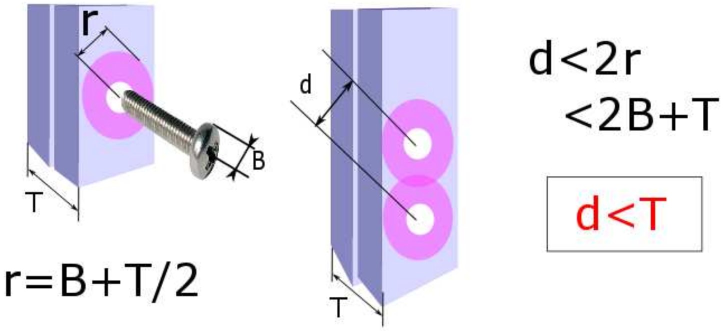

Figure 3.1: Low PIM flange design, the distance between two consecutive holes (d) must be lower than the overall thickness at the flange (T).

- **The hardware must be designed in such a way that the assembly plane to interconnect its parts does not interrupt surface currents.** This may be obtained either by a single piece manufacturing (i.e., electroforming), or manufacturing the device in two identical half-width halves (clam-shell technology).
- **Avoidance of tuning elements.** Tuning elements accumulate the electromagnetic field, normally have strong surface currents, and involve a movable and loose contact area. As a result, tuning elements are a very relevant potential PIM source, whose effect can also be enhanced due to the local heating related to high RF power levels.

A final practical consideration must be also taken into account. Due to budget constrains, it is practically impossible to design and manufacture a customized low PIM test bed for each payload. As a result, flexible solutions able to cover different scenarios should be conceived, if possible.

The architecture of each set-up is related to the nature of the PIM source that the set-up aims to evaluate. For satellite payloads, the PIM sources are typically classified into two main categories, conducted and radiated [13], as already described in Chapter 1.

3.2 Low PIM test beds for conducted scenarios

In a conducted scenario the PIM signal, once ignited, may spread both in forward and backward directions. Given the isotropy of the PIM interference, both components are assumed to be of similar amplitudes. This leads to two different classes of set-ups, which are conceived for measuring each PIM component.

3.2.1 Conducted forward PIM test beds

Forward PIM in a conducted scenario may be measured with test beds using an hybrid-based network for combining the input carriers [5, 17, 33]. This approach, despite being flexible in terms of RF input carriers and frequencies to be mixed, has two main drawbacks. The first one is related to the technology employed for such test benches, which is typically coaxial, thus limiting the PIM evaluation to frequency bands up to 4 GHz (S-band and below). The second inconvenient is related to the architecture of the bench, which tends to be lossy due to the combining network (with losses of 3 dB or above, depending on the number of input carriers combined). The high losses of the system limits the maximum RF power level of the carriers at the DUT plane, making this solution more suitable for systems operating with not extremely high RF power levels, such as mobile networks (i.e., 40-45 dBm maximum) [46].

However, RF components for satellite applications need to be tested at higher RF power levels and frequency bands. The classical solution for space applications is based on modular test benches composed by the cascade of several elements. Depending on the frequencies of each scenario, the test bench can be modified providing some flexibility to the solution. A typical schematic for this approach is depicted in Fig. 1.7 of Section 1.3 (or, similarly, in Fig. 4 of [18]), where 26 blocks are assembled (including two diplexers and seven filters) to perform a standard PIM test with only two input carriers. This solution suffers several drawbacks. Indeed, the high number of interconnections, the worn out given by the continuous mating/demating mechanism to adapt the set-up architecture, the presence of spurious resonances and the inhomogeneous mechanical stress which

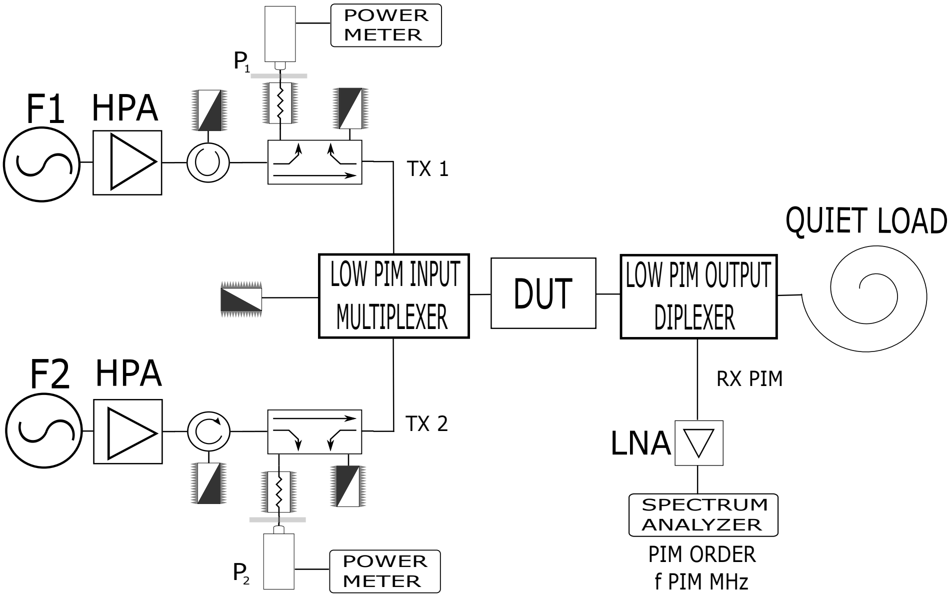

Figure 3.2: Conducted PIM test bed for collecting forward PIM.

may appear at the connectors due to misalignment, may generate additional PIM sources able to degrade the sensibility of the measurement system.

The new class of test benches proposed in this thesis work aims at overcoming these drawbacks. The novel set-up architecture is presented in Figure 3.2.

As it can be observed, the proposed solution minimizes the number of components of the test bed: following the RF-wise direction, the low PIM test set-up can be conceived as an input multiplexer, which combines the input carriers at the input port of the DUT, and a diplexer placed after the DUT, which separate the transmission carriers from the forward PIM generated at the device under test (DUT). The input multiplexer may be designed with two or more different input wideband channels, in order to cover a wider range of scenarios.

The low PIM diplexer is conceived following similar principles, where the PIM detection channel will also be wideband. In addition, the diplexer must provide a moderate rejection (at least 60 dB) at the PIM band between the output port and the input and PIM ports. This isolation preserves the PIM channel from PIM terms which might be generated at the quiet load by the input carriers, that otherwise might come back into the system and mask the real PIM signal generated by the DUT.

The fact that the transmission and PIM channels are wideband improves the flexibility of the system. As a result, the PIM set-up is able to cover a large class of scenarios, both in terms of choice of the transmission carriers and PIM orders, without any modification of the hardware.

Other benefits associated to the proposed solution are detailed below:

- Minimization of the mechanical connections in the main (combined) RF path. Looking at the main RF path on which the carriers are mixed, only the two mechanical connections to mate the DUT are present. Only these two connections may therefore generate PIM. This benefit is evident when compared with the traditional solution shown Fig. 1.7 of Section 1.3, where up to five connections are present in the main RF path.

- Compactness of the test set-up with associated lower insertion losses (thanks to the absence of flanged interconnections and reduction of internal filtering elements).

- Considerable simplification of the test bed assembly, with consequent mitigation of the mating/demating mechanism.

- Avoidance of return loss degradation and unwanted spurious resonances. Since both the multiplexer and the diplexer integrate the required filtering, the proposed architecture is not affected by a deterioration of the electrical response. This is a substantial improvement, in contrast with classical test bench solutions [17, 18, 33, 57], on which the connection of several class of devices may lead to a severe degradation on the return losses level (and, in addition, can give rise to unwanted resonances in the common stopband of consecutive filters).

- The quiet load is not required to provide a particular low PIM performance, because the diplexer is able to block the PIM signal backscattered by the load.

The main drawback of this proposed solution is that particular care has to be dedicated to the output diplexer. Indeed, the PIM port of the output diplexer must be able to damp at least 140 dB the input carriers (to avoid AIM in the LNA). However this tends not to be critical if the transmission and the PIM channels are separated enough, especially when the PIM channel is at a higher band than the transmission channel (thanks to the use of suitable high-pass waveguide sections).

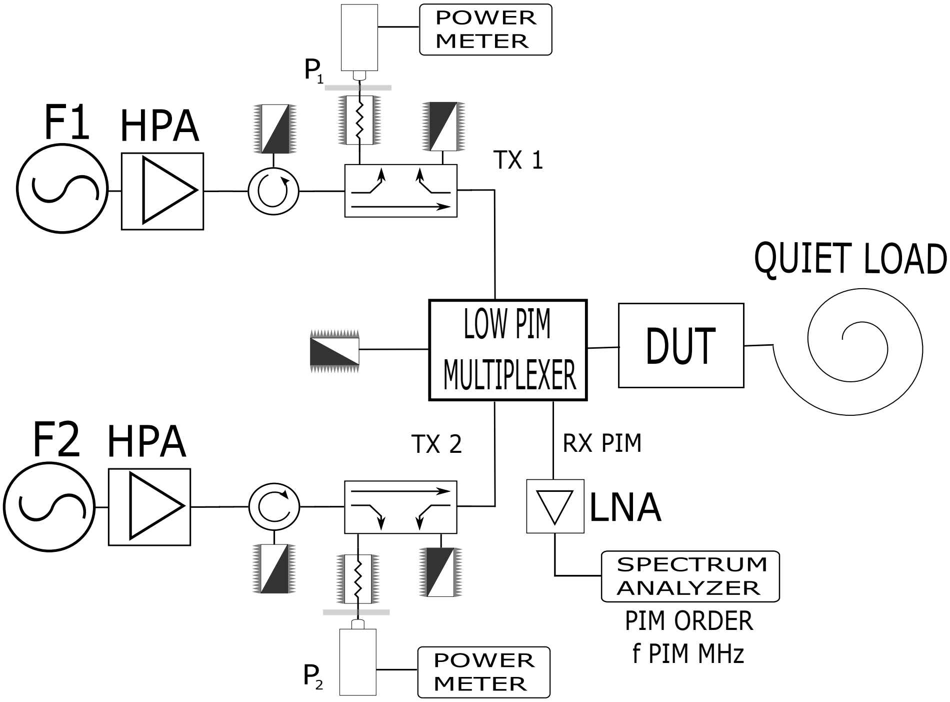

Figure 3.3: Conducted PIM test bed for collecting backward PIM.

3.2.2 Conducted backward PIM test beds

Following the same essential guidelines conceived for forward PIM solutions, the proposed test set-up architecture for evaluating backward PIM is shown in Figure 3.3.

As it may be observed, the solution is fully integrated, being a single multiplexer the key-component of the set-up. This multiplexer has the double task of combining all the RF channels and separate the PIM signal to be detected. In particular, the multiplexer has one RF channel used to pick up and filtering the reflected PIM signal from the DUT towards the reception port. The remaining RF channels are dedicated to filter and combine the different RF input carriers.

Both the transmission and reception filters employed are wideband, and the solution may consent to combine more than two input carriers, if deemed necessary. All these characteristics add flexibility to the proposed solution since, depending on the frequencies and channels chosen, a different PIM order may be collected at the reception port.

Furthermore, this test bench also has the same advantages described in Section 3.2.1 when compared to classical solutions composed of a cascade of several elements [44, 58, 66].

It is worth pointing out that the mechanical connections in the common RF path for this solution, the one sensible to PIM since in this region the carriers are combined, are squeezed to its minimum. Indeed, only the DUT ports must be faced to the test bench. Another characteristic of this set-up is that it consents the PIM evaluation of one RF port devices, such as load terminations.

This architecture, when compared with the one for forward PIM presented in Section 3.2.1, involves the design of only one multiplexer but with one additional filter to separate the backward PIM signal emitted from the DUT. A larger bandwidth must therefore be covered by the multiplexer due to the inclusion of the PIM band, which makes more difficult its design. On the other hand, the fact that the transmission channels and the reception channel are not directly faced (in contrast to the forward PIM solution), contributes to the isolation between the transmission and PIM bands, and therefore to satisfy the rejection requirements.

The main drawback of backward PIM solutions is their sensibility to imperfections in the common RF path, since PIM non-linearities generated there cannot be suppressed or mitigated. This implies that the utmost care must be devoted to the manufacturing of the multiplexer manifold and common port, in terms both of tolerances and symmetry.

Another issue which arises from this solution is that the test facility is also unprotected versus the quiet load, which must be very low PIM. Indeed, any PIM generated at the quiet load would be reflected and collected at the reception port of the test bench if the DUT does not block it. As a result, the design and manufacturing of low noise loads is fundamental to minimize the residual PIM noise floor of the test bed. To overcome this issue, a novel technique to mitigate the residual PIM noise floor of load terminations in waveguide technology is described in next Section 3.2.2.1.

A particular characteristic of this architecture is that the single piece multiplexer may cover, as maximum, an overall frequency range up to about 30-40%. This is normally enough to evaluate low PIM orders (3^{rd}, 5^{th} and 7^{th}), which are the most critical ones in terms of amplitude and frequency [13]. Conversely, this architecture may be unfeasible for set-ups conceived to have the transmission and reception frequencies falling at quite separated bands. This is because the integration of the transmission and reception filters in the same manifold would cause interactions which can lead to undesired resonances, and their suppression in a large bandwidth may be extremely complicated, even applying special wideband techniques [70].

For PIM measurement set-ups where the transmission and reception bands are quite separated, the forward PIM test bed architecture explained in Section 3.2.1 is the best choice. Indeed, this solution simplifies the hardware design, with the drawback of having two pieces, with consequent bulkier size of the test bench and increased cost associated to the manufacturing.

For waveguide technology, the threshold between employing either a backward or a forward architecture is, as a rule of thumb, dictated by the recommended frequency range of operation of a rectangular waveguide (namely, the range where the waveguide is single-mode with a limited dispersion characteristic for the fundamental mode). Indeed, if all the transmission channels and the reception (PIM) channel falls within the recommended frequency range of a common waveguide port, the backward solution is normally the best choice. On the other hand, if the reception channel is outside the recommended operation range of the ports used for the transmission channels, the forward PIM set-up architecture is the most indicated. In such cases, the high-power amplifiers (HPAs) reduces significantly their spurious contribution at the PIM bandwidth. As a result, “only” 60 dB of rejection of the transmission channels in the reception band is normally enough to have a measurement set-up with a dynamic range above 200 dBc in the PIM band (see Table 3.2).

Last but not least, a further difference between backward and forward PIM measurements is related to the interaction of the PIM sources in the main RF path. Indeed, despite PIM is assumed to be isotropic (thus the amplitude of the backward contribution is identical to the forward one), investigations conducted in several identical coaxial connectors showed that different PIM contributions are added in-phase in the forward direction, which leads that the overall PIM signal is the sum of all these contributions [59]. In backward direction things act differently. The location (in wavelength terms) of the PIM sources plays a significant role in the overall PIM signal due to the phase interaction between different contributions. As a result, the amplitude of the PIM contribution measured in a backward PIM test bed may show a relevant variation with the frequency [71].

3.2.2.1 Waveguide terminations with low passive inter-modulation properties

Low PIM test set-ups conceived to evaluate conducted PIM in backward direction are largely treated in the technical literature [16, 46, 66]. However, this class of set-ups are completely unprotected against the PIM signal generated by the dummy termination. This particular drawback is even more relevant in the novel architecture presented in Section 3.2.2, since the quiet load is essentially faced to the reception channel, so the PIM contribution from the dummy load is directly collected by the PIM channel. As a result, the dummy termination may be the limiting factor in tearing down the residual PIM noise floor of the test set-up.

IEC62037 PIM standards recommend the employment of low PIM terminations in the test assembly [46]. The same set of standards also indicate the solution to design quiet loads in coaxial technology, which must be based on long rolled cables (having a longitude of hundreds of meters or more) terminated in a classical coaxial termination. This solution consents to gradually dissipate the RF power along the rolled cable by Joule effect, in a way that the residual RF power arriving to the load is so attenuated that the load itself does not generate significant PIM signal. In addition, the low PIM produced by the load, if any, is strongly attenuated in the way back between the coaxial load and DUT, so the test system results protected against the PIM contribution of the termination.

This solution is however not applicable for waveguide technology, due to the technical constrains in manufacturing long size waveguides and the associated weight, size and cost issues that this solution would imply. Furthermore, the resultant mechanical tensions in the set-up may introduce additional PIM sources, and even cause cracks in the structure, jeopardizing the set-up integrity.

To the author's knowledge, a solution to implement low PIM loads in waveguide technology was never reported in technical literature, so an effort has been done during this Ph.D. thesis work to try to overcome this issue.

The solution found was very simple and essential, somewhat in accordance with the novel PIM set-up architectures presented along this chapter. It consists in inserting a filter between the output port of the device under test (DUT) and the waveguide load, as shown in Figure 3.4. A conventional waveguide termination can be used (obviously dimensioned to the overall power of the transmission carriers), thus avoiding the design, manufacturing and assembly of more complex loads.

The filter has to be designed to allow the carriers to pass through it and, at the same time, it must provide a good rejection for the inter-modulation terms produced by the dummy termination due to the transmission carriers. As a result, the pair filter-dummy load acts as a quiet (low PIM) load, thus protecting the test bench against the PIM ignited by the dummy load.

Filter considerations

The filter to be placed just before the dummy load has to be transparent to the transmission carriers, providing a pass-band response over the frequency region of the transmission channels. This leads that the return losses in such a pass-band should be good (20 dB at least), to avoid that a significant portion of the transmission carriers could be reflected by the filter towards the DUT and the multiplexer, and generate unwanted resonances and even additional inter-modulation terms.

At the same time, the filter must provide good rejection at the PIM band, in order to isolate the test bench from unwanted PIM contributions ignited at the waveguide load. In other words, the filter must avoid that a PIM signal generated at the waveguide load (if any) may entry in the main RF path and be added to effective PIM contribution of the DUT, thus masking the results and reducing the sensitivity of the test bench.

The guidelines for setting the proper filter isolation are discussed next.

Let us consider as PIM^{T} (dBm) the PIM target level requested to qualify the DUT (the superscript T states for target). For example, if a given device has to

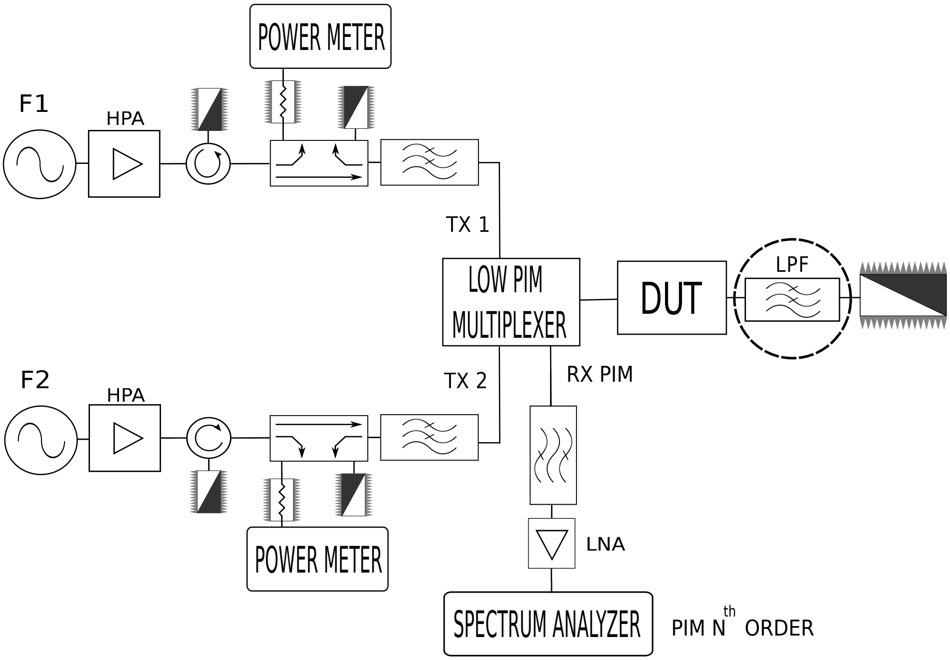

Figure 3.4: Low-PIM test bench in backward configuration with the filter placed before the waveguide load. The filter is highlighted by the circled block.

be certified to show a given PIM order below −115 dBm , thus the PIM target is $PIM^{\mathrm{T}} = -115$ dBm.

The first step is assembling the PIM test set-up with no DUT in place and having only the waveguide load as termination, see Figure 3.5. Next, the residual PIM level of this new test set-up is measured. Since waveguide loads tend to provide the strongest PIM contribution, the PIM value obtained is assumed to be dominated by the dummy load. Let us call this value obtained PIM^{L} (dBm), where the superscript L indicates that the contribution is due to the load.

If we want to tear down the PIM level from the load, the filter inserted before the dummy load must thus provide a rejection at the PIM band such that:

$$Rejection \text{ (dB)} \geq PIM^{\mathrm{L}} \text{ (dBm)} - PIM^{\mathrm{T}} \text{ (dBm)} + M \text{ (dB)} \tag{3.1}$$

where M is the design margin, which should be at least 20 dB or higher, to guarantee that the PIM generated by the load will always be negligible over a PIM signal of a level similar to the threshold PIM^{T} (dBm) to be detected.

In other words, since the waveguide load is the limiting factor for the PIM facility, the design margin M is directly related to the residual PIM level of the

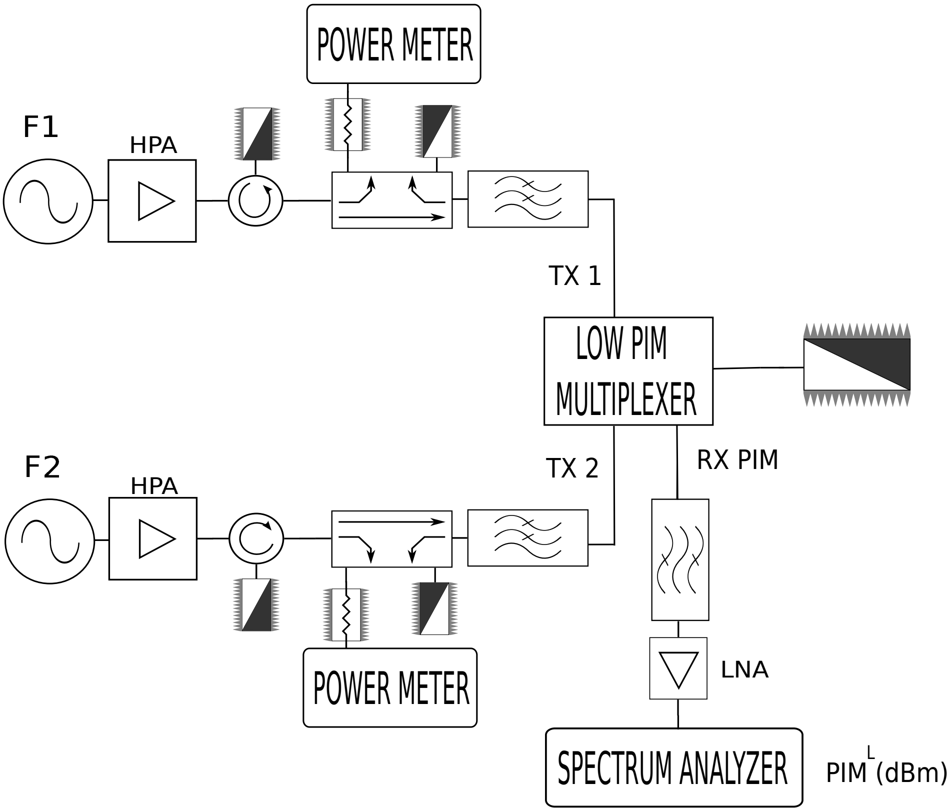

Figure 3.5: Low-PIM test bench with no DUT in place and only the waveguide load as termination. The PIM level from this set-up is assumed to be due to the waveguide only (stronger PIM source), PIM^{L} (dBm).

test facility, which should be always well below the PIM level to be evaluated in the DUT to avoid adding additional relevant PIM contributions to the measurement.

The type of filter to be employed depends on the relative frequency position of the transmission carriers versus the PIM bandwidth. For test set-ups having the PIM frequency band above the transmission carriers, the choice should be a low-pass/band-reject filter solution, as this topology normally guarantees good return losses, compactness and good rejection. Conversely, if the PIM band falls below the transmission carriers, the best topology is a high pass filter. However, if a more compact solution is needed to reduce the mechanical stress in the set-up, a solution based on a combination of a band-pass plus a high-pass filter is also possible, as the one shown in Section 4.2. Whatever solution chosen, the filter must show outstanding intrinsic PIM performance, following the design guidelines already reported in Section 3.1 or in [67].

It is however important to consider that the PIM test bench may present other PIM sources than the one associated to the waveguide load. This implies that a new PIM validation of the test facility is needed after the insertion of the filter (i.e. no DUT in place and filter inserted), in order to check the measured residual PIM level of the set-up is below the target one thanks to the effectiveness of the filter.

Test results to justify the approach

In order to check the validity of the proposed approach, a backward PIM test bed in waveguide technology was assembled in K-band.

This particular set-up is based on a low PIM multiplexer having five transmission channels covering the bandwidth ranging from 17.90 to 20.65 GHz (420 MHz bandwidth per channel, and around 170 MHz of separation between adjacent channels), whereas the reception band for evaluating PIM signal ranges the frequency band between 22.7 and 24.1 GHz [72].

Since for this particular set-up the PIM reception band is above the ones of the transmission carriers, the filter topology to insert before the dummy load will be a combined low-pass/band-reject filter. The PIM requirement was to measure the 3rd order with two transmission carriers delivering 30 W CW each and the target was a PIM level lower than −125 dBm ($PIM^{\mathrm{T}} = -125$ dBm).

According to the procedure explained above, the set-up was assembled first with only the waveguide load in place, in order to measure the PIM level of such a waveguide load PIM^{L} (dBm). A WR51 dummy load was chosen, as this is the standard rectangular waveguide port for the transmission carriers frequency band, thus providing better matching (i.e., low return losses). The data from this first set of measurements is provided in Table 3.3.

As it may observed from Table 3.3, the test scenario covered a wide range of carrier frequencies, so the PIM frequencies excited also ranged different frequencies. However, the same 3rd order PIM term at $2f_2 - f_1$ was always evaluated.

This approach was followed in order to check the PIM behaviour of the set-up over a wide frequency range, thus getting rid of uncertainties which may appear in backward set-ups due to the appearance of other PIM contributions which can be added with a varying phase, as already reported in technical literature for test beds based on coaxial technology [59, 71].

As shown in Table 3.3, the residual PIM level of the set-up was nearly constant for all the combinations and frequencies employed (variations of ±2 dB are typical for PIM measurements, due to the very low amplitude of the PIM signal and the measurement error range of the spectrum analyzer employed for detection). This is consistent with the presence of a dominant PIM source related to the waveguide load. In other words, in case other strong PIM sources are present in the set-up, we should observe a noticeable sum or cancellation of the PIM signal

Tx1 30 W CW f_1 (GHz)	**Tx2 30 W CW** f_2 (GHz)	**3rd PIM Freq.** $2f_2 - f_1$ (GHz)	**3rd PIM Level** PIM^{L} (dBm)
17.96	20.34	22.72	−106
	20.36	22.76	−106
	20.38	22.80	−106
	20.40	22.84	−106
	20.42	22.88	−104
	20.44	22.92	−104
	20.46	22.96	−104
	20.48	23.00	−102
	20.50	23.04	−102
17.92	20.50	23.08	−102

Table 3.3: Conducted backward PIM at K-band with only dummy load in place, test scenario. The PIM value collected is the residual PIM level of the load, PIM^{L} (dBm).

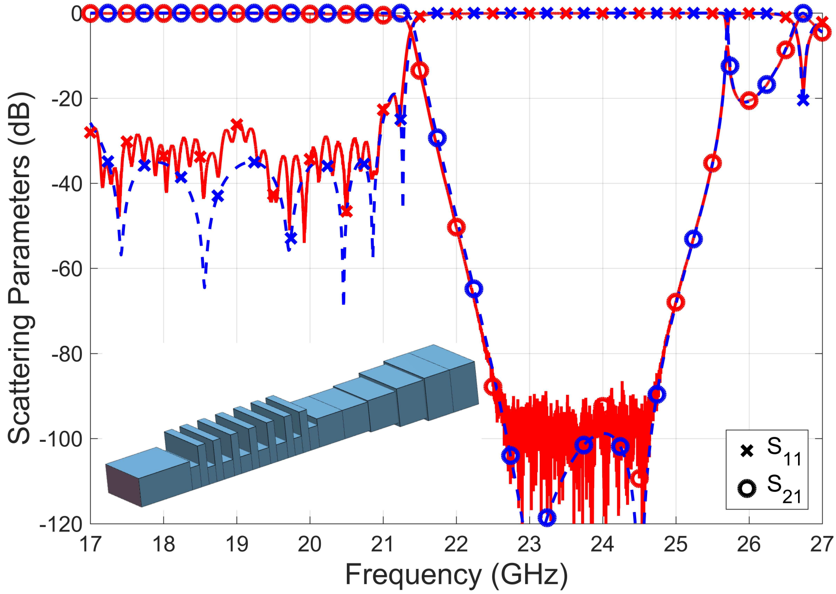

Figure 3.6: Comparison between measured (continuous lines) and simulated responses with FEST3D (dashed lines) of the low-pass/band-reject filter used to mitigate the PIM of the dummy load in the K-band test bed.

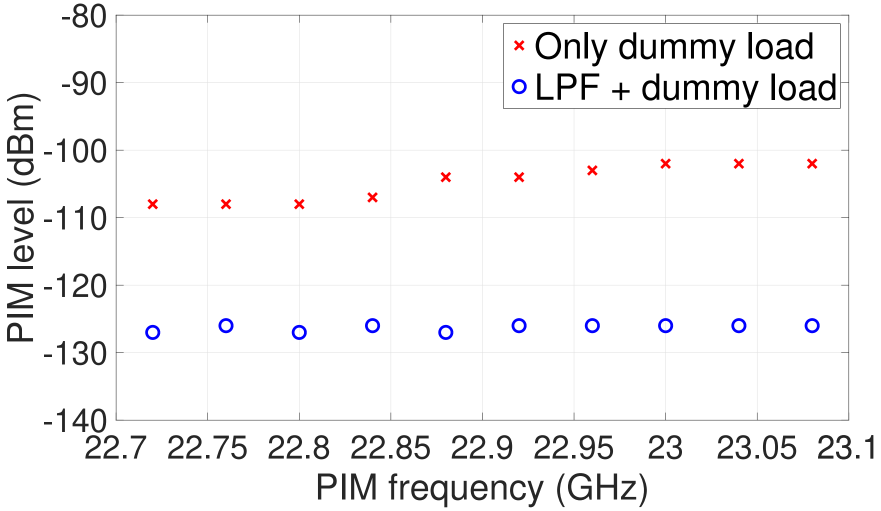

Figure 3.7: PIM measurements with and without low-pass/band-reject filter in place (LPF).

over the frequency range depending on the phase combination of the relevant PIM sources [71]. Since this is not the case in Table 3.3, we can definitely assume that the predominant PIM source is due to the load, and the presence of minor PIM sources, if any, does not play a significant effect.

As a result, the PIM noise floor of the test set-up due to the waveguide load was assumed to be $PIM^{\mathrm{L}} = -102$ dBm. Thus, from equation (3.1) and considering a margin $M = 20$ dB, the minimum rejection provided by the filter at the PIM bandwidth has to be above 43 dB:

$$Rejection\ (\mathrm{dB}) \geq -102\ \mathrm{dBm} - (-125\ \mathrm{dBm}) + 20\ \mathrm{dB} = 43\ \mathrm{dB} \qquad (3.2)$$

In order to fulfil the specifications, a suitable low-pass/band-reject filter has been designed and manufactured (see the inset in Fig. 3.6). The filter has to be transparent to the transmission carriers, and at the same time it has to provide a good rejection at the PIM bandwidth, which is placed at higher frequencies than the transmission band. The filter topology chosen was stub-based, and the heights of the stubs were chosen to obtain transmission zeros at proper frequencies in the PIM band [73, Section II.B].

As a result, the measured rejection was excellent, above 90 dB in the PIM band, being the filter transparent to the carriers with a return loss better than 25 dB (see Fig. 3.6). In order to minimize the flange connections, the filter has a WR42 input port (the same of the common port of the multiplexer), whereas the

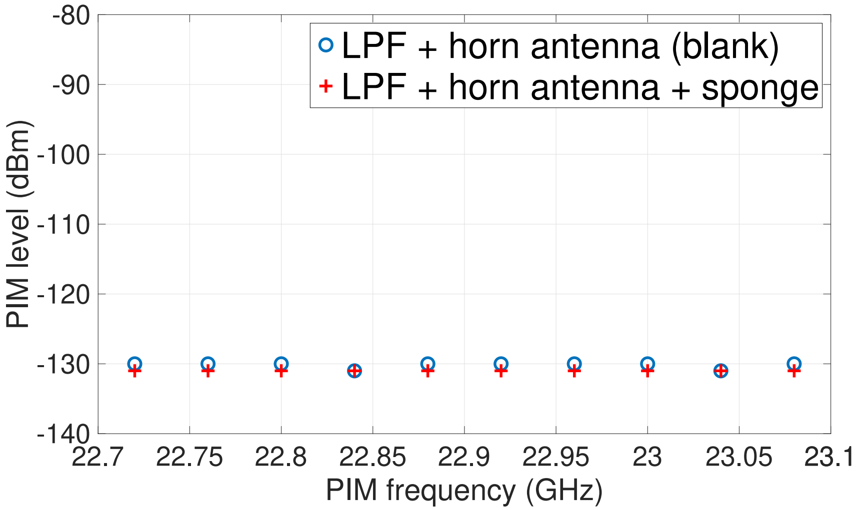

Figure 3.8: PIM measurements with LPF and horn radiating towards an anechoic chamber: comparison with and without metallic sponge as PIM source.

output port was chosen to be a standard WR51 rectangular waveguide (the port of the waveguide load).

It is important to observe that, whereas the input port must be designed to minimize PIM according to the design rules provided in [18], the output port (the one faced to the waveguide load) may use a conventional flange (i.e., not a low PIM flange), as the rejection of the filter is able to block an eventual PIM contribution generated at the output flange interconnection.

The electrical response of the filter, measured with a vector network analyzer (VNA), is provided in Figure 3.6. Since the RF ports have different size, the employment of a WR42 to WR51 waveguide taper was necessary to match with the ports of the VNA. The presence of this taper explains the small ripple observed in the pass-band return losses.

Next, the filter was added to the test facility and placed just before the waveguide load. A comparison between the measurements conducted with and without the filter in place is provided in Figure 3.7. The same set of frequencies as in Table 3.3 was considered. The results show that the insertion of the filter provides a benefit in the residual PIM level of the test facility, which is mitigated in about 20-25 dB.

Such a PIM reduction also demonstrates that the main PIM source of the test bed with only the dummy load in place was indeed the waveguide load, which is thus blocked by the insertion of the filter. An important point which deserves to be highlighted is that with the filter inserted, the PIM level measured is constant over the whole frequency band. This can be attributed to a single “weaker” PIM source present in the common RF path, that now has become the dominant one and provides the residual PIM level of the set-up.

In order to check the benefit associated to the 90 dB rejection filter, a second set of PIM measurements was conducted. The waveguide load was substituted by a horn antenna and the test bench was moved into a low PIM anechoic chamber (i.e., a chamber which was proved to show low PIM contribution). With this new configuration, a first set of measurements was conducted with the filter connected to a horn antenna radiating towards the anechoic chamber (blank reference scenario). Next, a metallic sponge (a strong PIM source) was placed in front of the horn antenna at a distance of around 40 cm and a second set of measurements were carried out. The results obtained are shown in Fig. 3.8. The same frequency scenario detailed in Table 3.3 was applied.

The test bench showed basically the same PIM level in both situations. This provides evidence that the high rejection low-pass filter blocks the PIM contributions generated by the sponge, which are unable to be injected in the measurement set-up. This is therefore a clear confirmation that the proposed approach is a valid solution to manufacture low PIM waveguide terminations, thus protecting backward PIM test beds against dummy loads having poor PIM performance.

The contents of this section dedicated to low PIM terminations in waveguide technology have been published in [68].

3.3 Low PIM test beds for radiated scenario

In the space segment, radiated PIM may be generated from parts of the satellite payload which are illuminated by the RF signal, such as reflectors, deployable meshes, thermal blankets and multi-layer insulation (MLI) blankets, among many others.

The fact that the device under test (DUT) is not physically interconnected as an additional element to the PIM test bed, provides an enhanced flexibility to the assembly.

The architecture proposed for the radiated scenario is derived from the one developed for conducted backward PIM already presented in Section 3.2.2. Indeed, with a few modifications, the same architecture may be adapted to evaluate radiated PIM, as depicted in Figure 3.9. The set-up must be moved into an anechoic chamber, and the high-power carriers are radiated towards the target DUT through a horn antenna directly connected to the common port of the multiplexer. The same antenna of the test bench is also used to collect the radiated PIM signal ignited by the DUT.

This approach inherits all the advantages of the fully integrated architectures

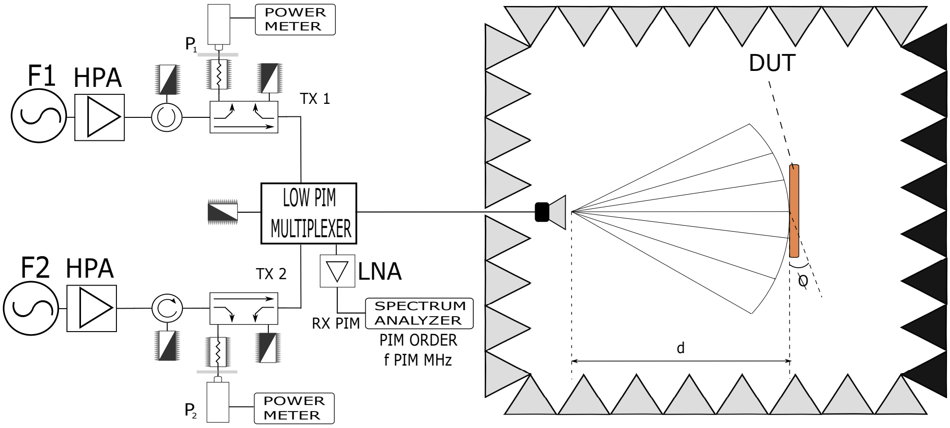

Figure 3.9: Radiated PIM setup for detecting reflected PIM based on the conducted backward architecture.

proposed in this chapter when compared with traditional configurations [57, 58]. Furthermore, there are several additional key benefits obtained from using a single antenna, instead of several antennas to radiate the carriers and receiving the PIM signal.

Firstly, the use of only one antenna for both transmission and reception is the most representative scenario for the DUT under operative conditions. Indeed, the selected area is radiated homogeneously by the two (or more) transmission carriers, whereas the PIM ignited is collected by an antenna which is located in the same position (similarly to satellite transceivers, which usually employ the same antenna for uplink and downlink operation).

The second benefit is related to the angle of the DUT with respect to the test bench. The DUT may be placed faced to the antenna in boresight, which tends to be the worst case scenario. In addition, the distance between the antenna and the DUT may be modulated depending on the isotropic gain of the feed antenna, in order to reproduce the flux power density at the DUT under operational conditions.

Finally, the backward configuration, having only one antenna in the set-up, fully eliminates the cross-coupling effects arising in classical set-ups where several antennas are employed for transmission and reflection. These cross-coupling effects may degrade the PIM performance of the set-up, increasing the noise floor of the facility. The mechanism behind the cross-coupling effect is attributed to an interaction between the antennas, which may act as additional PIM sources able to mask the real PIM signal from the DUT.

This radiated architecture based on conducted backward PIM has, however, the same drawbacks related to the conducted scenario. As a result, the anechoic

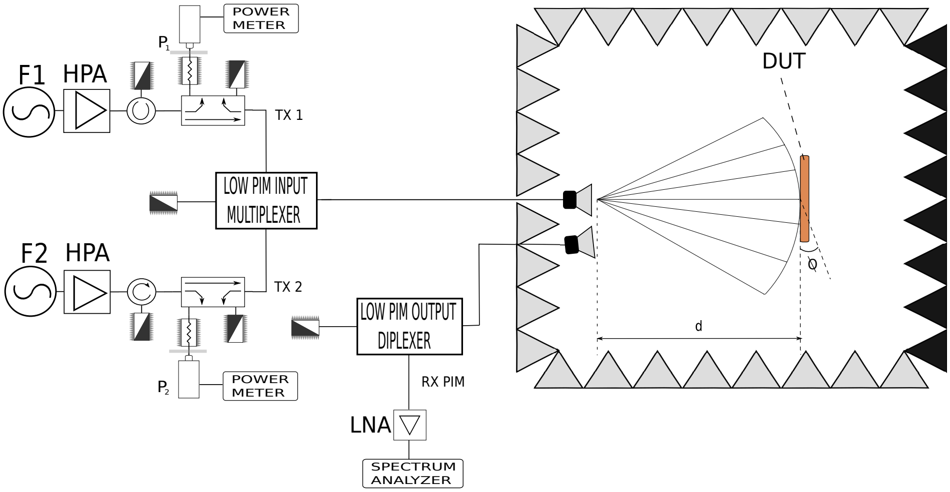

Figure 3.10: Radiated PIM setup for detecting reflected PIM based on conducted forward architecture.

chamber has to act as a quiet load (i.e., it has to be designed to avoid any PIM generation). Furthermore, this architecture is also valid for scenarios aimed at evaluating low PIM orders (the most critical ones), where the reception PIM band is relatively close to the transmission band in frequency terms (and the same waveguide port can be used for both transmitted and received signals).

However, if PIM evaluation is needed for higher PIM orders and involves transmission and reception bands placed further away, the proposed architecture is no longer valid. The alternative for such cases is derived from the conducted forward PIM architecture presented in Section 3.2.1, and is shown in Figure 3.10. The conducted forward set-up is split by the radiated domain. The input multiplexer has the task of mixing the input carriers before being radiated, whereas the output diplexer is dedicated to pick-up the PIM signal generated by the DUT. The common ports of both the multiplexer and the diplexer are connected to a different antenna, for feeding/picking-up purposes (in this set-up, the output diplexer must be mirrored with respect to its configuration in Figure 3.2 employed for evaluating conducted forward PIM).

As detailed above, this configuration requires special care to the placement of the antennas, which must point at the same spot of the DUT and simultaneously reduce their mutual cross-coupling.

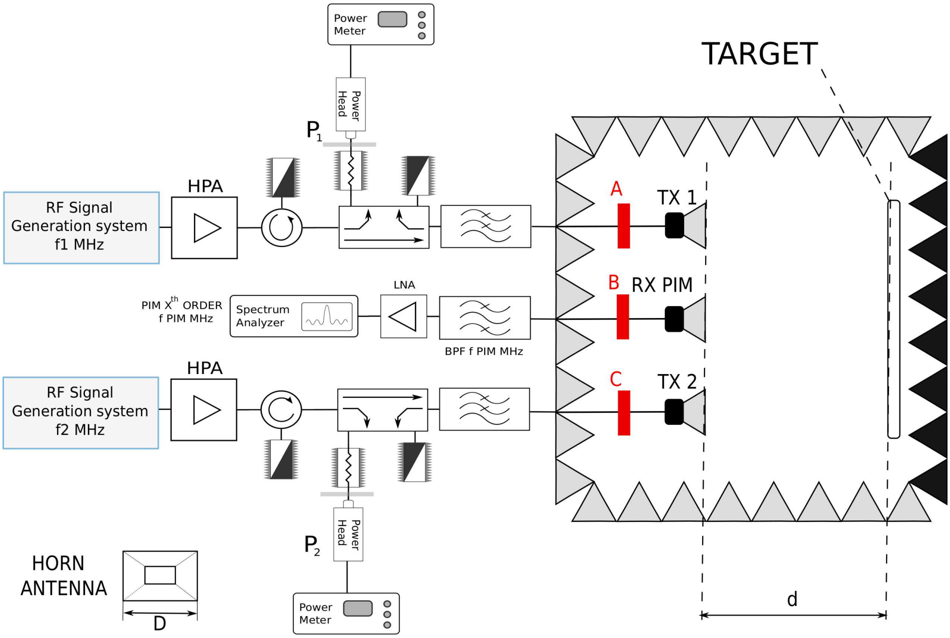

Figure 3.11: Radiated PIM test bed. The transmission and PIM power levels are calibrated at the reference planes A, B, C.

3.3.1 Conversion of payload PIM specifications to a radiated PIM scenario

Radiated PIM tests are conducted placing the DUT at a certain distance from the antenna/antennas of the test bed. The power flux density of the transmission carriers illuminates the DUT, and the ignited PIM is collected either by a sniffer or by means of the same transmission antenna which acts simultaneously as receiving antenna. The latter leads to the novel architecture just proposed before in Section 3.3 (see Fig. 3.9).

The transmission and the PIM level reported in the tests are referred to the reference plane corresponding to the input of the horn/horns (see Fig. 3.11). In other words, the reference plane is not placed in the device to be measured, so the PIM response of the target DUT in terms of real flux power densities is not obtained. A study is considered therefore necessary, in order to cover this gap for actual PIM tests.

Let be d the distance between the horn and the target, and let us consider the far-field condition $d \geq 2D^2/\lambda$ is satisfied, where D is the longer side of the antenna and $\lambda = c/f$ refers to the waveguide length. The quantity $2D^2/\lambda$ is called

Fraunhofer's distance and delimits the near-field from the far-field regions [74]. For elements operating at microwave frequencies, this distance is normally below a few meters, so far-field conditions can be assumed in most cases for actual laboratory tests.

Under these conditions, the power flux density incident at the target from the transmission carriers, $PFD_{\text{Tx-T}}$, can be calculated from the Friis formula [75, 76]:

$$PFD_{\text{Tx-T}} = \frac{(P_{\text{Tx1}} + P_{\text{Tx2}})\, G_{\text{Tx}}}{4\pi d^2} \left[\frac{W}{m^2}\right] \tag{3.3}$$

where P_{Tx1} and P_{Tx2} are the power levels of the two carriers delivered at the input of the transmitting horn antenna, G_{Tx} expresses the isotropic gain of the transmitted antenna (in linear units), and d is the distance between the horn radiating the transmitted signal and the target. Equation (3.3) assumes only two transmission carriers and an antenna spillover factor equal to 1. In case that different antennas are used for radiating each transmission carrier, it is assumed that both antennas have the same gain and are placed at the same distance from the DUT. In any case, expression (3.3) can be generalized for other scenarios straightforwardly.

In typical test scenarios, the powers P_{Tx1} and P_{Tx2} are limited by the high power amplifiers. As a result, the distance d between the transmission horn and the DUT is normally adjusted to obtain the correct power flux density at the target:

$$d = \sqrt{\frac{(P_{\text{Tx1}} + P_{\text{Tx2}})\, G_{\text{Tx}}}{4\pi PFD_{\text{Tx-T}}}} \quad [m] \tag{3.4}$$

It is worth noting that (3.3) expresses a power flux density. The real power incident on the target also depends on the illuminated surface area. In order to obtain reliable results, the illuminated region should be within the main lobe of the transmitting antenna. As an example, the Flann 17240-20 pyramidal horn antenna has a nominal isotropic gain of 20 dB, however simulations at the central frequency of 12.42 GHz showed that the maximum gain is only for a few degrees of the radiation pattern, see Fig. 3.12. At a distance of 116 cm from the horn antenna, this represents a circle of a few centimeters of radius, as shown in Fig. 3.13. For this reason, when possible, the target should be limited to stay within the maximum gain of the horn. A simple procedure to do this is covering the target with low PIM absorbers, and leave exposed to the RF signal only the part placed in front of the transmitting antenna.

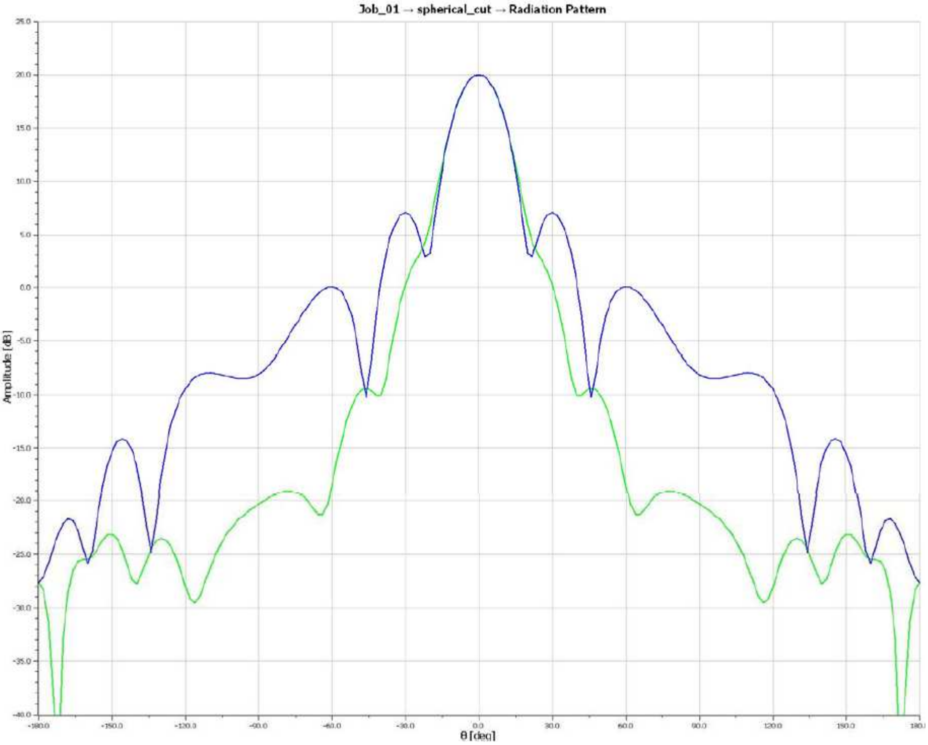

Figure 3.12: WR75 pyramidal horn antenna of Flann, model number 17240-20. Radiated pattern at the central frequency of 12.42 GHz.

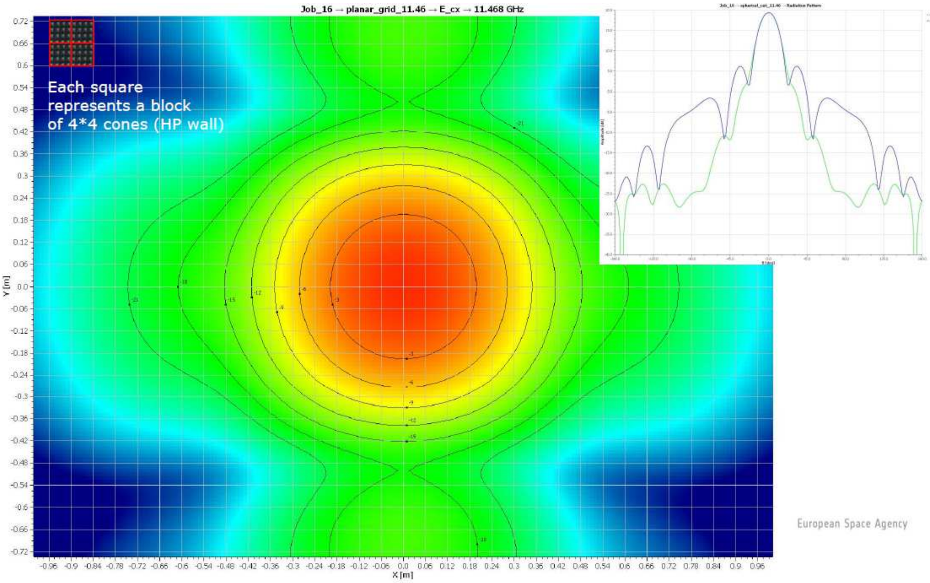

Figure 3.13: WR75 pyramidal horn antenna of Flann, model number 17240-20. Radiated pattern at the central frequency of 12.42 GHz for a plane at a distance $d = 1.16$ m from the antenna. As it can be observed, the maximum gain is only in a circle having a few centimetres of radius.

The PIM level measured at the test bed, P_{PIM} (dBm), is typically read by a spectrum analyzer in logarithmic scale at the reference plane corresponding to the input port of the receiving horn antenna. This value can be correlated to the PIM power flux density emitted from the DUT per unit of surface, PFD_{PIM}, as:

$$P_{\mathrm{PIM}}\ (\mathrm{dBm}) = 10\log\left[PFD_{\mathrm{PIM}} A G_{\mathrm{Rx}}\left(\frac{\lambda}{4\pi d}\right)^2\right] + 30 \tag{3.5}$$

where A is the illuminated surface of the target and G_{Rx} is the gain of the reception antenna (see Fig. 3.14).

From (3.5) we can extract the PIM power flux density at the target:

$$PFD_{\mathrm{PIM}} = 10^{\frac{P_{\mathrm{PIM}(\mathrm{dBm})}-30}{10}}\frac{1}{AG_{\mathrm{Rx}}}\left(\frac{4\pi d}{\lambda}\right)^2\left[\frac{W}{m^2}\right] \tag{3.6}$$

which can be related to the incident power flux density $PFD_{\text{Tx-T}}$ in (3.3) to determine the PIM performance of the DUT.

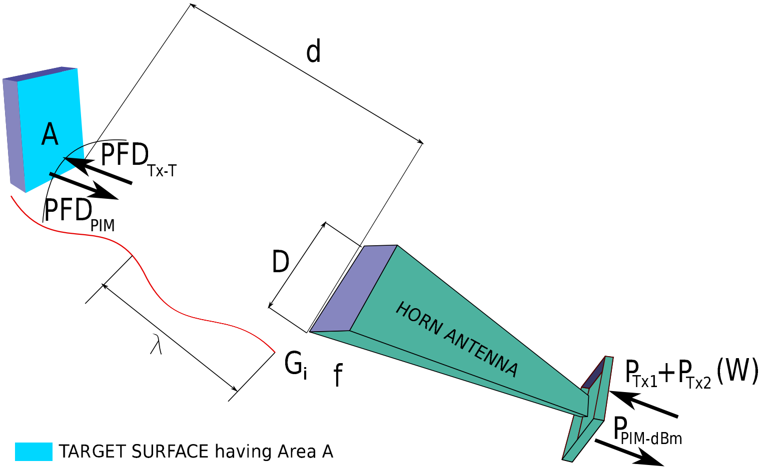

Figure 3.14: Radiated PIM - Test scenario.

It is interesting to notice that the PIM level detected by the spectrum analyzer (SA) is proportional to the surface of the target exposed to the RF for the same PIM power flux density. Indeed, considering two different target surfaces exposed to the RF signal, named as A_1 and A_2, the two PIM levels collected at the SA can be linked by:

$$P_{\mathrm{PIM}}^{A_2}(\mathrm{dBm}) = P_{\mathrm{PIM}}^{A_1}(\mathrm{dBm}) + 10 \log \frac{A_2}{A_1} \tag{3.7}$$

Measurements of radiated PIM from reflecting meshes with two different target areas are reported in Chapter 5, confirming experimentally (3.7).

Chapter 4

Hardware implementation for the proposed test bed architectures

The novel test bed architectures proposed in Chapter 3 present several advantages when compared to traditional PIM set-ups, thanks to the compactness given by the integration of several elements within a reduced number of hardware components. However, the benefits are paid with an increased complexity in the design and manufacturing of the components, which must be compliant with very demanding requirements.

According to Section 3.1, the multiplexers/diplexers employed in the PIM set-ups must cover wide frequency ranges and include several wideband channels. In addition, the rejections to be provided by the embedded filters are outstanding, in the range between 140 and 200 dB. The transmission channels must also handle very high RF power levels, being at the same time low-loss. Last but not least, the use of tuning elements in the filters is not allowed, as they are potential PIM sources. Tuning-less multiplexers/diplexers must therefore be implemented, thus requiring a very precise modeling and manufacturing procedures.

To face up this problem, some design techniques have been recently developed for wide band multiplexing [70, 77]. As an example, a four-channels multiplexer having an overall 40% relative bandwidth has been designed, suitable for reflected PIM measurement set-ups [70, 78]. However, the issues arisen by the integration of both transmission and reception filters within a same multiplexing network, introduced in [79], have not been treated in depth. This chapter describes the implementation details of the filters to be integrated in high-performance PIM set-ups.

4.1 Transmission filters

In the recent past, research activities at the Microwave Applications Group (GAM) of the Universitat Politècnica de València (UPV) leaded to the development of two novel topologies of band-bass filters capable of handling high RF power levels [78], which are suitable to be integrated in the transmission channels of the passive inter-modulation set-up architectures introduced in Chapter 3.

These two families are the so called Hybrid Folded Rectangular Waveguide (HFRW) [80, 81] and Modified Hybrid Folded Rectangular Waveguide (MHFRW) filters [82]. The two configurations, which externally may seem very similar, have relevant differences on the number and position of the transmission zeros (TZs) they can provide, so the use of one topology or the other depends on the complete set of design specifications. In Fig. 4.1 an example of each topology is presented. The folded configurations, in addition to allow the generation of transmission zeros, provide flexibility to the geometrical layout and also a shrinkage of the resulting structures.

In particular, with HFRW filters it is possible to implement an independently controlled TZ for each cascaded trisection [70]. The resulting TZ can be placed very close to the filter pass-band if required [81]. Figure 4.1(a) shows a fifth order filter composed of two concatenated trisections, providing two independent TZs above the filter pass-band.

Conversely, MHFRW filters consent to generate a TZ for each coupling window. The TZ is tuned through the stub created by the resonator location, see Fig. 4.1(b). As a consequence, given a same filter order, MHFRW filters may have a higher number of TZs when compared with HFRW topology [82]. However, the TZs of MHFRW filters are difficult to place close to the pass-band. Indeed, in cases where the coupling window must also provide a strong direct coupling, MHFRW solution is only viable for higher order resonators (i.e., TE_{102} or above) [82].

From a set of specifications, and after adding suitable margins to absorb mechanical tolerances due to workmanship and temperature variations during operation, the first step for the design is the selection of the resonator configuration. In particular, the choice of the resonant mode (TE_{10p}, where $p = 1, 2, 3, ...$) has a considerable impact in the resonator performance, as well as on the robustness and cost of the complete filter.

Filters based on TE_{10p} resonators present a p-times stronger robustness against manufacturing tolerances than filters using TE_{101} resonators. Indeed, the p index is associated to the length of the resonator (i.e. it acts on the longitudinal direction). To make a practical example, a TE_{102} resonator is twice longer than a TE_{101} one, but its sensitivity to manufacturing tolerances is halved. Note also that the variation of the resonator reactance with the frequency (i.e., the resonator slope parameter) is doubled, leading to coupling elements equivalent to the ones of a filter of double bandwidth based on TE_{101} resonances [83–85], and therefore

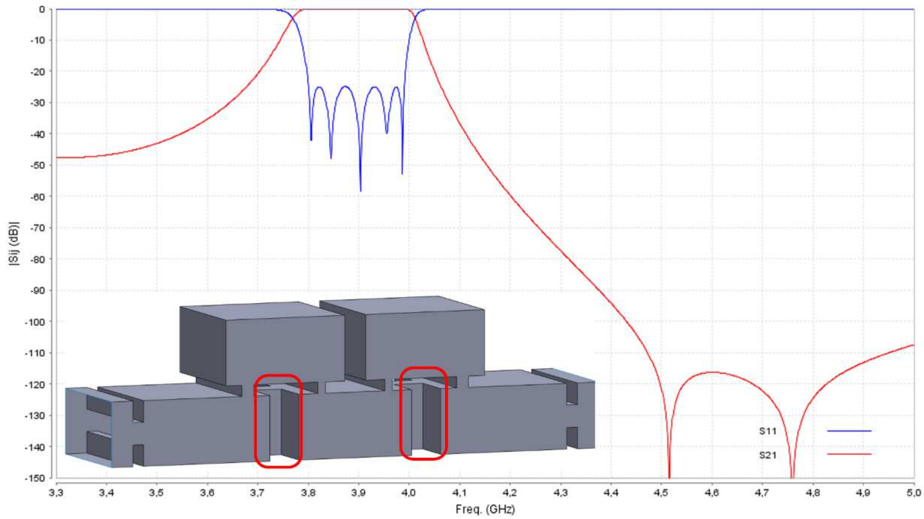

(a) Hybrid Folded Rectangular Waveguide (HFRW) with two TZs

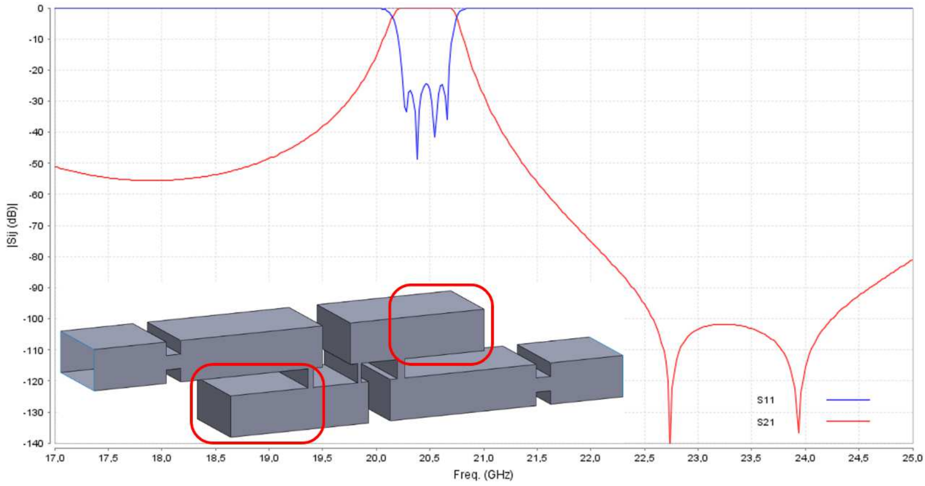

(b) Modified Hybrid Folded Rectangular Waveguide (MHFRW) with two TZs

Figure 4.1: HFRW and MHFRW filter topologies. For each topology, the red boxes highlight the parts of the structure implementing the transmission zeros (TZs).

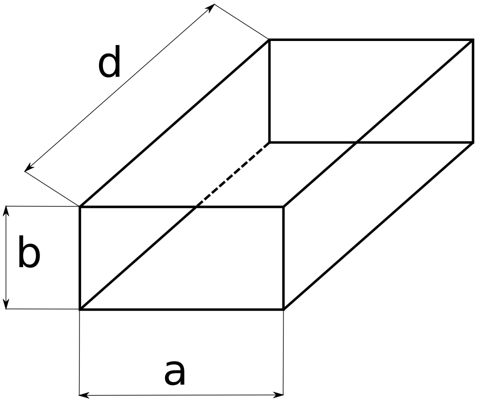

Figure 4.2: Hollow cavity resonator based on a rectangular waveguide.

to an improved manufacturing robustness [86, 87]. This mechanical robustness is fundamental for the implementation of tuning-less filters, since for these structures there is no way to recover any deviation which may occur due to manufacturing.

In addition, filters based on TE_{10p} resonators (where $p > 1$) also improve in terms of insertion losses (the resonator Q is higher [35]) and power-handling capability, in both cases due to the lower EM field accumulation per volume unit.

On the other hand, the drawbacks associated to use filters with higher orders cavities, when compared to TE_{101} resonators, are basically two:

- The larger size, with consequent increased costs in the manufacturing process. Since the manufacturing cost tends to be proportional to the volume of material employed, as a rule-of-thumb, filters based on TE_{10p} resonators cost nearly p times the ones based on TE_{101} resonators for the same order.
- A narrower spurious-free frequency window is obtained, limited at least with the pass-bands related to the $\text{TE}_{10(p-1)}$ and $\text{TE}_{10(p+1)}$ resonances. Note also that the higher the longitudinal index p, the closer the adjacent undesired bands.

For multiplexers/diplexers aimed at covering a wide frequency range, the presence of adjacent spurious bands is a key limiting factor that deserves further discussion. Obviously, the natural choice for wideband multiplexers/diplexers (i.e., relative bandwidth above 25%) consists on exploiting the TE_{101} resonant mode for implementing the filter pass-band, due to the higher separation to the adjacent spurious pass-bands (in this case, normally related to the TE_{102} resonance of the cavities).

Let us consider a hollow rectangular waveguide cavity resonator enclosed by perfect electric walls, as shown in Fig. 4.2. A TE mode only has transverse electric field, which can be expressed in general as:

$$\vec{E}_{\mathrm{t}}(x,y,z) = \vec{e}_{\mathrm{t}}(x,y)\left(A^{+}e^{-\mathrm{j}\beta z} + A^{-}e^{+\mathrm{j}\beta z}\right) \tag{4.1}$$

where $\vec{e}_t(x,y)$ is the normalized transverse electric field of the TE waveguide mode and β its propagation constant.

Being the resonator walls perfect electric conductors, the boundary conditions $\vec{E}_{\mathrm{t}}(x,y,z) = 0$ at $z = 0$ and $z = d$ must be satisfied. Applying these boundary conditions to (4.1) we get $\beta d = p\pi$, which can also be written as:

$$d = \frac{p\pi}{\beta} = \frac{p}{2}\lambda_{\mathrm{g}} \quad , \quad p = 1, 2, \cdots \tag{4.2}$$

where λ_{g} is the guided wavelength of the rectangular waveguide mode.

In general, for a TE$_{mn}$ mode (and also for a TM$_{mn}$ mode) of the rectangular waveguide, the cut-off wavenumber $\kappa_{\mathrm{c},mn}$ and frequency $f_{\mathrm{c},mn}$, the propagation constant β_{mn}, and the guided wavelength $\lambda_{\mathrm{g},mn}$ are given by [35,88]:

$$\begin{aligned}
\kappa_{\mathrm{c},mn} &= \sqrt{\left(\frac{m\pi}{a}\right)^2 + \left(\frac{n\pi}{b}\right)^2} \\
f_{\mathrm{c},mn} &= \frac{c\ \kappa_{\mathrm{c},mn}}{2\pi} = \frac{c}{2}\sqrt{\left(\frac{m}{a}\right)^2 + \left(\frac{n}{b}\right)^2} \\
\beta_{mn} &= \sqrt{k^2 - \kappa_{\mathrm{c},mn}^2} = \frac{\omega}{c}\sqrt{1 - \left(\frac{f_{\mathrm{c},mn}}{f}\right)^2} \\
\lambda_{\mathrm{g},mn} &= \frac{2\pi}{\beta_{mn}} = \frac{2\pi c}{\omega\sqrt{1 - \left(\frac{f_{\mathrm{c},mn}}{f}\right)^2}} = \frac{c/f}{\sqrt{1 - \left(\frac{f_{\mathrm{c},mn}}{f}\right)^2}}
\end{aligned} \tag{4.3}$$

whereas the resonant frequency and wavenumber for a TE$_{mnp}$ (or TM$_{mnp}$) mode of the cavity with p half-variations in the longitudinal axis, are:

$$\begin{aligned}
\kappa_{mnp} &= \sqrt{\kappa_{\mathrm{c},mn}^2 + \left(\frac{p\pi}{d}\right)^2} = \sqrt{\left(\frac{m\pi}{a}\right)^2 + \left(\frac{n\pi}{b}\right)^2 + \left(\frac{p\pi}{d}\right)^2} \\
f_{mnp} &= \frac{c\ \kappa_{\mathrm{c},mnp}}{2\pi} = \frac{c}{2}\sqrt{\left(\frac{m}{a}\right)^2 + \left(\frac{n}{b}\right)^2 + \left(\frac{p}{d}\right)^2}
\end{aligned} \tag{4.4}$$

Assuming that the rectangular waveguide is monomode in the frequency range of interest, only the TE$_{10}$ fundamental mode propagates (for $a > b$ and $f > f_{\mathrm{c},10} = c/2a$), and the TE$_{10p}$ resonant modes of the cavity can be excited. In this case,

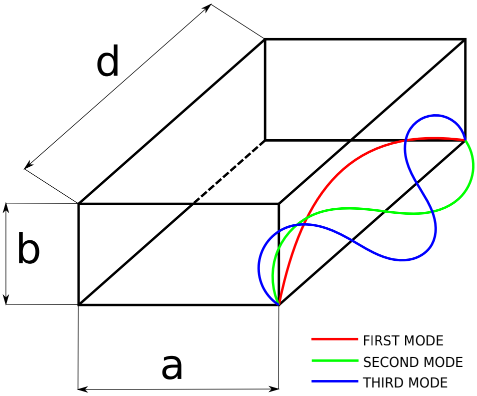

Figure 4.3: Hollow rectangular waveguide resonator with TE_{10p} resonant cavity modes.

from (4.3) and (4.4) we can obtain:

$$
\begin{aligned}
\kappa_{\mathrm{c},10} &= \left(\frac{\pi}{a}\right) \\
f_{\mathrm{c},10} &= \frac{c\kappa_{\mathrm{c},10}}{2\pi} = \frac{c}{2a} \\
\beta_{10} &= \sqrt{k^2 - \kappa^2_{\mathrm{c},10}} = \frac{\omega}{c}\sqrt{1 - \left(\frac{f_{\mathrm{c},10}}{f}\right)^2} = \frac{\omega}{c}\sqrt{1 - \left(\frac{c}{2af}\right)^2} \\
\lambda_{\mathrm{g},10} &= \frac{2\pi}{\beta_{10}} = \frac{c/f}{\sqrt{1 - \left(\frac{f_{\mathrm{c},mn}}{f}\right)^2}} = \frac{c/f}{\sqrt{1 - \left(\frac{c}{2af}\right)^2}} \\
\kappa_{10p} &= \sqrt{\kappa^2_{\mathrm{c},10} + \left(\frac{p\pi}{d}\right)^2} = \sqrt{\left(\frac{\pi}{a}\right)^2 + \left(\frac{p\pi}{d}\right)^2} \\
f_{10p} &= \frac{c\kappa_{\mathrm{c},10p}}{2\pi} = \frac{c}{2}\sqrt{\left(\frac{1}{a}\right)^2 + \left(\frac{p}{d}\right)^2}
\end{aligned}
\tag{4.5}
$$

Since the cavity has fixed physical dimensions, including also its length d, the frequencies which satisfy the condition (4.2) will be the resonant frequencies of the cavity. These frequencies are the ones given by f_{10p} in (4.5). The first resonance, corresponding to $p = 1$, is the one where the length d is $\lambda_{\mathrm{g},10}/2$ (half-wavelength); for the second resonance ($p = 2$) d is $\lambda_{\mathrm{g},10}$, so a complete wavelength is formed in the resonator; for the third resonant frequency ($p = 3$) d equals to $3\lambda_{\mathrm{g},10}/2$, and so on (see Figure 4.3).

In case the HFRW/MHFRW filter is implemented using the TE_{101} mode of the

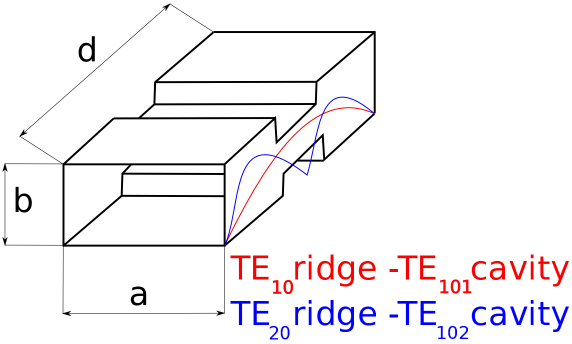

Figure 4.4: Topology of a SIR resonator, which can be interpreted as a double ridge waveguide in the longitudinal direction.

rectangular cavities, the spurious-free range is normally limited by the pass-band corresponding to the TE_{102} resonant mode of the cavities. However, the spurious-free range may be improved through modifications on the resonator geometry for both HFRW and MHFRW topologies. In particular, some benefits were observed by acting on the resonator width. Indeed, from Eq. (4.5) it can be deduced that after enlarging the resonator width a, the resonator length d has to decrease to keep the same resonant frequency. Advantageously, the mode TE_{102} of the resulting resonators is shifted upwards in frequency, increasing the spurious-free range [89, 90]. The main drawback of this solution is that unwanted higher-order waveguide modes, such as the TE_{20} mode, shift down their cut-off frequency and may entry in propagation in the intended stop-band. Although the HFRW/MHFRW filter topologies are symmetrical in width, the manufacturing and assembly can cause slight asymmetries which can excite these unwanted modes that otherwise should not be coupled. As a result, particular attention must be paid to the manufacturing and assembly, and alternative solutions must be prepared against the eventual presence of these modes.

A further benefit is observed adding capacitive sections in the resonators (i.e., modifying the rectangular resonator into a stepped-impedance resonator (SIR)) [91], as shown in Figure 4.4. The SIR structure can be seen as a double ridge waveguide in the longitudinal section of the resonator. It is well known that by inserting a metal ridge at the upper and/or bottom wall of the transverse section of a rectangular waveguide, the cut-off frequency of the fundamental mode is reduced (the larger the ridge depth, the higher the decreasing of the TE_{10} cut-off frequency) without a noticeable modification of the TE_{20} mode. This can lead to an important increase in the monomode region of a waveguide [92]. A SIR applies the same principle in the longitudinal section, so that the resonant frequency of the TE_{101} mode of the cavity is reduced without modifying the TE_{102} resonant frequency for a given cavity length d. To restore the resonant frequency to the desired value, the length d should be reduced. This results in a shorter resonator with the intended TE_{101} resonant frequency, and simultaneously a higher resonant frequency for the TE_{102} mode (due to the reduction in the cavity length). Of course, a suitable trade-off in the depth of the SIR longitudinal ridge is necessary. A shorter resonator would imply a wider stopband with a higher rejection level, at the expense of an insertion losses increase and a reduction on the power-handling capability and robustness against manufacturing deviations (due to the lower gap between ridges, and the higher field accumulation in such a region).

In conclusion, the resonator configuration for the HFRW/MHFRW filters must be chosen as a trade-off among all these factors: mechanical robustness, losses, power-handling capabilities and the spurious-free band required to cover the requirements of the PIM set-up. This will be illustrated in the two examples shown in the next subsections.

Once the type of resonator has been chosen, the maximum order of the filter allowing a tuning-less implementation is found out. The maximum filter order depends on several aspects, both technological and economical. Indeed, the manufacturing tolerance T required for a tuning-less implementation reduces with the filter order N. As a result, an increase in the filter order also increases the manufacturing cost (because of the higher volume of the filter, but also from the tighter tolerances required).

The manufacturing tolerance T tends to be proportional to the relative bandwidth and inversely proportional to the center frequency and the filter order [86]. However, a more recent study [87] provided an improved expression to determine the manufacturing tolerance for inductive filters based on TE_{10p} resonators:

$$T \propto p\frac{BW_{\mathrm{r}}\lambda_{\mathrm{g,wg}}^{1.5}}{N^{1.5}}\lambda_{\mathrm{g,cf}}^{0.5} \qquad (4.6)$$

where BW_{r} is the relative bandwidth in wavelength terms, N is the filter order, p is the resonance order of the cavity (TE_{10p} mode), $\lambda_{\mathrm{g,cf}}$ is the guided wavelength at the pass-band center frequency and $\lambda_{\mathrm{g,wg}}$ is the wavelength at the center frequency of the recommended band of the waveguide.

Since there is a technological (and maybe economical) limit in the minimum manufacturing tolerance attainable, Eq. (4.6) limits the possible maximum filter order. Although (4.6) has been checked to be quite accurate in practice, it is always recommended to perform a Montecarlo analysis to verify the filter order choice. This further verification can be conducted on an initial HFRW or MHFRW filter version without TZs, and confirmed at a second stage for the final topology which includes all the transmission zeros. As a rule-of-thumb, a 4th order tuning-less filter with TE_{101} resonators and a pass-band centered at 20 GHz with 750 MHz bandwidth and 20 dB of return loss can be obtained with a manufacturing tolerance of $\pm 5\mu\mathrm{m}$ (if designed for an equal-ripple return loss of 25 dB).

The following step, having the filter order and the resonant mode determined, is the choice of the topology, either HFRW or MHFRW. Such a choice is leaded by the separation between the PIM band with respect to the transmission one, being the HFRW topology preferred if the two bandwidths are close, thanks to its capability to place TZs very close to the transmission band. Conversely, MHFRW topology tends to be chosen in case the PIM band is quite separated from the transmission carriers, given its ability to provide more TZs (i.e., further rejection) with the same filter order.

Next point is the selection of the filter layout. This point is fundamental, since the transmission filter will be later integrated in the final low PIM multiplexer (MUX). Thus, the layout must take into account several mechanical aspects such as the final clam-shell connection (which requires space for the mating screws between the two halves of the MUX), the connection to the rest of the test bed, heat dissipation gaps, and the final volume of the structure (compact layouts are preferred for their reduced manufacturing cost and easier handling). The layout may also play a role in determining the maximum number of attainable TZs, particularly important for the HFRW topology. It is worth pointing out that, for a filter to be integrated in a wideband multiplexer, it is highly recommended to avoid implementing a TZ using the first resonator, thus limiting undesired strong interactions/resonances between the filters connected to the manifold of the MUX [70].

Additional TZs, and hence higher rejection, can be also obtained replacing some coupling windows with capacitive obstacles [93]. This solution is complementary for both HFRW and MHFRW filters, as it alleviates their main limitations. In the case of HFRW filters, it allows increasing the number of transmission zeros without an increase in the filter order. For MHFRW filters, it allows placing some transmission zeros closer to the filter passband.

In spite of the capabilities of HFRM/MHFRW topologies, sometimes the filter rejection between the transmission and the PIM band is insufficient to satisfy the requirements (see Section 3.1). An additional filter must therefore be attached to the HFRW or MHFRW topology. This filter does not create a concern from a PIM point of view, as it will be placed before the carriers have been combined (between the High Power Amplifier and the HFRW/MHFRW filter). The nature of this additional filter depends on the relative positioning of the PIM reception band with respect to the transmission one, being a low-pass filter (LPF) solution in case the PIM band lays above, and a high-pass filter (HPF) solution in case it is below in the frequency spectrum. However, the insertion of an additional filter in cascade is not the preferred option, due to possible interactions which can cause return losses degradation, as well as spurious responses due to unwanted resonances in the interconnecting waveguide sections. These unwanted effects, however, can be controlled and, in most of the cases compensated during the design stage if the additional filter is integrated in the combining multiplexer.

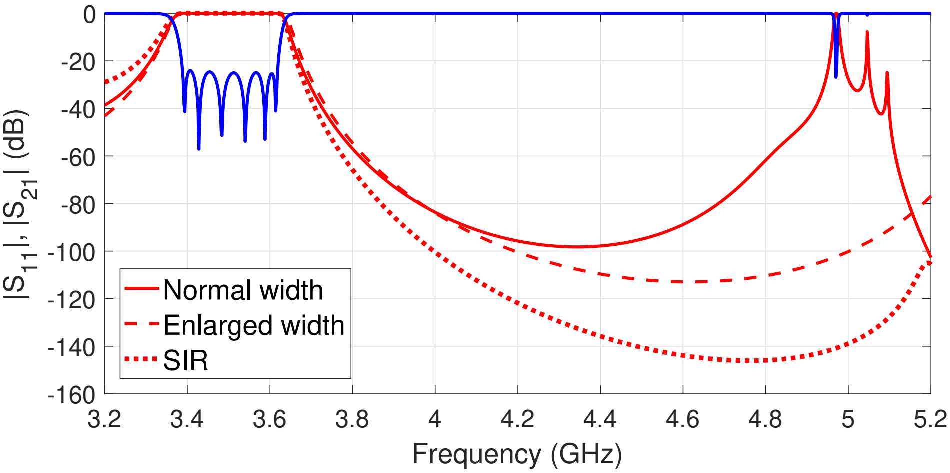

Figure 4.5: 6th order HFRW filter with requested stop-band in the range between 4.4 and 4.9 GHz. Electrical response comparison between different resonator configurations.

4.1.1 First example: sixth order HFRW transmission filter

The first example is focused on a transmission filter, which was implemented in the lower channel of the C-band low PIM multiplexer reported in [70]. The filter has a pass-band between 3.39 and 3.62 GHz with 25 dB of return loss (to get at least 20 dB after manufacturing), and must guarantee an outstanding rejection higher than 165 dB at the PIM band, located between 4.5 and 4.85 GHz. WR229 standard waveguide ports have to be used, whose recommended operation band matches all the intended frequency range.

The filter design was based on TE_{101} resonant cavities, since they provide the more compact structure (very relevant for hardware operating at C-band) and at the same time have the wider free spurious-range. Note that the stop-band ends at about 1.4 times the central frequency of the filter passband, resulting in a wide distance between the transmission and PIM bands for a backward PIM set-up based on a single multiplexing network (see Fig. 3.3 in Section 3.2.2). As the filter operates at a relatively low frequency band, the manufacturing tolerances should not be very restrictive.

This filter is the one corresponding to the first transmission channel of a backward PIM test bed, whereas the pass-band of the last channel (the third one) ranges between 4.12 and 4.27 GHz. Due to the proximity of the last transmission channel to the PIM band, an HFRW topology was selected for all the transmission channels of the C-band multiplexer.

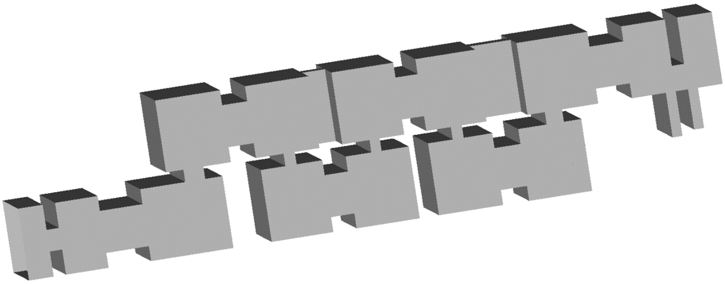

(a)

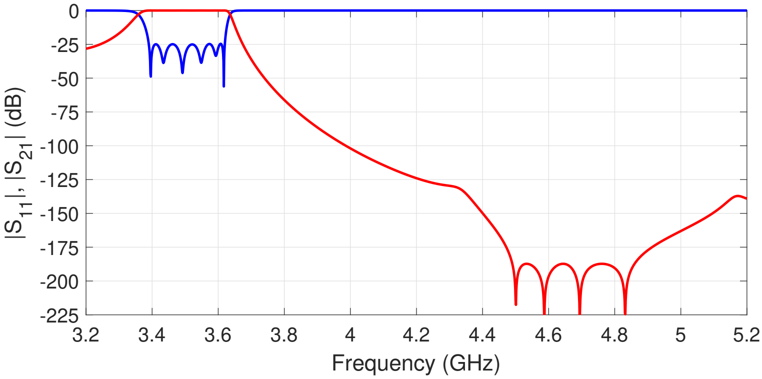

(b)

Figure 4.6: (a) Topology of a 6th order HFRW filter with SIR resonators providing 4 transmission zeros. (b) Optimized final response.

For a manufacturing tolerance T of about ±15 µm, the maximum filter order obtained from (4.6) is nearly 9 in order to get a return loss goal of 20 dB in the pass-band after manufacturing (to attain such a goal, an ideal response of 25 dB of return loss must be considered in the design stage). Anyway, a filter of order 6 was initially chosen to reduce mass, volume and overall set-up manufacturing cost.

In order to choose the most suitable resonator configuration, a performance comparative analysis was performed. Figure 4.5 shows the electrical response of several alternative implementations of an in-line 6^{th} order filter designed with TE_{101} resonators.

A first version uses resonators with the width and height of a standard WR229 waveguide. The resonator length was set to have a resonance of the cavity mode TE_{101} at the pass-band center frequency. The filter shows good electrical response in the pass-band (see Fig. 4.5), however the rejection in the higher portion of the stop-band was reduced due to spurious resonances related to the second resonant mode TE_{102} of the rectangular cavities.

To improve the rejection, a second version of the filter was designed by enlarging the width of the resonators. This leads to a reduced size of the resonator length, which moves the second resonant mode TE_{102} beyond 5 GHz. As drawback, the TE_{20} mode propagates in the enlarged waveguide, with the risk of a severe reduction in the stop-band rejection if it is excited due to small asymmetries in the manufacturing and/or assembling process.

Finally, a third filter was designed with the addition of stepped-impedance resonators (SIR) and maintaining the original width of the WR229 resonators (as in the first implementation). This version showed the best performance in terms of rejection, with reduced risks of higher-order mode propagation (in fact, the only waveguide mode on propagation in both the filter pass-band and stop-band is the fundamental mode TE_{10}), however the insertion losses will be increased due to the capacitive sections (SIR) embedded in the resonators.

As a result, the resonators for this filter were chosen to be SIRs, since this topology provides the best rejection in the stop-band (PIM reception band), as shown in Fig. 4.5. Moreover, it reduces the risk of spurious band due to unwanted resonances related to higher-order modes.

A sixth order HFRW filter consents the implementation of two cascaded trisections, and therefore the independent placement of 2 TZs in the stop-band (one for each trisection, as described in [70]). Unfortunately, the rejection in the PIM band was about 140 dB and did not fully fulfill the requested isolation. Instead of increasing the filter order, two additional TZs were added through the output coupling window following the technique described in [93]. The final isolated filter is shown in Fig. 4.6(a), and its response is provided in Fig. 4.6(b). The software CAD tool used for the design was FEST3D [94], due to its accuracy and efficiency for a structure composed of basic building blocks which can be modeled with modal methods [95]. The use of a very accurate analysis tool providing a fully convergent response is of the outermost importance in this particular application, as any design deviation cannot be compensated with tuning elements.

4.1.2 Second example: fourth order MHFRW transmission filter

The second example is a K-band transmission filter designed for a forward PIM measurement set-up working at K/Ka bands. The pass-band of the filter ranges between 21 and 22 GHz, and the PIM band is located between 27 and 31 GHz, where an extremely high rejection above 165 dB is required.

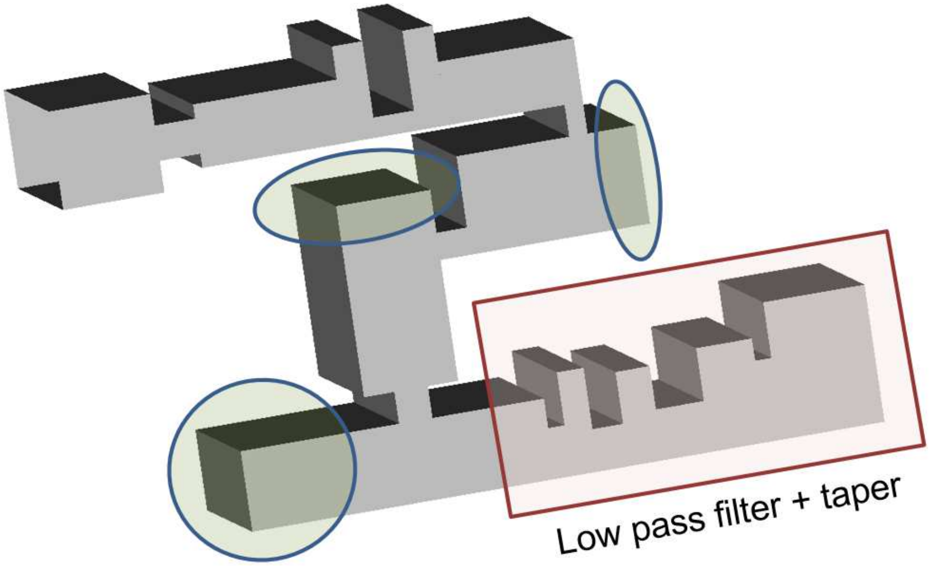

Figure 4.7: Transmission channel filter at K-band, composed by a band-pass filter plus an integrated low-pass filter. The four order MHFRW band-pass filter places 5 transmission zeros, 3 of them controlled by the stubs remarked with ovals.

Figure 4.7 shows the final topology. The filter is based on TE_{101} resonators, due to the far and wide PIM reception band. The MHFRW topology was employed for this filter, because the transmission and reception bands are quite separated.

In this case, a tight manufacturing tolerance T of ± 5 µm allows, in virtue of (4.6), a tuning-less implementation for filters of order equal or lower than 4 (for a minimum return loss of 20 dB after manufacturing and assembling, provided that in the CAD design the return loss is fixed to 25 dB). As a result, a four order filter was considered. Thanks to the capabilities of the MHFRW topology, the fourth order filter is able to provide 5 independent transmission zeros (as shown in Fig. 4.7 and 4.8). As it can be observed, the MHFRW topology can implement a number of TZs higher than the filter order, overcoming the theoretical limits of cross-coupling or extracted-pole techniques [5]. Indeed, for the proposed filter, two TZs are generated by the coupling window between the first and second resonator [93]. Three additional TZs are provided in the following coupling windows of the resonators, and the placement of each TZ is controlled by adjusting the stub sections spotted by blue ovals in Fig. 4.7 [82]. The first coupling window

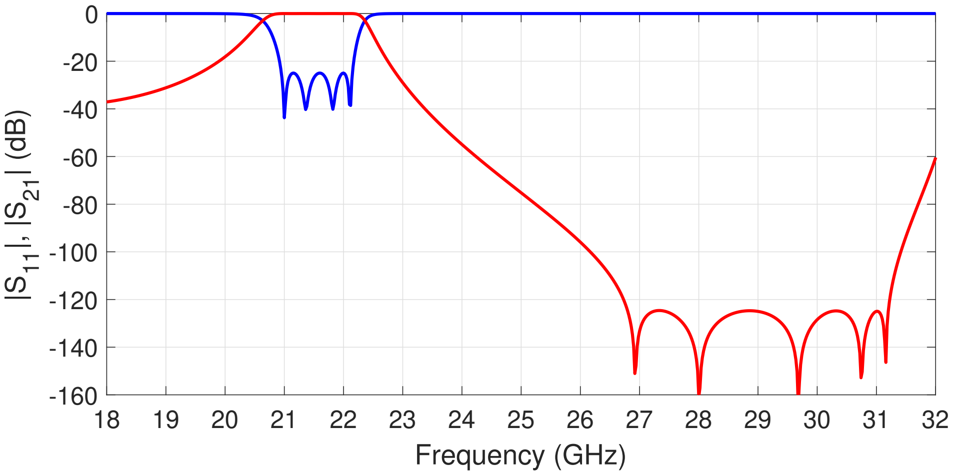

Figure 4.8: Optimized response of the isolated 4th order MHFRW band-pass filter with 5 transmission zeros.

and resonator (the ones closer to the manifold) have not been used to generate transmission zeros, in order to reduce unwanted interactions with the other filters of the multiplexer.

An additional advantage of the MHFRW topology is its geometrical flexibility, which is fully exploited in Fig. 4.7. The filter shape has been conceived to reduce volume, facilitate the interconnection to the manifold of the combining multiplexer. and placing the input channel port in a suitable position to its connection with the rest of the PIM test bed. In addition, some filter twists have also been used to implement transmission zeros.

However, even with 5 TZs, and given the exceptional bandwidth of the reception band (4 GHz, around 13 %), the MFHRW filter alone was not able to keep the rejection above 130 dB (see Fig. 4.8). An additional low-pass filter was therefore cascaded to the MHFRW filter in order to increase the rejection, as shown in Fig. 4.7. An integrated solution was designed, with a small interconnect waveguide section. The dimensions of the band-pass filter were slightly tuned in order to recover the desired pass-band response after combining the MHFRW and the low-pass filters. Figure 4.9 compares the S-parameter response of the integrated solution, with a traditional solution where an external low-pass filter of the same return loss level is attached (without applying any type of compensation). The pass-band return losses are clearly degraded in about 5 dB for the cascade connection of both filters (theoretically, up to 6 dB of degradation may be possible), whereas a resonance appears in the stop-band impairing the rejection level (due to the interconnection section of 15 mm between the multiplexer and the external

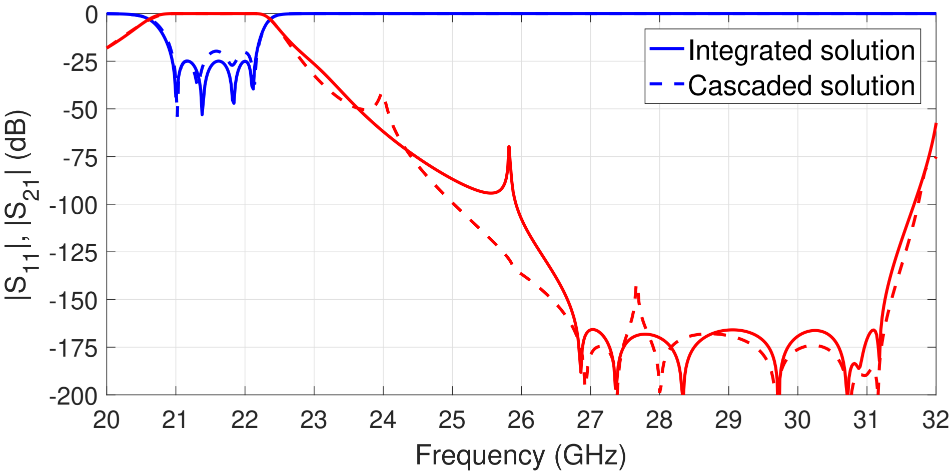

Figure 4.9: Comparison between an integrated design of the band-pass and low-pass filters, and a cascaded connection of both filters through a waveguide section of 15 mm.

low-pass filter). On the other hand, with an increased design effort, the integrated solution is able to control and compensate both effects (note how the resonance in the stop-band has been shifted to a non-harmful frequency thanks to the choice of a more suitable (and shorter) interconnection length).

The degradations caused by the cascade connections grow proportionally with the number of elements. Therefore, the overall response of a classical PIM test bed composed of several elements connected in cascade, as the one depicted in Fig. 1.7 in Section 1.3, may exhibit a quite high degradation even though each isolated element behaves properly. Conversely, by using the integrated solutions proposed in Chapter 3, the effect of these interactions can be compensated and/or mitigated (for instance, the unwanted resonances may be shifted to frequencies outside the PIM reception band).

4.2 Reception filters

The filters to pick up the PIM signal present different characteristics when compared to the ones associated to the transmission channels.

On the one side, the test bed architectures presented in Chapter 3 are conceived to provide a wide bandwidth PIM reception channel. This is a necessary condition to accomplish the flexibility purposes of collecting different PIM orders and for several scenarios. As a consequence, the bandwidth of the PIM channel is typically

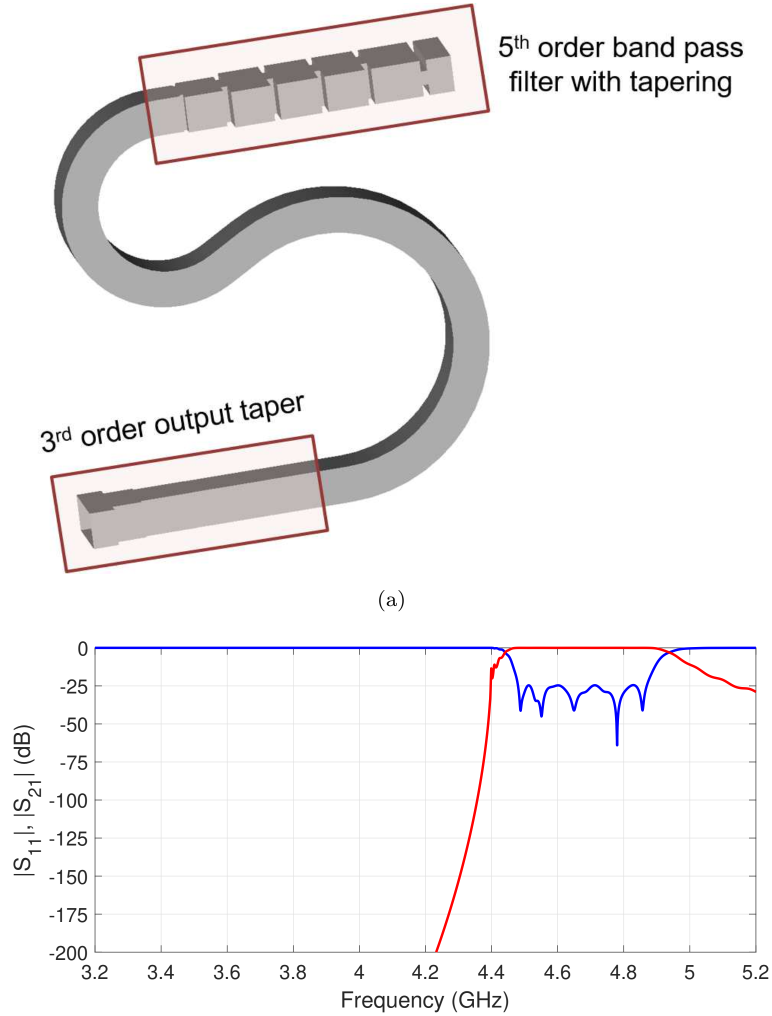

(a)

(b)

Figure 4.10: (a) Topology of the PIM reception filter for on-board hardware composed of a band-pass filter and a high-pass section. (b) Optimized final response.

wider than the one associated to each transmission channel, thus allowing the use of higher order filters according to Eq. (4.6). On the other side, the rejection levels that the PIM filter has to fulfill at the transmission band are less stringent than the ones needed for the filters in the transmission channels (see Section 3.1). All these considerations lead to a filter design less demanding than the one carried out for the transmission filters.

Depending on the PIM requirements, the PIM channel may be placed at frequencies either higher or lower than the transmission band. In scenarios on which the PIM band is falling at higher frequencies than the transmission carriers, the typical situation in on-board satellite payloads (uplink are normally placed at higher frequencies than downlink), the proposed solution for the PIM channel is a band-pass filter cascaded to a high-pass section.

A band-pass filter should be placed in the final multiplexer assembly to accomplish with several tasks. First of all, it can provide a high rejection at the transmission band frequencies to avoid active inter-modulation in the low-noise amplifier (used to increase the low power level of the PIM signal before being measured). Next, it reduces the interactions between the reception branch and the other transmission channels which may lead to undesired resonances, as it provides a high rejection to the carriers from the first resonator. These resonances, if present, may lead to a degradation of the overall response, as already discussed in Section 4.1. Finally, the band-pass filter can be designed to provide a good matching with a cascaded high-pass section, performing also the role of the input taper. In any case, a good tapering at the output of the high-pass section will normally be required.

A practical example of PIM reception filter is presented in Fig. 4.10(a), where a fifth order band-pass filter is cascaded to a high-pass section. The band-pass filter, which also performs the tapering to the high-pass, selects the reception band and provides a rejection on the transmission band of around 50 dB, which is a third part of the one requested to the whole PIM channel. The remaining rejection is provided by the high-pass section.

Fig. 4.10(b) shows the final response of the reception filter, which satisfies the rejection requirements in the transmission band. The non-perfect 25 dB ripple in the reception band is attributed to the interactions between the band-pass and the high-pass sections, however it may be controlled in an integrated solution design.

The dual case, where the reception (PIM) band is placed below the transmission channel, is the usual case for earth-station hardware. It is typically faced by a stub-based low-pass filter having enhanced rejection at the transmission band [96]. The low-pass solution is normally preferred to the band-pass one because it takes less physical space, and provides lower insertion losses and improved robustness to manufacturing tolerances. However, for transmission and PIM bands very close to each other, an integrated band-pass + low-pass filter solution may be required.

Specification	Downlink channel	Uplink channel
pass-band frequency	17.3-22 GHz	27-31 GHz
Return loss	> 20 dB	> 20 dB
Insertion loss	< 0.2 dB	< 1 dB
Isolation	> 50 dB	> 150 dB
Power handling	> 270 W CW	-

Table 4.1: Design specifications for the K/Ka bands PIM diplexer.

4.3 Reception diplexer at K/Ka bands

The novel conducted forward PIM set-up architecture introduced in Section 3.2.1 is suitable to cases where the transmission channels and the PIM reception band are quite separated. This topic is of particular interest in modern telecommunication satellites, which are moving towards higher operating frequencies, such as K/Ka bands or beyond. This is indeed the case of recent High Throughput Satellites (HTS) [7, 97]. As a matter of fact, the International Telecommunication Union (ITU) has assigned for satellite payloads a downlink band (i.e., satellite transmission band) in the range between 17.3 and 21.1 GHz, with a potential future extension up to 22 GHz, whereas the uplink (satellite reception band) has been allocated between 27 and 31 GHz [49].

In this context, an output diplexer compliant with ITU recommendations [49] at K/Ka bands has been designed and manufactured. It becomes a part of a conducted forward PIM set-up based on the architecture presented in Section 3.2.1, due to the huge separation between the downlink and uplink bands (aimed at avoiding 3^{rd} order inter-modulation terms in the reception band). The low PIM diplexer described in this section was presented in the IEEE MTT-S International Microwave Symposium (IMS) held in Philadelphia in June 2018 [73].

The specifications to be fulfilled by the diplexer in terms of frequencies, power and PIM levels are listed in Table 4.1.

The diplexer is conceived to separate the transmission carriers (downlink) from the PIM contribution (uplink). In fact, due to PIM generation in the DUT, the signal at the input of the diplexer will be a sum of several high-power transmission carriers between 17.3 and 22 GHz, plus a weak PIM contribution to be detected in the band ranging from 27 to 31 GHz. The diplexer must be able to sucessfully separate those components.

The internal building blocks of the diplexer are depicted in Fig. 4.11. As it can be observed, the component is composed by three main pieces: a three-port junction at the input, one low-pass filter (LPF) in the main RF path, and a cascade solution formed by a band-pass filter (BPF) and a high-pass filter (HPF) in the reception path.

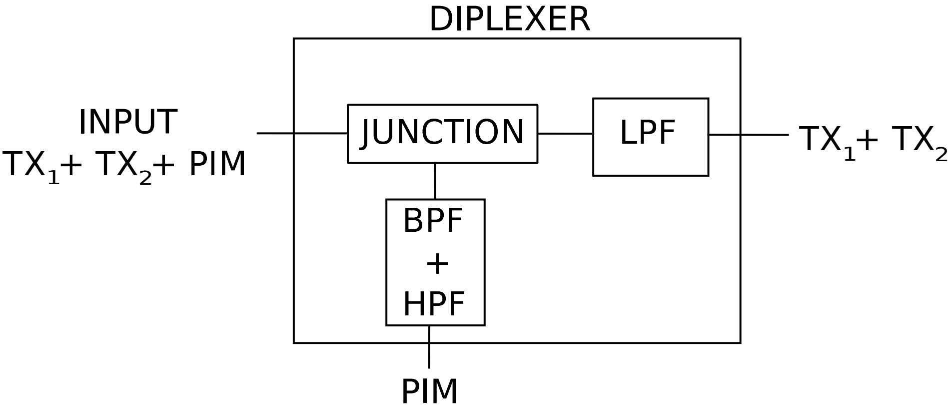

Figure 4.11: Block diagram of the output diplexer for conducted forward PIM test bed architecture (two-carriers excitation case).

The most critical component of the diplexer is the LPF, which must let pass the downlink channel (17.3-22 GHz), and at the same time reject the PIM contribution in the reception channel. This task must be accomplished both from the input port (to reflect the PIM signal to be collected by the reception branch) and also from the output port (to avoid that any PIM contribution coming from the load may interfere the weak PIM signal originated in the DUT, similarly to the filter inserted in the novel solution proposed in Section 3.2.2.1). An optimal equal-ripple response will be sought for both the pass-band return losses and the stop-band rejection.

The BPF + HPF combination in the reception branch must pick-up the weak PIM signal in the uplink band, providing simultaneously a high rejection to the transmission carriers (in order to reduce to non-harmful levels the active intermodulation generated in the Low Noise Amplifier (LNA) placed at the PIM output port).

Both branches are joined by a three-port star junction of reduced dimensions to avoid unwanted spurious resonances at the PIM reception channel. It turns out to be evident that the RF high power path of the diplexer is the one connecting its common input port to the output of the LPF, whereas the branch with the cascaded BPF + HPF is the reception (PIM) path.

Looking at Table 4.1, the band to be covered by the diplexer is outstandingly wide, around 58%, divided between the 24% for the transmission filters and the 14% for the PIM channel. These are unprecedented figures in the technical literature.

For the given downlink frequency range, standard WR51 waveguides (recommended band from 15 to 22 GHz) were employed for the input port of the diplexer

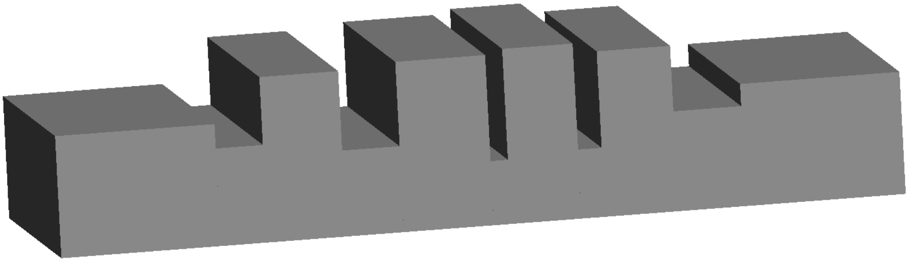

(a)

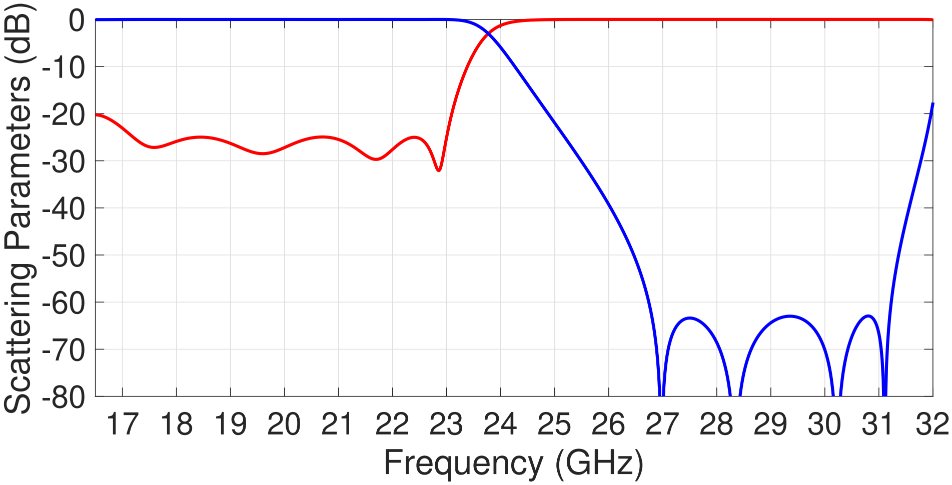

(b)

Figure 4.12: Band-reject filter topology in (a), and simulated response in (b).

and the main RF path (including the output port of the LPF), whereas the PIM port (output of the cascade BPF + HPF solution) was implemented in WR28 standard waveguide with recommended operation band between 26.5 and 40 GHz.

At the input port of the diplexer, the high power transmission signal (downlink) will be on a monomode regimen, but the PIM signal to be detected will be transported through different modes (only the fundamental TE_{10} mode propagates in a WR51 standard waveguide until 23.1 GHz approximately). Therefore, some part of the PIM signal originated from the DUT can be coupled to higher-order modes. The star junction combining the filters has a reduced height of 4.65 mm, so it reflects any contribution in the PIM band associated to the TE_{01} mode.

4.3.1 Low Pass Filter design (high-power)

The LPF has a stub-based structure. The filter width is kept constant, and is the same one of the WR51 input/output ports. The height of the filter ports has been fixed to 4.65 mm, in order to cut-off the TE_{01} mode at the PIM reception band frequency range. A two-step transformer is implemented next to connect with the WR51 output port for the transmission carriers. Each stub places one TZ in the PIM band, which can be controlled independently. In the rejection band, the filter behaves as a short circuit for the PIM signal coupled with the fundamental TE_{10} mode, which is reflected and then collected in the reception channel of the diplexer (which is described in Section 4.3.2).

Similar structures have been presented in the recent literature [98–100], where some design parameters were set to the same value (e.g. stubs (width/height) or capacitive sections length/height). However, the full capabilities of this topology have not been deeply studied yet.

The ninth order LPF designed is depicted in Fig. 4.12(a). It is composed by 5 capacitive (i.e., low-height) sections and 4 inductive (i.e., high-height) sections, and the FEST3D simulated response is shown in Fig. 4.12(b). The filter provides an optimum Zolotarev transfer function at the pass-band and and equal-ripple rejection at the reception band (with the four possible transmission zeros). The required power-handling capability of the filter is guaranteed thanks to a minimum gap size of 2 mm.

4.3.2 Reception filter chain in the PIM band

The high frequency channel of antenna diplexers is typically implemented through a high-pass filter (HPF). The HPF is composed by a narrowed waveguide section tuned to be monomode at the reception band and below cut-off at the transmission band [98, 101–103].

For our application, a band-pass filter (BPF) was also included, since it provides additional benefits, namely:

- Improvement of the rejection at the transmission band (downlink).
- Improvement of the compactness (HPF input taper no longer requested, as the filter can make this role).
- Easier connection at the manifold between the downlink and uplink filters. Indeed, the first resonator of the BPF provides isolation at the downlink frequency band. This is particularly convenient in order to avoid unwanted resonances in wideband diplexers/multiplexers [70].

Figure 4.13 shows the simulated electric response of the cascade BPF + HPF in the reception (PIM) band. The BPF is composed by five TE_{101} in-line resonators

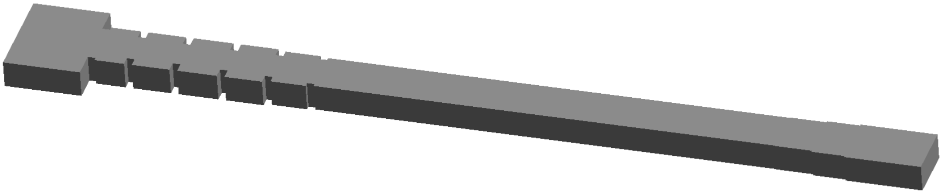

(a)

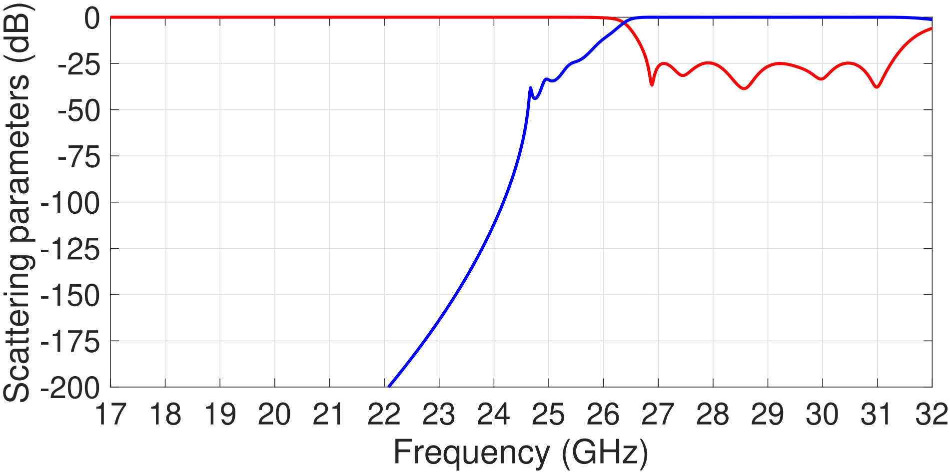

(b)

Figure 4.13: PIM filter topology in (a), and simulated response in (b).

in WR28 (the last one is 6.5 mm wide) coupled by inductive irises. Considering the manufacturing tolerances for a tuning-less structure, the BPF order was limited to five. The HPF has a width of 6.1 mm and its length was adjusted to obtain an overall rejection greater than 200 dB at the downlink frequencies. Finally, a two-step quarter-wavelength taper was used to match the reception channel to the standard WR28 uplink port.

Considering the frequency of 22 GHz as the critical one for the rejection (being the highest frequency of the downlink), the BPF provides 75 dB of the 200 dB of rejection, taking up 30 mm of the 103 mm overall length of the BPF + HPF cascade. Using only a HPF without BPF (i.e. following the classical approach [98, 101–103]), the HPF length would have been about 125 mm. This proofs the advantage in terms of compactness of inserting the BPF filter, although an increase in the insertion losses is also expected. In the final design, the HPF section was meandered in order to improve the compactness of the overall diplexer.

4.3.3 Junction

The three-port star junction has the task of joining the input port with the LPF and the cascade BPF + HPF branches. It has been designed using a wideband E-plane T-junction, since this solution is the most suitable for clam-shell manufacturing without interrupting conduction currents (two identical halves in the wider side of the WR51 waveguide). In addition, an E-plane T-junction also guarantees a wider bandwidth than an H-plane one. The latter is an important aspect to take into account for such a wideband diplexer, which must cover an overall (and unprecedented) 17.3 to 31 GHz frequency band at its input port.

The star junction has the width of a standard WR51 waveguide, but a reduced height of 4.65 mm to reject any signal coupled by means of the TE_{01} mode in the reception band. However, a PIM contribution propagating through the TE_{20} may pass the junction. As this contribution is at cut-off in the BPF + HPF branch, it can only be reflected to the diplexer common port or propagated through the LPF towards the load.

The star junction is connected to the common WR51 input port of the diplexer with a transformer, and by means of a short waveguide section to the LPF (whose length is adjusted in order to improve the impedance matching of the HPF + BPF branch).

4.3.4 PIM diplexer results

The design of the diplexer has been conducted by FEST3D [94], as this particular component can be decomposed in the cascade connection of several blocks which can be accurately represented by a multimode network representation. As a result, it is particularly suitable for advanced modal analysis methods.

Figure 4.14 shows the simulated electrical response of the hardware for TE_{10} excitation at the input port. As it can be observed, the FEST3D results were compared with an analysis conducted by Ansys HFSS [104], showing an excellent agreement.

The diplexer has been manufactured in pure aluminium, without the presence of tuning elements. The comparison between simulation and real measurements is shown in Fig. 4.15.

As it can be observed, the agreement for a tuning-less component is excellent in the downlink band, which corresponds to the WR51 monomode region. The small deviations in the S_{11} parameter at the common port can be attributed to the manufacturing tolerances. Conversely, some deviations were observed in the reception band (uplink), particularly concerning the spikes in the isolation between the input (common) port of the diplexer and the output port for the transmission carriers. These spikes are related to the TE_{20} mode, which is excited by small misalignment/asymmetries within the hardware (i.e., non-perfect clam-shell) or at the waveguide port connections. However, this unwanted response is

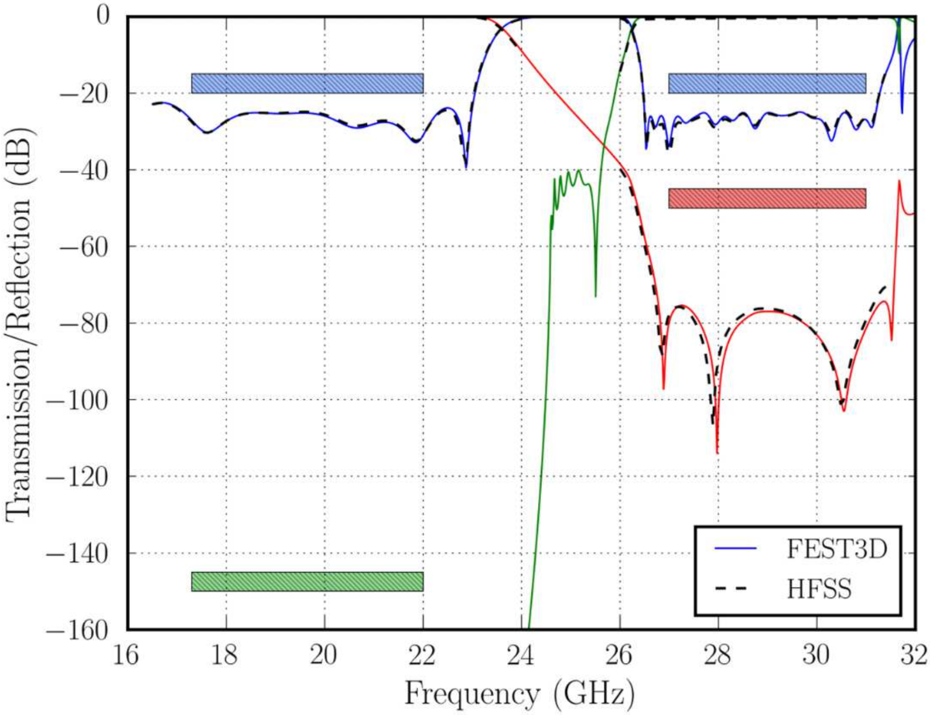

Figure 4.14: Comparison of the simulated response between CST FEST3D and Ansys HFSS (the design masks are included for reference).

not problematic for the application of the diplexer, since the PIM signal generated by the DUT in the forward direction and coupled with the TE_{10} mode (the main part) will be successfully collected by the PIM reception branch of the diplexer. Only the PIM contribution coupled with the TE_{20} mode can reach the downlink output port connected to the quiet load. Moreover, the transmission carriers are conveniently guided through the high-power branch of the diplexer, and are highly attenuated at the PIM reception port (so that their active inter-modulation at the LNA can be neglected). It does not seem therefore necessary a re-design of the hardware to remove these spikes by adjusting the width of the LPF or the input port [98], at the cost of a reduced power-handling and increase on the LPF insertion losses.

The manufactured component shows a measured return losses better than 22.5 dB and insertion losses lower than 0.15 dB in the downlink band. As far as uplink (PIM reception) band concerns, the return losses are better than 20 dB

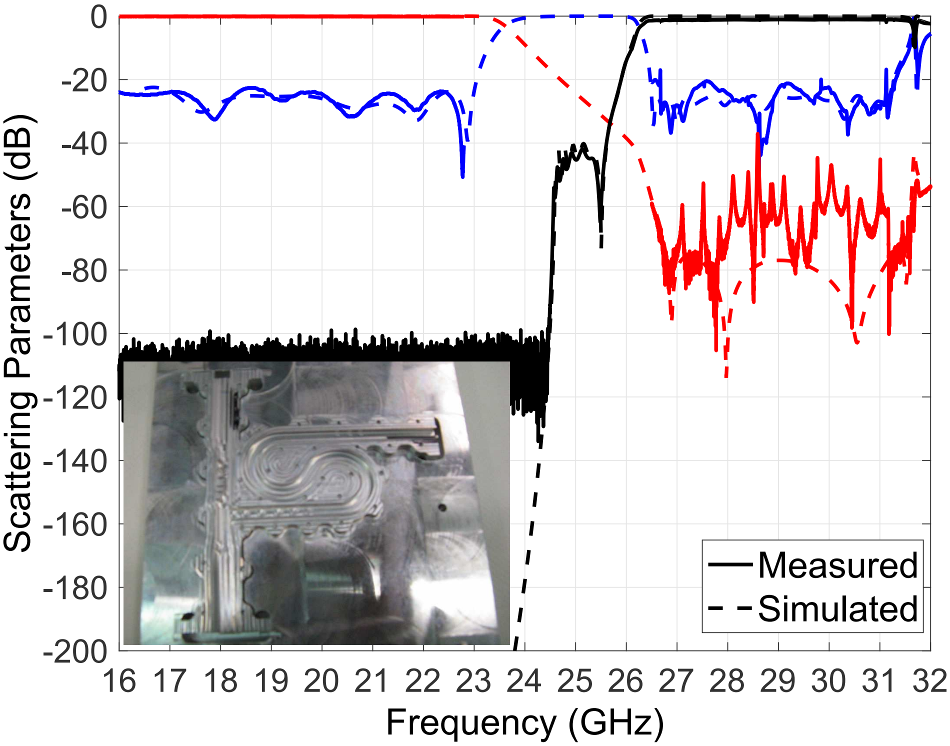

Figure 4.15: Comparison between the FEST3D simulated response and the measurements.

(see Table 4.1), with insertion losses ranging between 0.45 and 0.6 dB. The slight impairment in the return and insertion losses (however not problematic for PIM application) is attributed to the long meandered high-pass section. Additional scalar electrical measurements conducted with a spectrum analyzer demonstrated that the isolation between the input (common) port and the uplink (PIM) port of the diplexer in the downlink band was above 160 dB, the limit of the measurement set-up. Note that the use of a BPF represents a trade-off between size and insertion losses. Finally, the power handling capabilities of the diplexer were simulated and checked to be several dB above the 270 W CW requirement.

Chapter 5

Experimental Results

Several PIM measurement set-ups based on the architectures already presented in Chapter 3 were designed and developed following the theory and the guidelines described in Chapter 4. In addition, some of the multiplexers/diplexers implemented have been published as application examples of advanced multiplexing devices and wideband design techniques [69, 70, 72, 78].

This chapter is focused on the PIM performance of the test beds, showing the outstanding results obtained in real test campaigns, both for conducted and radiated scenarios.

5.1 Conducted forward PIM test bench

A test bench designed for evaluating conducted forward PIM at K/Ka-bands was designed and manufactured. The test bed architecture is depicted in Fig. 3.2 and a picture of the final test bed assembly is shown in Fig. 5.1. The frequencies covered by the high power transmission channels (downlink) and the PIM channel (uplink) are chosen in agreement with the ITU Regulations for satellite payloads [6], as shown in Table 5.1.

Downlink channels			**Uplink channels**	
Tx1 [GHz]	**Tx2 [GHz]**	**Tx3 [GHz]**	**Rx [GHz]**	**PIM order**
17.3 – 18.0	18.8 – 20.2	21.0 – 22.0	27.0 – 31.0	5th, 7th, 9th 11th, 13th at least

Table 5.1: Frequency bands of the conducted PIM forward set-up at K/Ka-bands.

As it can be observed in the general schematic in Fig. 3.2, the set-up is composed by two main blocks. The first one is an input triplexer placed before the

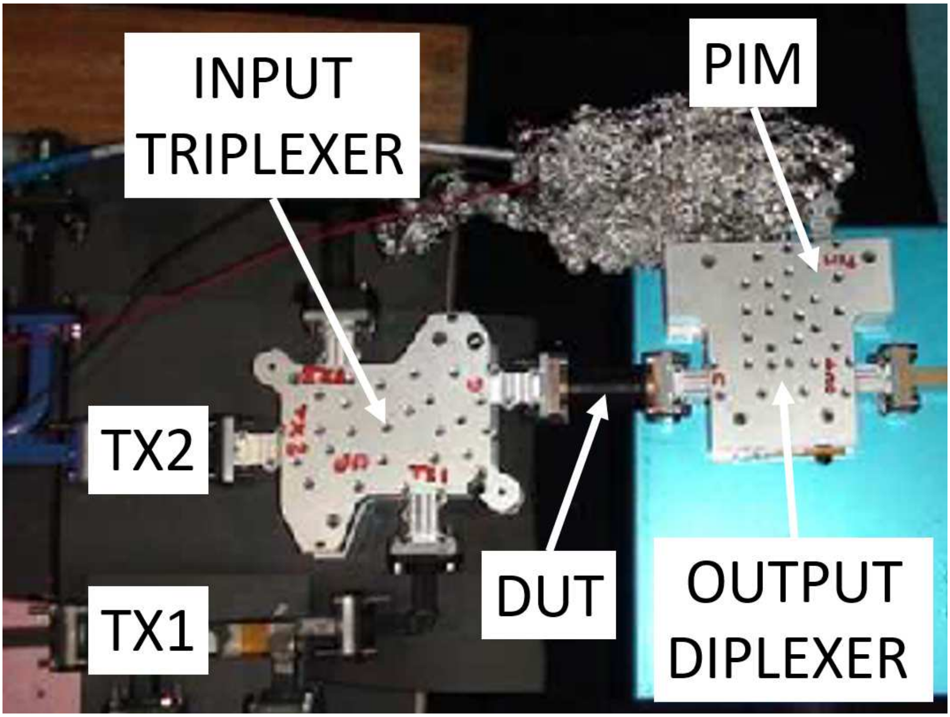

Figure 5.1: K/Ka-band set-up assembled for collecting forward conducted PIM.

Device Under Test (DUT). Its task is to combine up to three RF high power input carriers at K-band (ranging from 17.3 to 22 GHz). The mixed signal at the output of the triplexer will be injected into the DUT. The filters of the triplexer were implemented in MHFRW technology, following the design rules introduced in Section 4.1.

Figure 5.2(a) shows the internal design of the triplexer, where the MHFRW topology for the transmission filters may be appreciated. In Figures 5.2(b) and 5.2(c) the manufactured triplexer is shown, which includes a clam-shell (two-halves) assembly, the employment of grooved (high pressure) flanges, and the use of two metallic base plates (one for each side of the clam-shell) to give mechanical sturdiness to the structure.

The electrical response of the triplexer is shown in Fig. 5.3. Despite the high frequencies involved, the triplexer channels have in-band insertion losses lower than 0.5 dB. This is a clear benefit of the proposed integrated solution versus typical solutions composed by a cascade connection of several elements. The out-of-band response of the filters, however, showed unexpected spikes due to internal TE_{10} to

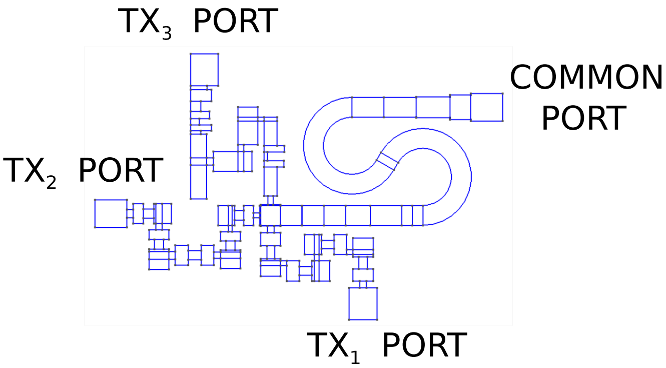

(a) Internal design

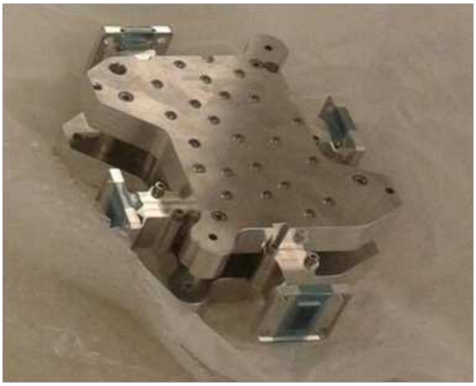

(b) Manufacturing - assembled structure

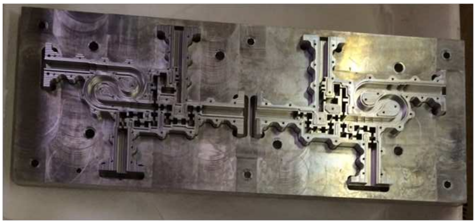

(c) Manufacturing - clam-shell parts

Figure 5.2: Combining triplexer in waveguide technology for evaluating conducted forward PIM at K/Ka-bands.

TE_{20} to TE_{10} conversions in the structure, which were not successfully reflected by the meandered high-pass filter section placed between the main junction and the common port of the multiplexer. Note that the filters were implemented in WR51

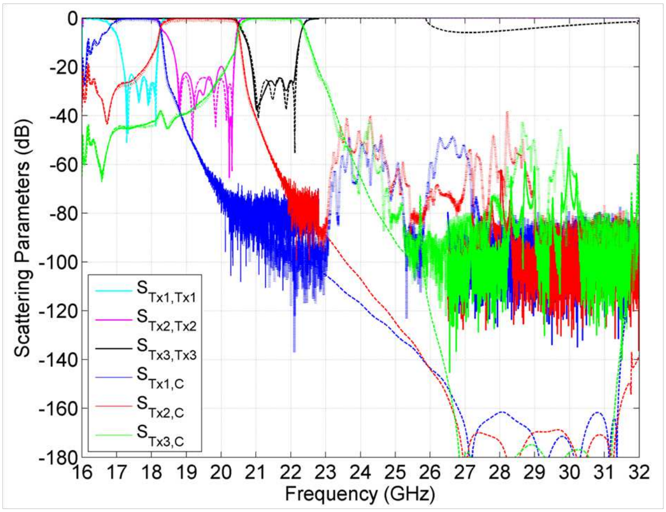

(a) Overall bandwidth

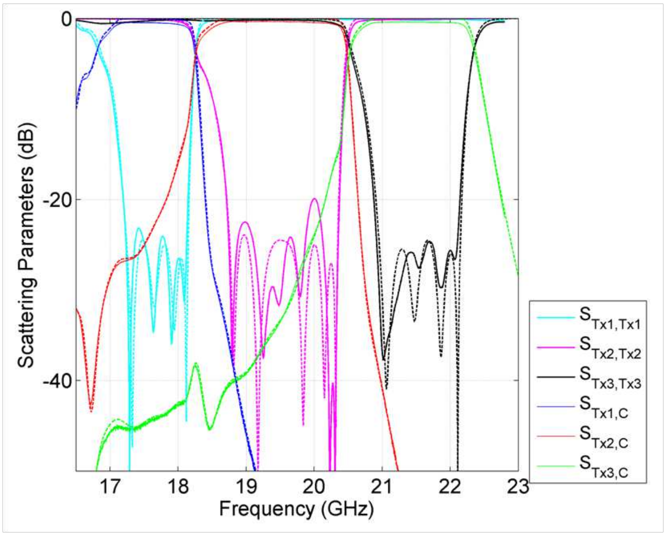

(b) Only transmission (downlink) bandwidth

Figure 5.3: Waveguide triplexer for evaluating conducted forward PIM at K/Ka-bands - electrical response (continuous and dashed lines represent measured and simulated responses, respectively).

waveguide. Although the obtained rejection may be enough, since the undesired signals generated by the High Power Amplifiers at such a far reception band should be small, an external low-pass filter was also designed and manufactured to increase the rejection if needed.

The second block is composed by the output diplexer placed after the DUT. This element, already presented in Section 4.3, is connected to the output of the DUT and covers a wide frequency band ranging from 17.3 GHz to 31 GHz. The diplexer is able to separate the PIM contribution at Ka band (from 27 to 31 GHz) from the input carriers, as shown in Fig. 4.15.

5.1.1 Choice of the test scenario

Depending on the choice of the transmission carrier frequencies, several PIM orders can be collected at the PIM reception port (at least, all the odd PIM orders from 5th to 13th).

The verification of the test assembly was conducted for two transmission carriers and the 7th order PIM, as this is the classical scenario for K/Ka-band satellite payload operation. In particular, two CW carriers at 17.5 GHz (first triplexer channel) and 20 GHz (second triplexer channel) were used. The problematic 7th order PIM contribution therefore falls at $4f_{\mathrm{Tx2}} - 3f_{\mathrm{Tx1}} = 27.5$ GHz.

5.1.2 RF power calibration procedure

After defining the test scenario, the next step consists in calibrating the test set-up in order to measure reliable RF power and PIM levels.

The procedure applied to calibrate both the transmission and the PIM channels is based on a measurement technique developed at the ESA-VSC European High Power RF Space Laboratory, which is consistent with the one already described in [5]. This measurement technique can be summarized here below.

Referring to Fig. 3.2, such a procedure considers as reference plane for the transmission carriers (downlink) the output port of the input triplexer. This is equivalent to the DUT input RF port. The calibration procedure, executed one at a time for each transmission channel, consisted in by-passing the HPA and injecting a signal of around +10 dBm in the transmission channel under consideration. Then, the offset between the reference plane and the plane on which the power sensor was placed in the set-up was measured, at the corresponding transmission frequency. Each offset measured was added to the reading of the corresponding power sensor.

On the other hand, for the PIM signal (uplink) the reference plane was the input (common) port of the output diplexer, which corresponds to the output port of the DUT in the real test scenario. The calibration procedure for the PIM channel was different to the one employed for the transmission channels, due to the weaker signals involved. It consisted in injecting a zeroed weak carrier at the PIM frequency (around -90 dBm) through the input port of the output diplexer, and then measuring the signal at the spectrum analyzer (SA) connected by means of a low noise amplifier (LNA) to the diplexer uplink output port. The offset resulting was subtracted to the reading provided by the SA, because the LNA amplifies the PIM signal.

It can be observed that the reference planes for transmission carriers and PIM signal measurements are slightly shifted. Being the PIM band quite separated from the one of the carriers, the electrical response of the DUT may attenuate/reject the PIM signal, and so affect the calibration. This effect is not present for a PIM signal reference plane placed at the output of the DUT (i.e. input of the diplexer). On the other hand, the DUT is always pass-band at downlink frequencies with consequent low insertion losses so, for the downlink band, the reference plane at the input of the DUT is basically equivalent to the one at the output of the DUT (and we may assume the output of the DUT as the global reference plane, if needed).

5.1.3 Optimization of the low PIM test bed

Prepare the test-set to read PIM signals is not an easy task, since several settings are necessary. To understand how correctly tune the test bed, it is important to enumerate the main characteristics of the PIM signal:

1. PIM is a permanent perturbation.

2. PIM signal is weak, typically close to (or even lower than) the Spectrum Analyzer sensitivity.

3. PIM signal is expected at determinate frequencies.

4. PIM signal is generated from carriers' amplitude.

For each point enumerate above, several actions must be taken in order to optimize the PIM reading.

1 - PIM is a permanent perturbation. An eventual PIM signal, when present, is permanent, hence the Spectrum Analyzer speed reading (sweep time) can be sacrificed in order to enhance the sensitivity.

2 - PIM signal is weak, typically close to (or even lower than) the Spectrum Analyzer sensitivity. The PIM signal is read by a Spectrum Analyzer (SA). Figure 5.4 shows the front-end of a typical SA in sweep mode. In order to detect an eventual PIM signal, the following two points must be guaranteed:

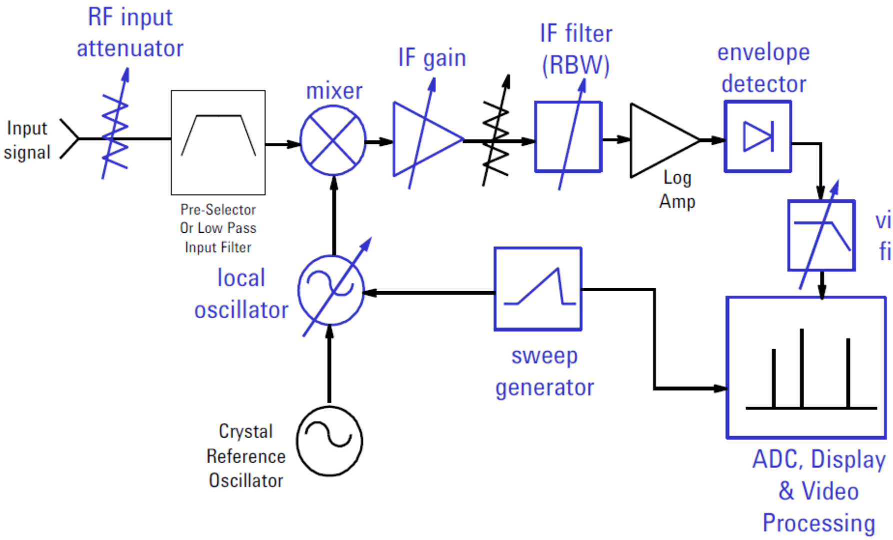

Figure 5.4: Typical block diagram of a Spectrum Analyzer in sweep mode.

- A low noise amplifier (LNA) having a high gain G (typically $G \approx 30$ dB or greater) must be inserted in the reception (PIM) path, in order to have at the Spectrum Analyzer a signal greater than its noise floor.
- The Spectrum Analyzer (SA) front-end must be set to maximize its sensitivity. Hence:
  - The **resolution bandwidth** (RBW) must be minimized (RBW set to 1 Hz, typically).
  - The **sweep time,** even though not critical given the permanent nature of PIM (see above), should be however minimized as far as possible, in order to guarantee a continuous witnessing of the test (1 second or less is recommendable). The reduction of the sweep time is in trade-off with the RBW, which might lead to an uncalibrated (”UNCAL”) reading of the spectrum analyzer. The ”UNCAL” must be avoided, since it might add inaccuracy to the PIM reading.
  - The **RF input attenuator** must be minimized, providing that the internal mixer overloading is avoided (note that a mixer overloaded generate undesired non-linear distortion).
  - The **envelope detector** is typically set in normal operation, which guarantees a compromise between signal and noise readings.

  - The **video bandwidth** does not affect the signal reading, but it can smooth the signal displayed. Typically, it is set in automatic mode.
  - In the receiver path, **the PIM filters and the LNA must be placed as close as possible to the PIM detection reference plane**, in order to strengthen the PIM signal. The LNA must be placed always after the PIM branch filters, in order to amplify the PIM signal only.

3 - PIM signal is expected at determinate frequencies. An erratic external reference in the Spectrum Analyzer can shift the PIM reading and give erratic PIM evaluations. **The spectrum analyzer must have the same external reference of the carrier signal generators.** In addition, always set one carrier signal generator as master and the Spectrum Analyzer as sleeve.

4 - PIM signal is generated from carriers' amplitudes. In a Spectrum Analyzer, in order to detect a "true" PIM signal generated by the DUT (device under test), it must be guaranteed that:

- For each transmission path, each carrier signal must be generated as free-spurious as possible. This is important to avoid any residual signal from the high power amplifier (HPA) which might mask the effective PIM signal. Typically, the spurious response of an HPA in saturation is in the order of -50 dBc in bands close to the transmission carriers. Since around 200 dBc are requested between carriers and PIM, the transmission filter must provide around 150 dB of rejection in the PIM band. A typical test to check whether the filtering in the transmission channels is enough, consists in switching-on each transmission carrier separately (i.e., one carrier at a time) and check that the SA noise floor at the PIM frequency is not affected. In case SA detects some variation in the amplitude reading, the filtering of the corresponding transmission channel is not enough. This issue can be solved by adding an additional band-pass/low-pass filter in cascade to the transmission channel. Such a filter must let pass the transmission carrier frequency and simultaneously provide high rejection at the PIM frequency band.

- In the receiver (PIM) path, the PIM signal must pass whilst the carrier signals have to be strongly attenuated. This is important to avoid the generation of active intemodulation (AIM) at the LNA, which can mask the effective PIM to be detected. Laboratory measurements performed in several LNAs showed that these components may generate significant AIM levels when the RF power of the carriers at the LNA input is above -70 dBm. Considering that the carrier amplitude is around 53 dBm/carrier, the PIM channel should provide a rejection in the range of 130 dB or higher. The rule-of-thumb test to check enough filtering in the PIM channel has been

	Tx 1	**Tx 2**	**7^{th} order PIM**
Frequency (GHz)	17.5	20.0	27.5
RF levels (dBm)	52	52	≤ -165 (*)

(*) After thermal stabilization

Table 5.2: Conducted forward PIM at K/Ka-bands, set-up validation results.

carried out, consists in switching-on each carrier separately with maximum power, and check the SA does not detect the carrier. If a variation in the amplitude of the SA reading is observed at the carrier frequency, a notch filter in cascade to the PIM channel is required. The filter pass-band must cover the PIM frequency and provide high rejection at the frequencies of the carriers.

5.1.4 Set-up validation

Once the power calibration has been performed, the next step is validating the test facility with no DUT in place, in order to measure the residual PIM noise floor of the test set-up. Note that the reference planes for downlink and uplink coincide for the validation of the test facility (as the DUT is not inserted).

For the K/Ka-band PIM set-up and the test scenario under consideration (see Section 5.1.1), the validation results are provided in Table 5.2. To perform this validation, a 10 cm length straight WR51 waveguide section, manufactured in a single piece and with suitable low PIM flanges (i.e., having low PIM performance), was inserted between the input triplexer and the output diplexer in order to consent the physical connection between these two components. As a consequence, this short low PIM waveguide section can be assumed as part of the set-up.

Two RF input carriers delivering 160 W CW each were injected through their corresponding input channels of the multiplexer, and the 7^{th} order PIM product at 27.5 GHz (conducted forward PIM contribution) was measured at the uplink port of the output diplexer. Figure 5.5 shows the evolution of such a PIM signal versus time. Once both RF carriers were increased to 160 W CW, a PIM level of −160 dBm was measured. Nevertheless, after awaiting some minutes for the thermal stabilization of the set-up, the detected PIM level decreased to the range between −165 dBm and −168 dBm. Therefore, the residual 7^{th} order PIM level of the measurement test bed was below -165 dBm (see Table 5.2), being an unprecedented value for high-performance PIM test beds (see Section 20.7.1 in [5]).

The PIM level obtained is outstandingly low, very close to the thermal noise floor (PNT) of the facility. Indeed, the thermal noise floor for a 1 Hz resolution bandwidth B and a source noise temperature T_{s} of 20 °C (293 K) is given by:

$$\mathrm{PNT} = 10\log_{10}\left(\kappa \mathrm{B} T_{\mathrm{s}}\right) + 30 = -174 \text{ dBm} \tag{5.1}$$

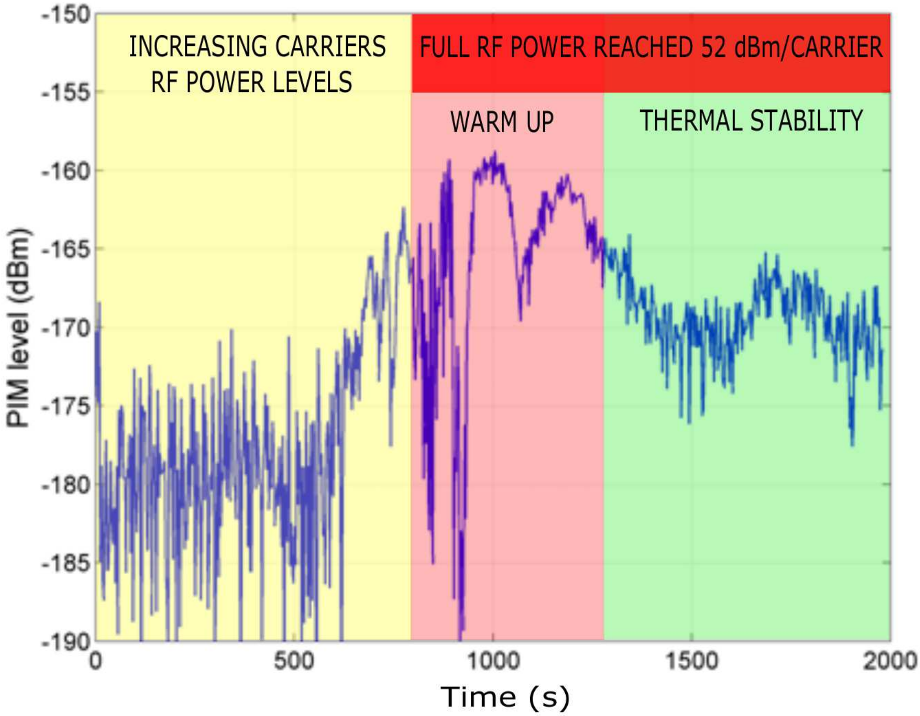

Figure 5.5: Evolution of 7th order PIM level versus time for the K/Ka-band PIM setup with two input carriers of 160 W CW each and no DUT (blank scenario to validate the PIM noise floor of the set-up).

where κ is the Boltzmann constant. The noise contribution of the LNA assembly must also be incorporated. Taking into account that the insertion losses introduced by the reception PIM branch is 0.6 dB, the LNA parameters are $NF_{\text{LNA}} = 4$ dB (or, equivalently, $f_{\text{LNA}} = 10^{0.4} = 2.51$ in linear units) and $G_{\text{LNA}} = 30$ dB, and the insertion losses of the cable connecting the LNA to the Spectrum Analizer are 1 dB, the noise factor of all the PIM reception assembly is given by the classic Friis formula [20]:

$$\begin{aligned} f_{\text{PIM}} &= f_{\text{filter}} + \frac{f_{\text{LNA}} - 1}{g_{\text{filter}}} + \frac{f_{\text{cable}} - 1}{g_{\text{filter}} g_{\text{LNA}}} \approx 2.88 \\ NF_{\text{PIM}} &= 10 \log_{10} \left(f_{\text{PIM}} \right) \approx 4.6 \text{ dB} \end{aligned} \tag{5.2}$$

where it has been exploited the fact that a passive component operating at ambient temperature has a noise figure similar to its insertion losses [20].

The effect of the noise of the PIM reception branch can be incorporated to (5.1), thus obtaining

$$\mathrm{NoiseLimit} = 10\log_{10}\left(\kappa \mathrm{B}\left(T_{\mathrm{s}} + T_0\left(f_{\mathrm{PIM}} - 1\right)\right)\right) + 30 = -169.4 \text{ dBm} \tag{5.3}$$

which is very similar to the noise level measured in the Spectrum Analyzer after reaching thermal stability. This same noise floor with 1 Hz RBW was observed in real radiated tests at ESA ESTEC Compact Test Range facility [105], thus suggesting that the measurement might be limited by thermal noise rather than residual PIM originated in the set-up. A PIM test bench for detecting 7th order PIM contributions with similar performance has not been reported in the technical literature previously.

5.1.5 Set-up verification

Finally, the effective capability of the PIM test set-up to detect weak PIM signals must be checked. This can be done by inserting a sample having well known PIM performance in place of the DUT. For waveguide components, off-the-shelf samples are available, such as flexible waveguides and standard UBR flanges. These samples have been proved to ignite significant PIM with moderate RF power levels in the transmission carriers.

For the PIM test bench under consideration, a short section of WR51 flexible waveguide was inserted as DUT. A PIM signal of −113 dBm was detected in the spectrum analyzer with only 5 W of power per continuous wave (CW) carrier. This experimental result fully validates the PIM test bed assembly, which can be used for a real PIM measurement campaign.

5.2 Conducted backward PIM test benches

Three different test set-ups were designed and manufactured for performing conducted PIM measurements in backward configuration, according to the novel architecture presented in Section 3.2.2 which follows the schematic depicted in Fig. 3.3.

5.2.1 C-band test set-up

The first one is a test bed operating at C-band, which covers almost the whole WR229 operational frequency range (3.4-4.8 GHz). The set-up is able to mix up to three different transmission carriers and separate the PIM signal in reflection, according to the specifications given in Table 5.3.

The core of the test bed is a four channel waveguide multiplexer having standard WR229 rectangular waveguide ports. The multiplexer presents three high-power input channels ranging between 3.41 and 4.25 GHz, plus one reception

Downlink channels			Uplink channels	
Tx1 [GHz]	**Tx2 [GHz]**	**Tx3 [GHz]**	**Rx [GHz]**	**PIM order**
3.41 – 3.60	3.82 – 3.97	4.14 – 4.25	4.5 – 4.85	3rd, 5th, 7th 9th at least

Table 5.3: General specs for the conducted PIM backward set-up at C-band.

	Tx 1	**Tx 2**	**3rd order PIM**
Frequency (GHz)	3.58	4.17	4.76

Table 5.4: Conducted backward PIM at C-band, test scenario.

	Tx 1	**Tx 2**	**3rd order PIM**
Frequency (GHz)	3.58	4.17	4.76
RF levels (dBm)	50	50	≤ -137

Table 5.5: Conducted backward PIM at C-band, test results.

channel covering the bandwidth between 4.5 and 4.85 GHz. Depending on the choice of the transmission carriers, several odd PIM orders (3rd, 5th, 7th and 9th) can be detected in the PIM reception band. The overall insertion losses were again below 0.5 dB for all the input channels. HFRW filters were employed for the transmission channels, being the filter for the first channel the one already described in Section 4.1.1 with SIR resonators. For the other two channel filters, WR229 rectangular waveguide cavities were used (the separation with the PIM reception band was lower, so the spurious pass-band related to the TE_{102} cavity mode does not limit the rejection in the PIM band), and a low-pass filter was integrated at each input to satisfy the rejection requirements. On the other hand, the reception filter is the one outlined in Section 4.2. The assembled set-up is shown in Fig. 5.6.

The test frequencies and PIM order applied for testing are spotted in Table 5.4. As it can be observed, the 3rd order PIM, the most critical one, was evaluated.

The test bed was calibrated measuring the offsets both for the transmission carriers and the PIM channel. The same calibration procedure described in Section 5.1.2 was applied. The reference plane, both for the transmission carriers and the PIM signal, was the common port of the multiplexer, which corresponds to the input port of the DUT in a real test scenario.

After assembling the test bench and optimizing its configuration, a PIM measurement was carried out for a straight WR229 waveguide section acting as DUT (see Fig. 5.6). The results are detailed in Table 5.5.

As it can be observed, two input RF tones delivering high power were injected into the set-up whilst the 3rd order PIM was evaluated. The residual PIM level of

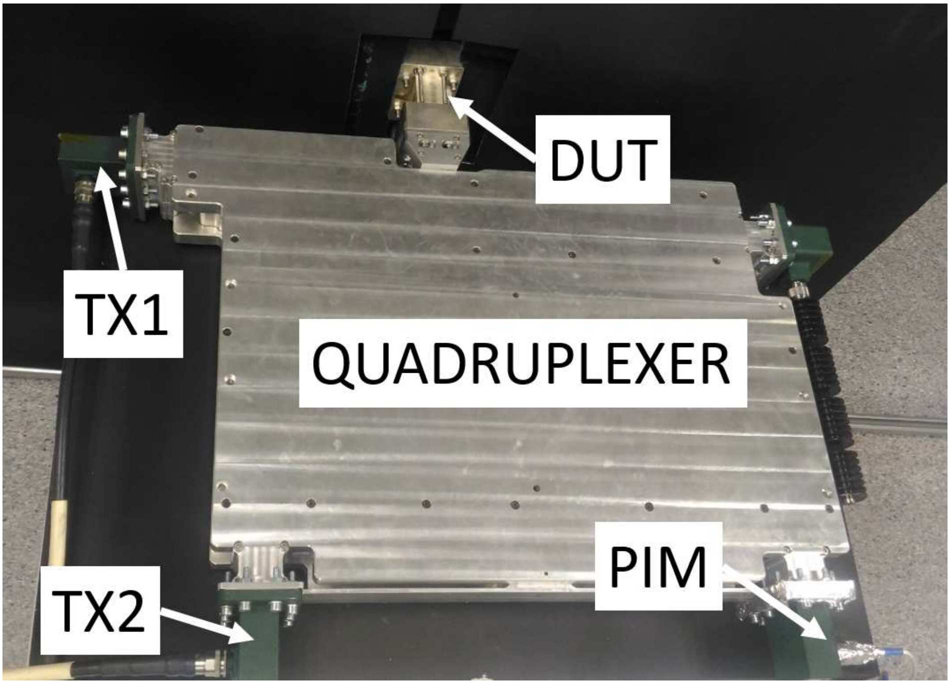

Figure 5.6: C-band setup assembled for testing backward conducted PIM.

the test set-up was quite good considering the PIM order evaluated (187 dBc of dynamic range between carriers and PIM), although it was a few dB higher than expected. This small deviation could be attributed to the quiet load rather than to the multiplexer itself, which may be a limiting point for waveguide PIM set-up architectures in backward configuration (as detailed in Section 3.2.2.1).

In any case, the test bench is still fulfilling test requirements for payload satellite hardware, being the residual PIM level of the facility 15 dB lower than typical PIM specification at C-band (as reported in the last sentence of section 1.8.4 in [5]).

This test set-up was successfully used in several PIM test campaigns, including the one aimed at evaluating the 3rd order PIM level generated by three input carriers reported in [106]. The low PIM multiplexer also showed flexibility, being able to attend several power handling test campaigns. For instance, it has been used to test high power waveguide loads to be used as dummy termination for payload satellites in ground level tests. In this particular case, the multiplexer was able to mix three RF carriers (one for each transmission channel), achieving an aggregated RF mean power level of 2000 W at its common port.

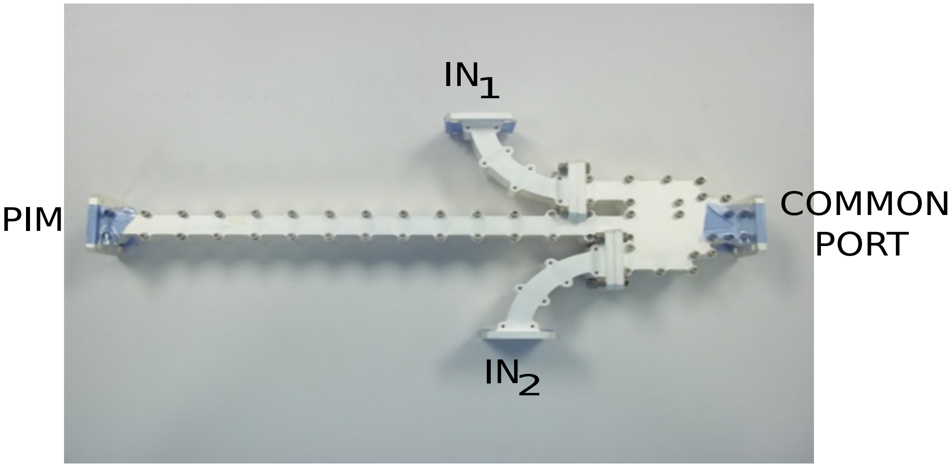

Figure 5.7: Ku-band triplexer for conducted backward PIM set-up.

Downlink channels		Uplink channels	
Tx1 [GHz]	**Tx2 [GHz]**	**Rx [GHz]**	**PIM order**
11.12 – 11.75	12.45 – 12.75	13.7 – 15.0	3rd, 5th, 7th 9th at least

Table 5.6: General specs of the conducted backward PIM set-up at Ku-band.

5.2.2 Ku-band test set-up

A second test bed for evaluating conducted PIM in backward direction was developed for the Ku-band. This set-up also follows the architecture proposed in Section 3.2.2. The core of the test bed is the low PIM triplexer shown in Fig. 5.7 (two transmission channels, one PIM channel) designed in a joint collaboration between ESA-VSC European High Power RF Space Laboratory and UPV-GAM research group [107].

The triplexer was designed to fulfill ESA Small Geo Payload scenario, see Table 5.6. Depending on the frequencies of the high power carriers, several odd PIM orders can be collected at the PIM port.

The transmission filters of the triplexer were designed in HFRW topology given the proximity between the transmission and the PIM bands, and were backed-up by low-pass filters to satisfy the rejection requirements. As far as reception concerns, the PIM channel consisted in a high-pass filter solution. Since all RF ports of the triplexer are in WR75 standard waveguide, the parameter limiting the maximum frequency for the PIM channel is given by the monomode range of the WR75

	Tx 1	**Tx 2**	**3^{rd} order PIM**
Frequency (GHz)	11.468	12.735	14.002

Table 5.7: Conducted backward PIM at Ku-band, test scenario.

	Tx 1	**Tx 2**	**3^{rd} order PIM**
Frequency (GHz)	11.468	12.735	14.002
RF levels (dBm)	52	52	≤ -145

Table 5.8: Conducted backward PIM at Ku-band, test results.

waveguide (i.e., slightly above 15 GHz).

The triplexer was manufactured in clam-shell technology in aluminum and was silver plated. The use of silver for the surface improves PIM mitigation, at the cost of increasing the electrical response deviations due to the highest manufacturing tolerances (the final tolerance of the piece was around ±15 µm). In this case, neither the filters were extremely sensitive nor the component was bulky (limiting the economical cost), so a silver plating finish was feasible.

The set-up was employed for evaluating conducted backward PIM with the scenario stated in Table 5.7. As it can be noticed, the 3^{rd} order PIM, the most critical one in the reception band, was evaluated.

Considering the common port of the triplexer as the reference plane, and applying the standard calibration procedure detailed in Section 5.1.2, a first test was conducted having a WR75 straight waveguide section (a 20 mm length spacer) as DUT. This spacer was silver plated and manufactured with high pressure flanges following the design rules detailed in [17], in order to mitigate any PIM coming from this piece and its flanged interconnections.

The measured results for 3^{rd} order PIM with two input CW carriers delivering 160 W each are detailed in Table 5.8. As it can be observed, the set-up showed outstanding residual PIM, around 197 dBc, for the most critical PIM contribution.

The results obtained for 3^{rd} order PIM are equivalent to the the state-of-art PIM measurements performed at Ku-band for conducted forward PIM (see [18], and section 20.7.1 in [5]), in spite of being unprotected for the PIM generated by the quiet load. In addition, the proposed integrated set-up architecture presents several advantages when compared with a classic set-up composed of the cascade interconnections of several blocks, in terms of compactness, flexibility, easier assembly, lower insertion losses, less return loss degradation, and avoidance of unwanted spurious resonances.

At a later stage, the same test bed was employed to measure higher PIM orders such as the 5^{th} and the 7^{th} ones. The residual noise floor was below -152 dBm in both cases, being probably limited again by the residual noise floor of the quiet

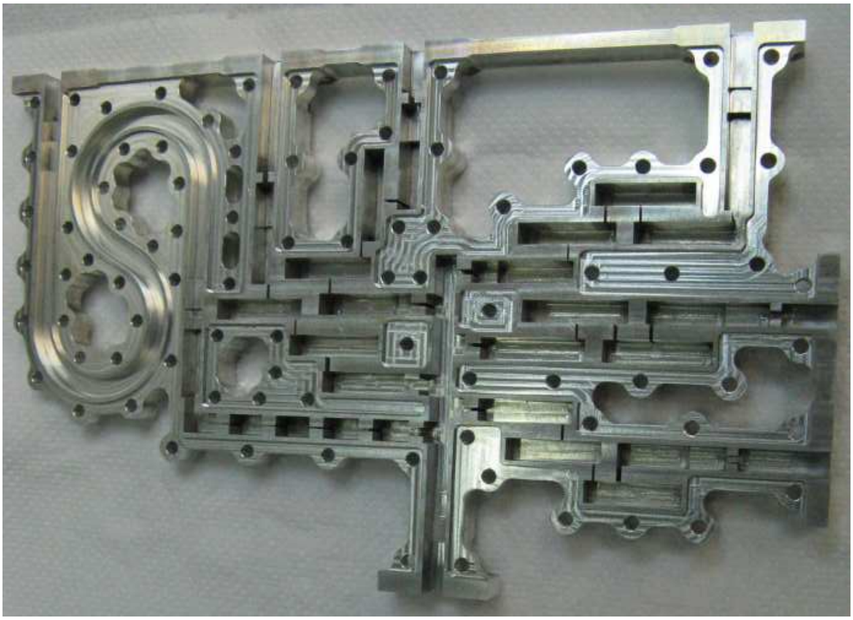

Figure 5.8: Six-channel multiplexer for conducted backward PIM set-up at K-band.

load employed in the test set-up.

The proposed set-up was largely employed in several test campaigns carried out at ESA-VSC laboratories, in order to measure the PIM performance of a large class of devices under test (waveguide couplers, isolators and filters) for satellite communications, and also at proto-flight model (PFM) level.

5.2.3 K-band test set-up

The last test bed presented in this section consists in a conducted backward PIM set-up for K-band, implemented again according to the block diagram shown in Section 3.2.2. The key element of the test bed is the six-channel multiplexer shown in Fig. 5.8. It is composed of five channels between 17.89 and 20.67 GHz for combining the input carriers, and a PIM channel covering the frequency range between 22.7 and 24.1 GHz. Each transmission channel has a bandwidth of 420 MHz and the separation between adjacent channels is 170 MHz. All the ports use standard WR42 waveguide (recommended operation range between 18 and 26.5 GHz) with UBR 220 flange.

Taking into account the separation between the transmission and PIM recep-

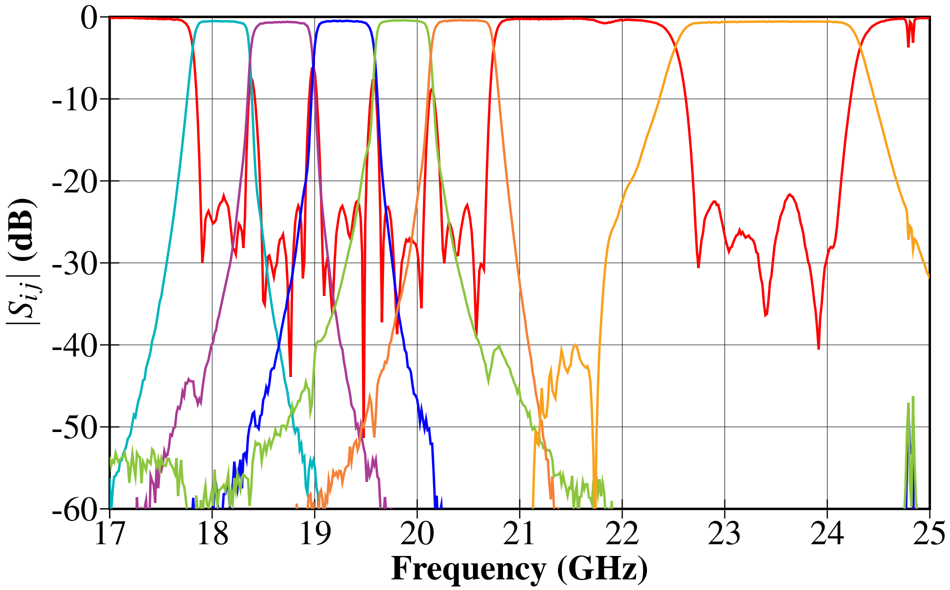

Figure 5.9: Electrical response of the K-band six-channel multiplexer.

tion band, MHFRW filters were finally considered for the transmission channels. TE_{102} cavities were used in order to increase the robustness to manufacturing, allowing a 4th order filter for a manufacturing tolerance of about ±7 µm. The PIM reception filter is composed of an in-line five order band-pass filter with TE_{101} cavities and a high-pass section. The multiplexer was manufactured in bare aluminum. Silver plating was not possible in this case, as it implies an unacceptable increase in the manufacturing deviations. Each MHFRW filter provides two transmission zeros, resulting in a PIM band rejection between 105 dB (closest transmission channel) and 140 dB (farthest transmission channel). As a result, an additional low-pass filter is required to satisfy the isolation requirements.

The S-parameter response of the full multiplexer, with the low-pass filter in place at the input of each transmission channel, is shown in Fig. 5.9. The return loss is better than 21.7 dB for all the channels, and the insertion losses are lower than 0.6 dB in almost all the transmission channel pass-bands.

Thanks to the high number of input channels, this multiplexer provides an outstanding flexibility in terms of PIM characterization. Any odd PIM order can be detected in the PIM reception channel with a suitable choice of the input carriers. In addition, several carriers can be combined simultaneously, obtaining an scenario more similar to realistic operation conditions.

A first set of measurement was performed to validate the 3^{rd} order PIM perfor-

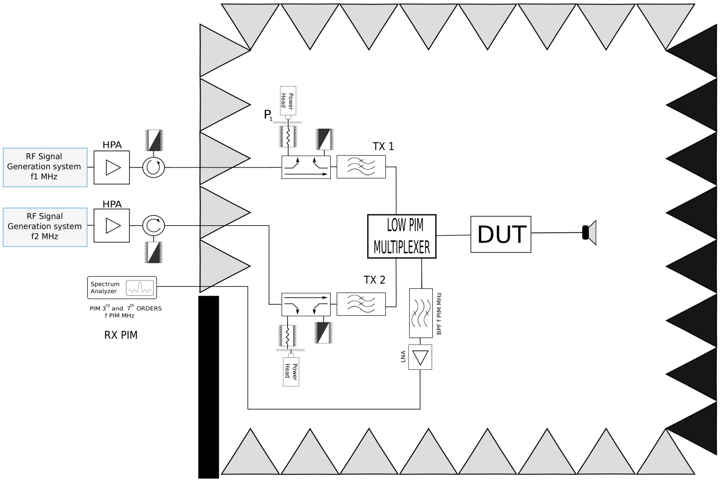

Figure 5.10: Schematic of the test bed for conducted backward PIM at K-band.

	Tx 1	**Tx 2**	**3^{rd} order PIM**
Frequency (GHz)	17.9	20.5	23.1

Table 5.9: Conducted backward PIM at K-band, test scenario.

	Tx 1	**Tx 2**	**3^{rd} order PIM**
Frequency (GHz)	17.9	20.5	23.1
RF levels (dBm)	48.2	48.2	≤ -117 without DUT
	48.2	48.2	≤ -101 with DUT

Table 5.10: Conducted backward PIM at K-band, test results.

mance of a WR51 waveguide isolator. The carriers were inserted at the first and last transmission channels. The test scenario is detailed in Table 5.9. A sketch of the test bench is available in Fig. 5.10. As it can be noticed, despite being a conducted PIM test, the test set-up was moved inside the anechoic chamber, so that the combination of a horn antenna plus the anechoic chamber walls was employed as the quiet load. This approach was followed since the measurements were carried out before the innovative solution proposed in Section 3.2.2.1 was developed (in fact, the results reported in such a section were obtained using this K-band test bench). Figure 5.11 shows photos of the test bed employed for this campaign.

The results obtained from the PIM measurement set-up are detailed in Table

(a) Part inside the anechoic chamber - multiplexer (b) Part inside the anechoic chamber - horn antenna

(c) Part outside the anechoic chamber

Figure 5.11: Test set-up assembled for testing conducted backward PIM at K-band.

5.10. As it can be observed, the residual PIM level of the test bench, despite widely enough for testing purposes, showed “only” 166 dBc between the transmission carriers and the PIM level. The reason of this behaviour was investigated, and it was found that the main PIM contribution was due to the waveguide flanges at the common port of the test bench and the horn antenna. Both flanges are standard UBR 220 flanges and do not follow the design rules detailed in [17].

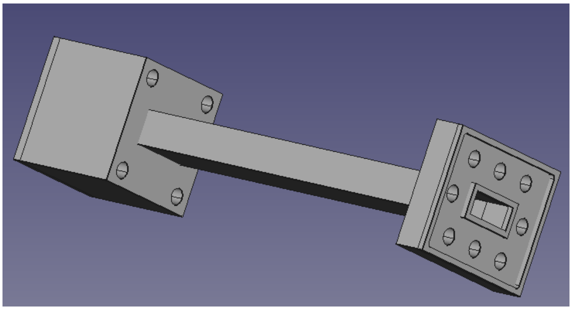

(a) Waveguide adapter CAD model

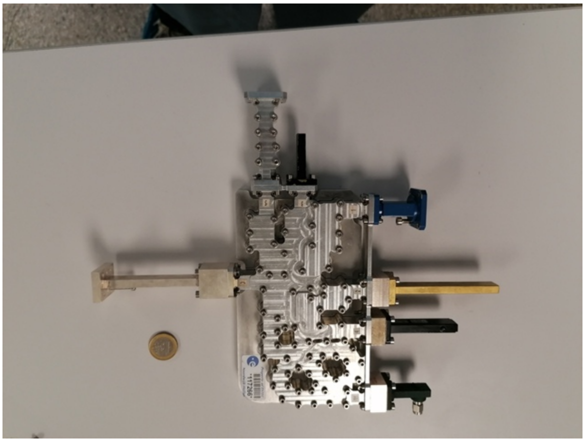

(b) Waveguide adapter placed at the common port of the multiplexer

Figure 5.12: Low PIM waveguide adapter designed at K-band.

As a consequence, a novel waveguide adapter able to be mated at the critical PIM places and complying with such design rules was designed (see Fig. 5.12). Two units were manufactured by electro-forming (i.e., single piece), and were silver plated in order to reduce as much as possible residual PIM. As it can be observed, the side mating of the UBR 220 flange is grooved and has a thickness of 20 mm, whereas the other side is only 7 mm thick but eight holes are present. One of the units should be inserted in the multiplexer-DUT connection, and the another one in the DUT-horn antenna connection.

The second set of measurements with these transitions in place indicated an additional PIM mitigation around 25 dB, as shown in Table 5.11. This result clearly points out the effectiveness of the novel adapter aimed at reducing the

	Tx 1	**Tx 2**	**3^{rd} order PIM**
Frequency (GHz)	17.9	20.5	23.1
RF levels (dBm)	47	47	≤ -145 without DUT

Table 5.11: Conducted backward PIM at K-band, test results after inserting the adapters in the test bed.

residual PIM in flanged interconnections.

5.3 Radiated test benches for measuring reflected PIM

5.3.1 Ku/Ka-band test set-up at Airbus CATR facility

The conducted PIM backward test set-up at Ku-band presented in Section 5.2.2 was initially conceived for measuring radiated PIM. The initial use of the set-up was to evaluate (and mitigate) the PIM performance of the Airbus Compact Antenna Test Range (CATR) facility located at Ottobrunn (Germany). This facility was used to perform the ground level testing of ESA Small Geo satellites before its launching.

The schematic of the PIM measurement set-up is illustrated in Figure 5.13, which follows the architecture described in Section 3.3 (see Fig. 3.9). The requirements for the test set-up coincide with the ones of ESA Small Geo satellites, including a 20 dB safety margin for PIM (see Table 5.12).

The PIM test bench was assembled and tested at ESA-VSC European High Power RF Space Laboratory before its moving to Germany, see Fig. 5.14. The quiet load placed at the common RF port of the triplexer was substituted by a WR75 horn antenna (20 dBi of isotropic gain) and the set-up was placed inside a low PIM anechoic chamber. The anechoic chamber should dissipate the radiated RF power without stimulating any PIM disturbance, which may mask the effective PIM signal to be measured. In other words, the anechoic chamber must provide a quiet environment for PIM, being at the same time able to fulfill its main task of dissipating the high-power RF carriers incident towards their cones. Furthermore, an additional sniffer antenna was added to the test set-up to collect the 10^{th} order PIM contribution at Ka-band, as this scenario was also critical in terms of PIM for the Small Geo satellite uplink. The performance of the facility was evaluated both for 3^{rd} and 10^{th} orders of PIM in a blank scenario (anechoic chamber walls). For the third order, the most critical one, the results were in line with the ones already reported in Table 5.8. For the tenth order, the residual PIM level was around -155 dBm.

	Tx 1	**Tx 2**	**3^{rd} order PIM**	**10^{th} order PIM**
Frequency (GHz)	11.468	12.735	14.002	30.538
PIM target (dBm)			≤ -110	≤ -110

Table 5.12: Radiated PIM at Ku/Ka-bands, test scenario.

The PIM measurement set-up was then moved to Airbus CATR facility, where it was installed in its payload displacer using a custom-designed dedicated support, as shown in Figure 5.15.

The test bed was placed at 1.16 m from the CATR wall. This scenario provides, using a transmission power of 52 dBm per carrier (see Table 5.8), a radiated power flux density at the CATR cones equivalent to the one generated by the satellite placed at the center of the CATR during the ground level tests. For such a distance from the CATR wall, the spot covered by the antenna mounted in the set-up is a circle of around 15 cm diameter, following simulations performed at ESA-ESTEC (see Fig. 5.16).

First, a verification of the test set-up was carried out, inserting a metallic sponge (typical strong PIM source) on top of the CATR wall, as shown in Fig. 5.17. With this sponge in place, the set-up detected a strong PIM with only few watts per carrier, demonstrating the sensitivity of the measurements system.

A complete scan of the CATR anechoic wall was then performed. PIM measurements were conducted twice, both in vertical polarization (V-pol, see Fig. 5.14(a)-5.14(b)) and horizontal polarization (H-pol, see Fig. 5.14(c)-5.14(d)). The skip from one polarization to the dual one was achieved by a routing scheme that allows a 90° rotation of the triplexer. The use of a 90° waveguide twist for the horn antenna was not suitable as the twist would be placed in the common RF path after combining the carriers, thus degrading the PIM performance of the set-up. The outcome of the test campaign is shown in Fig. 5.18 for both polarizations. The results for some particularly important spots are shown in Fig. 5.19.

No issues were detected for the 10^{th} order PIM, since the PIM level was always below the threshold level of -110 dBm. On the other hand, the test campaign was able to detect the areas of the CATR surface not compliant with the target specification of -110 dBm for the 3^{rd} order PIM. These areas were visually inspected after testing, and some burnt marks in some tips of the cones were detected. In addition, it was noticed that some panels were not perfectly aligned, causing an exposition to the RF power of the metallic frame sustaining the structure, with consequent PIM ignition. As a result of the test campaign, the non-compliant panels were replaced with new ones, and the disposition of the panels was changed in order to cover the parts of the metallic frame previously exposed to the RF signal.

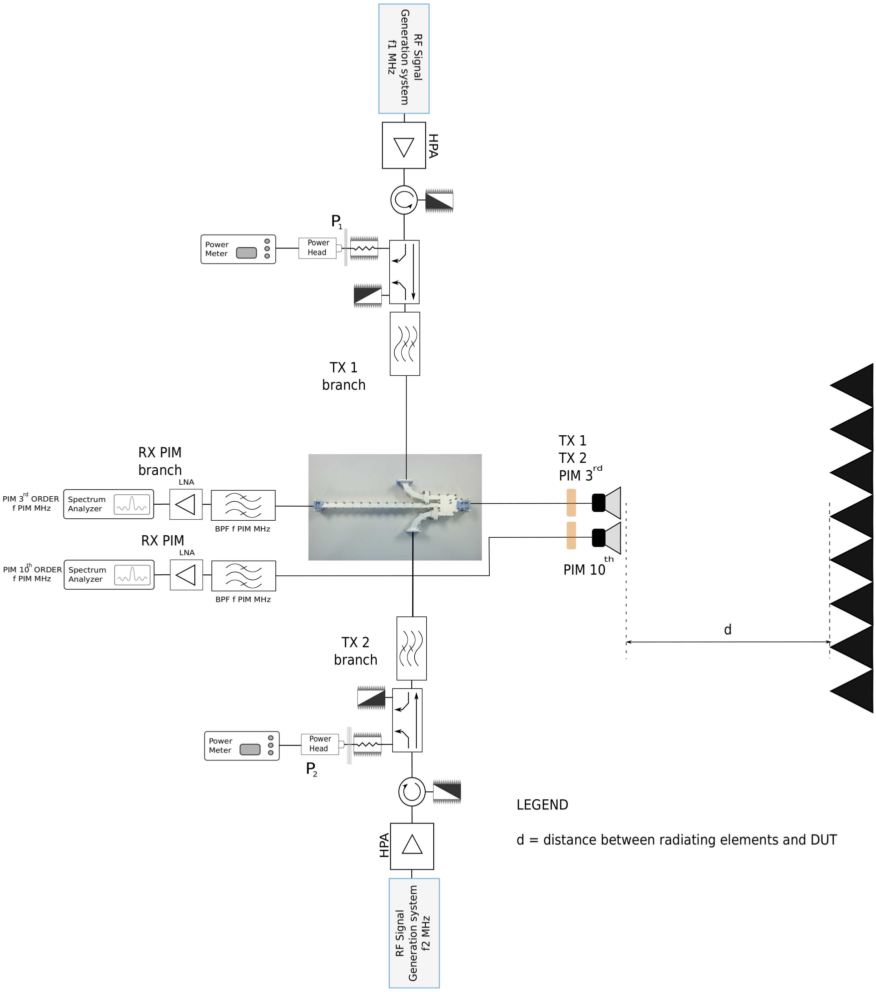

Figure 5.13: Schematic of the radiated PIM test bench for the test campaign at Airbus CATR facility.

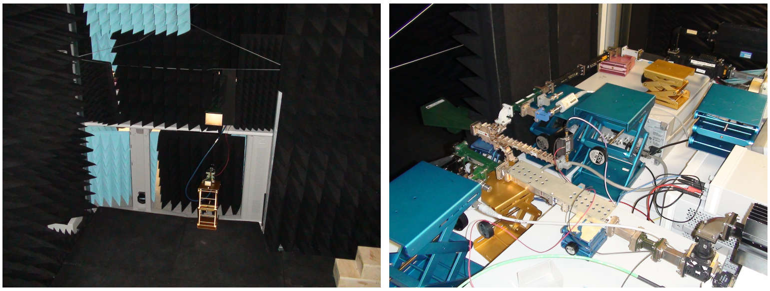

(a) Front side - V-pol (b) Inner side - V-pol

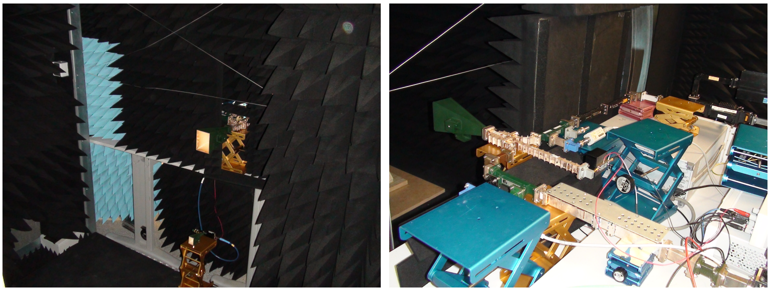

(c) Front side - H-pol (d) Inner side - H-pol

Figure 5.14: Ku/Ka-bands set-up assembled for testing radiated PIM. Assembly at ESA-VSC premises before its moving to Airbus CATR facility.

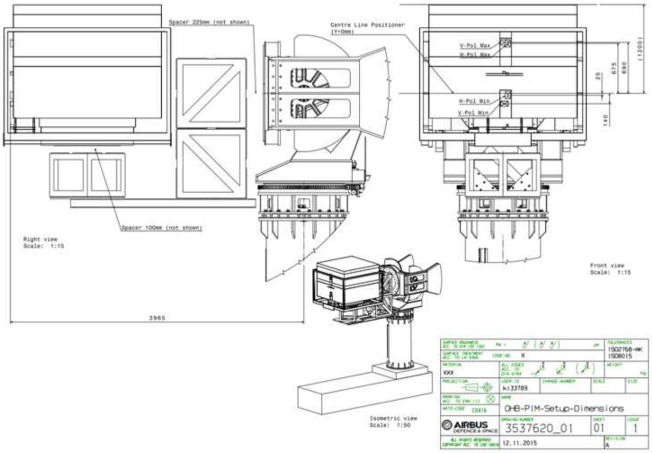

(a) Schematic of the support

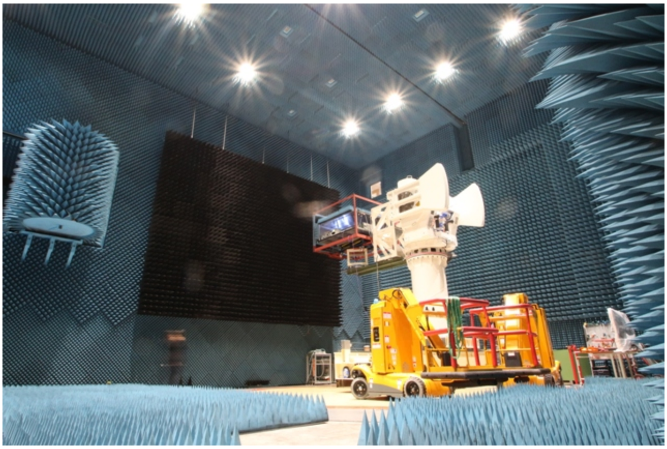

(b) Test bed installed in the positioner in front of the DUT

Figure 5.15: Ku/Ka-bands set-up at Airbus CATR facility.

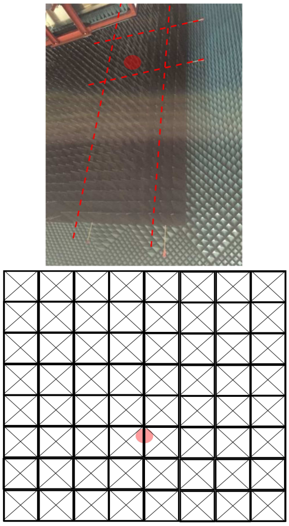

Figure 5.16: Typical spot covered by the set-up for each PIM measurement.

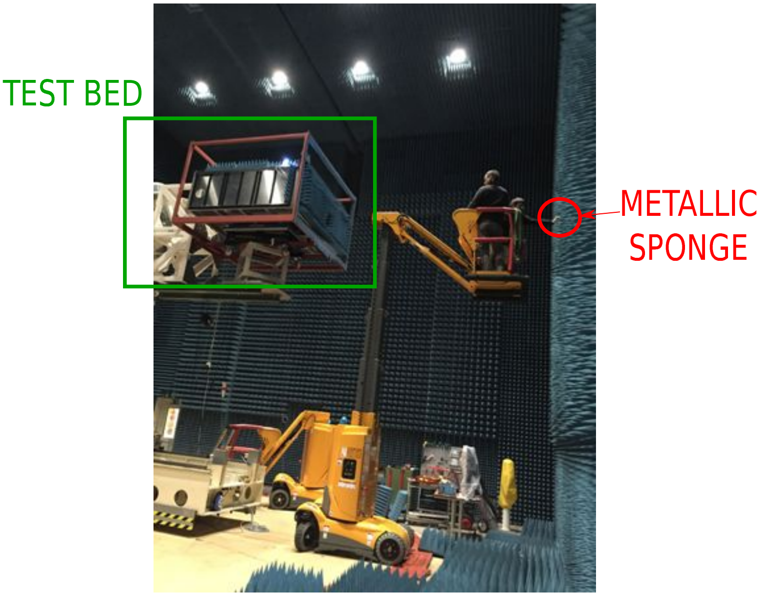

Figure 5.17: Placement of the metallic sponge on top of the DUT to check the sensitivity of the test bed.

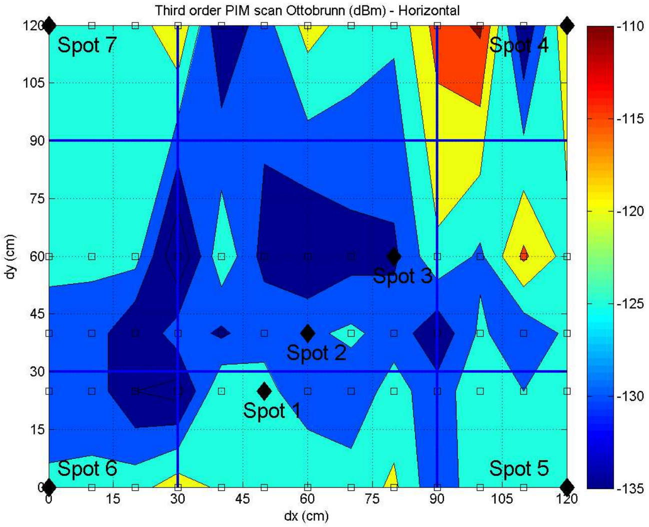

(a) Horizontal polarization

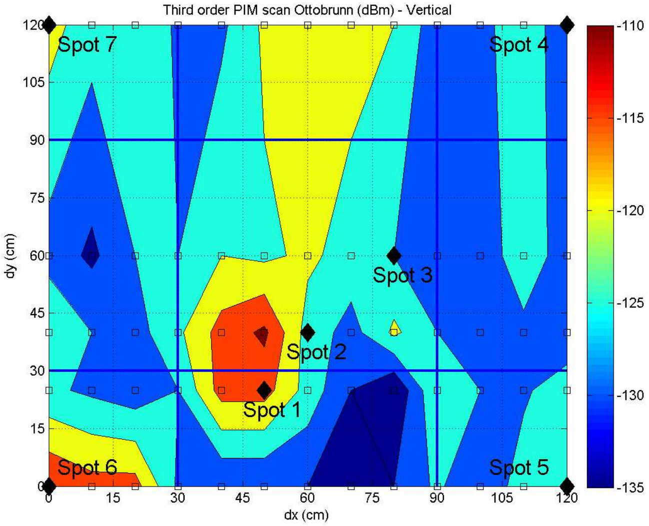

(b) Vertical polarization

Figure 5.18: Scan of the CATR area of interest for Small Geo ground level tests.

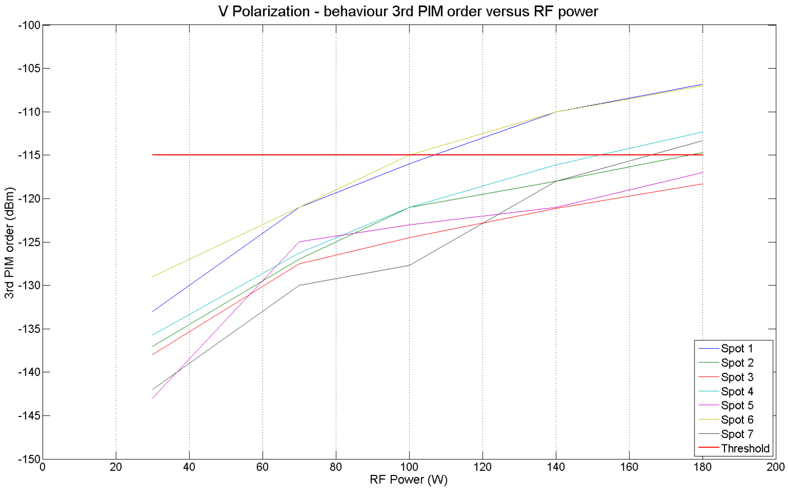

(a) Horizontal polarization

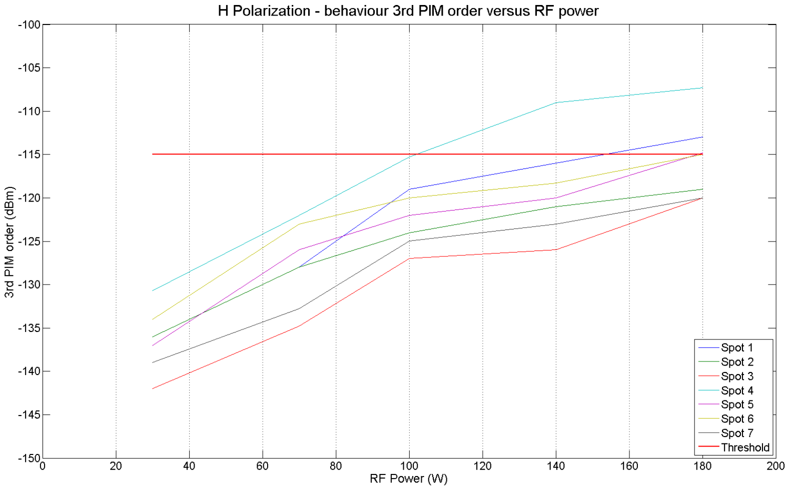

(b) Vertical polarization

Figure 5.19: PIM in terms of RF carrier power for some particular spots.

5.3.2 Ku-band test set-up on Multi Layer Insulation

The same set-up considered in Section 5.3.1 was also employed to evaluate the 3$^{\text{rd}}$ order PIM performance of a set of multi layer insulation (MLI) samples. The MLIs are the typical gold-colored multi-layer blankets used to protect satellite external surfaces from thermal radiation in space. The MLI samples for test mounted rivets composed of springs and standoff, in order to check the best material/combination in terms of PIM for the springs over an aluminium standoff. All the rivets but one were covered by Vespel (a low PIM absorber), whereas the remaining one was illuminated by the antenna within its maximum-gain region.

Following the architecture schematic of Fig. 3.9 described in Section 3.3, the MLI samples were placed 1.2 m away from the horn antenna connected at the common port of the Ku-band triplexer described in Section 5.2.2.

Firstly, the residual PIM floor of the assembled set-up was checked with a blank scenario composed of only the anechoic chamber walls. Next, the sensitiveness of the test bed was verified by inserting a metallic sponge in the position of the DUT in the anechoic chamber (in front of the antenna). Then, the PIM of the different MLI samples were measured. Furthermore, in some tests the illuminated rivet was also covered by a washer manufactured in Vespel, in order to measure the PIM level of the MLI without rivets. A total of 127 tests were performed, both at ambient temperature and over thermal cycles. Figure 5.20 illustrates the test campaign carried out with some photos of the set-up and the MLI samples.

The main results are summarized in Table 5.13. The rivet area was observed prone to ignite PIM, especially when the combination of aluminium springs and aluminium standoff was employed. Lower PIM was observed with titanium and Kapton springs over aluminium standoff. These mitigated PIM levels were equivalent to the case when the rivet area is entirely covered with pieces of Vespel, a low PIM absorber material.

	Tx 1	**Tx 2**	**3$^{\text{rd}}$ order PIM**
Frequency (GHz)	11.468	12.735	14.002
RF levels (dBm)	52	52	≤ -145 blank scenario
	40	40	≤ -88 MLI with aluminium spring
	50	50	$\leq$ -135 MLI with titanium spring
	50	50	≤ -135 MLI with kapton spring
	50	50	≤ -135 with MLI having the rivet covered with absorber

Table 5.13: Radiated PIM at Ku-band for MLI, test results.

An additional PIM test was conducted in a sample of MLI without rivets which was firstly tested as received (i.e., MLI surface perfectly plane) and after being wrinkled. The MLI was placed 1 meter away from the horn antenna and in front of

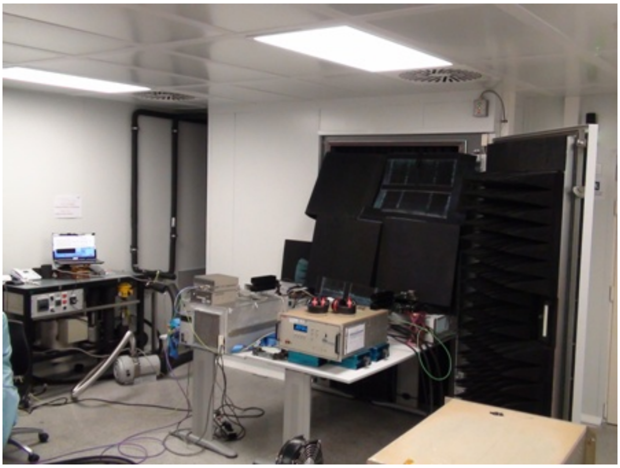

(a) Test bed - general view.

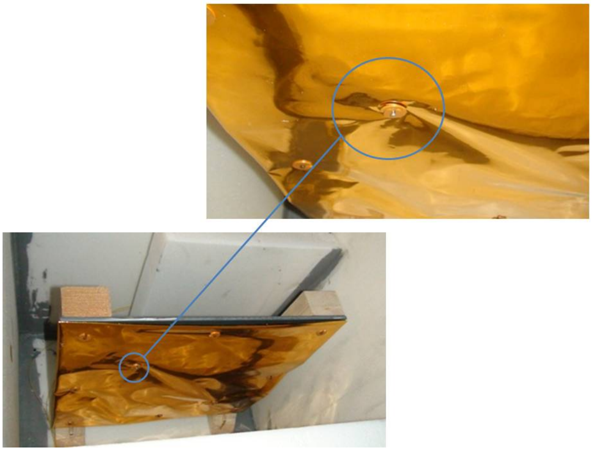

(b) Multi-Layer insulation as DUT. A rivet area is spotted.

Figure 5.20: Ku-band setup assembled for testing MLIs.

it, and was illuminated with two continuous wave (CW) carriers delivering 30 W each. The 3^{rd} order PIM was measured using the same test bench. After wrinkling the MLI, the measured PIM level was between 7 dB and 10 dB lower than for the perfectly plane MLI surface (before being wrinkled).

A study of this unexpected behavior was carried out. The PIM originated by the MLI is related to the surface currents of the radiating carriers incident to

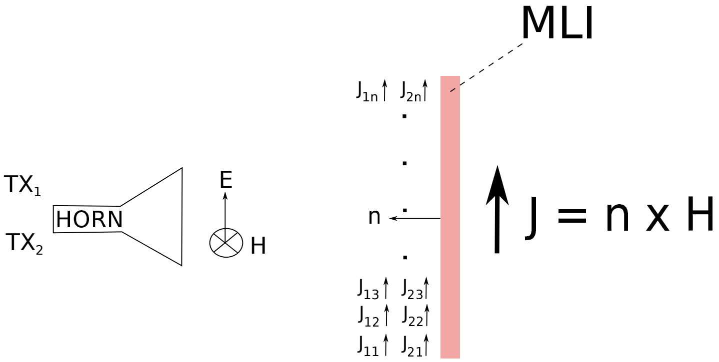

Figure 5.21: Surface currents of the transmission carriers in a plane MLI surface.

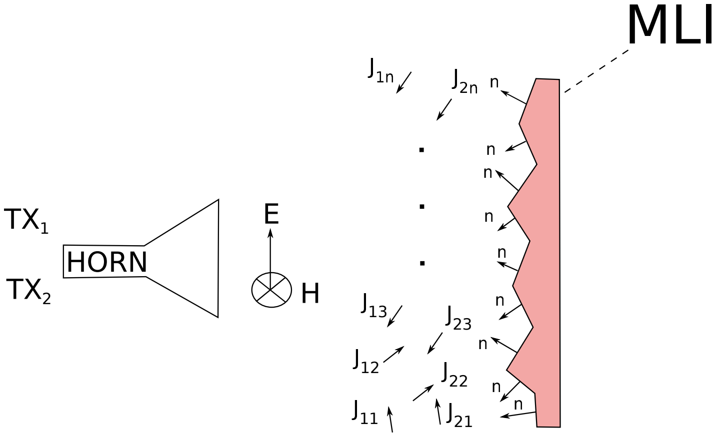

Figure 5.22: Surface currents of the transmission carriers in a wrinkled MLI.

the MLI ($\mathbf{J} = \hat{\mathbf{n}} \times \mathbf{H}$). These currents interact in a non-linear way in the MLI, leading to a current $\mathbf{J}_{\mathrm{PIM}}$ which generates the radiated PIM picked-up by the horn antenna of the set-up. Since all the elemental currents distributed along the MLI surface carriers are essentially in phase for each carrier (see Fig. 5.21), the resulting radiated fields generated by the PIM current $\mathbf{J}_{\mathrm{PIM}}$ will be also in phase, thus maximizing the PIM power radiated towards the horn antenna.

Conversely, the surface currents for a wrinkled MLI surface will be oriented randomly (see Fig. 5.22), so that the PIM current distribution $\mathbf{J}_{\mathrm{PIM}}$ will not be in phase anymore, reducing the radiated PIM power (particularly, in the direction of the horn antenna). This property may be of interest to reduce the level of PIM radiated by an MLI surface, particularly in the worst direction.

5.3.3 Ku-band test set-up for reflector mesh samples

In the frame of the ESA ARTES (Advanced Research in Telecommunications Systems) activity "Mesh and associated carrying net for large deployable reflector antenna" (MESNET project), HPS-Germany developed several reflective mesh samples which were tested for PIM at ESA-VSC European High Power RF Space Laboratory.

In order to give the right mechanical tension to the mesh samples, a non-metallic frame was also made available by HPS-Germany.

The test campaign was focused in the third order PIM, as it is normally the one with highest power levels. The test scenario was the same used at Ku-band for PIM tests in ESA Small Geo Payload, see Table 5.14, being also fully representative for telecommunication payloads. The PIM requirements for the samples are also detailed in Table 5.14.

Most of the PIM tests were performed at ambient temperature. Only a temperature cycle PIM test in the range −30/+80 °C was conducted for a mesh sample inserted into an RF-transparent thermal chamber, as depicted in Fig. 5.23. Figure 5.24 shows pictures of the set-up employed for measuring the PIM for a DUT placed in front of the test bench.

	Tx 1	**Tx 2**	**3^{rd} order PIM**	**Distance horn-DUT**
Frequency (GHz)	11.468	12.735	14.002	
RF levels (dBm)	50	50	≤ -135 blank scenario	1.2 m
	50	50	≤ -110 mesh samples	1.2 m

Table 5.14: Radiated PIM at Ku-band, test scenario and PIM requirements for the mesh samples.

A total of 10 different meshes were tested. Some of the meshes presented sawing areas disposed either in horizontal or vertical direction. The PIM tests were conducted having the horn antenna of the set-up in the vertical polarization (V-Pol). The distance between the antenna and the DUT was 1.2 m, the isotropic gain of the horn were 20 dBi and two CW carriers of 100 W each were used. From (3.3), the power flux density ($PFD_{\text{Tx-T}}$) at the mesh samples has been estimated to be about 1100 W/m^2.

The tests clearly revealed that the mesh borders were a strong PIM source, due to the finishes between the mesh sample and the frame (i.e, bad contact wires, presence of tape, tension mechanisms, etc.). A mesh sample with sawing areas is shown in Fig. 5.24(c). The sawing areas degrade the PIM in about 15 to 20 dB when compared with the samples without sawing areas. Moreover, the PIM level detected from these samples were unstable over time. PIM degradation was

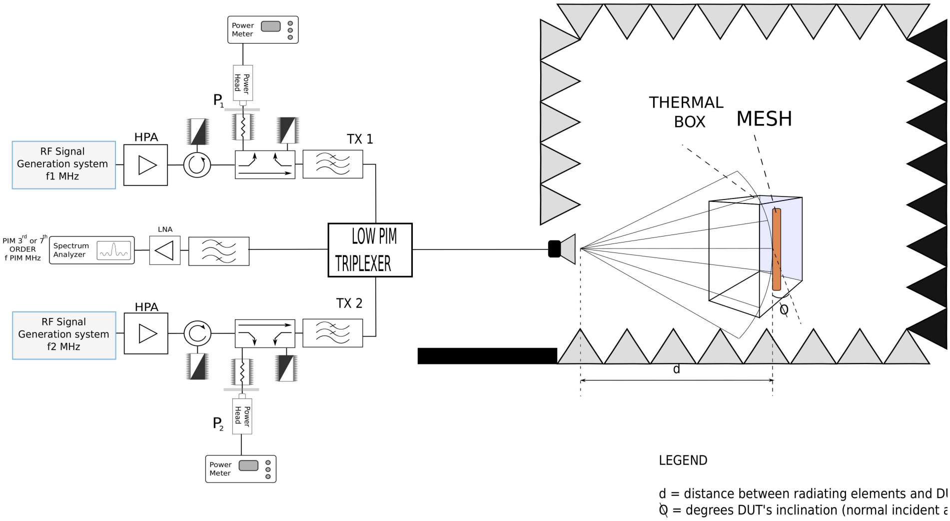

Figure 5.23: Schematic of the Ku-band radiated PIM test bed employed for thermal cycle tests.

increased after adding mechanical tension to the orthogonal direction with respect to the sawing.

In order to get rid of unwanted additional PIM contributions generated by the frame rather than from the mesh itself, the border areas were masked as shown in Fig. 5.24(d). The masking was carried out with a low PIM absorber, so that only the center of the mesh was exposed to the RF carriers. The dimensions of the square area exposed to the RF signal were 10 cm x 10 cm, being placed within the region of maximum gain of the WR75 horn antenna (see Figures 3.12 and 3.13).

A first set of measurements was performed on each mesh at ambient temperature, applying different mechanical tensions. The general trend is that mesh samples without sawing areas showed a lower PIM contribution, in the range between −120 and −130 dBm depending on the particular mesh sample. In addition, the PIM is reduced and stabilized as the mechanical tension increases. This is probably thanks to the stiffer structure which creates a more stable metal-to-metal contact. Benefits on PIM were also observed repeating the test after leaving the sample with applied mechanical tension during several hours. However, an excessive tightening of the structure may cause a PIM degradation.

Finally, a thermal cycle PIM test was conducted on one of the samples which showed better PIM performance at ambient temperature. The results indicated that the mesh suffered a PIM degradation of up to 40 dB and, in general, an unstable PIM response is observed. This unexpected bahaviour is attributed to a

(a) Test bed outside the anechoic chamber

(b) Test bed inside the anechoic chamber

(c) One of the DUTs: mesh sample with sawing

(d) PIM test focused at one restricted area of the DUT

Figure 5.24: Images of the test bed used for measuring the radiated PIM from the mesh samples.

combination between the intrinsic nature of the mesh and the limitations of the test set-up. Indeed, in order to emulate a thermal cycle at ambient pressure, the sample was inserted into an RF transparent thermal box and exposed to a flux of a mixture of air and nitrogen. The flux has probably caused vibrations in the mesh with consequent generation of unstable metal-to-metal contacts. Additional PIM contribution could be associated to the frame, which has a different thermal dilatation coefficient than the mesh, which may have caused a variation in the mechanical tension applied to the mesh sample.

During the test campaign, one sample showing a PIM level of -130 dBm having an exposed area A_1 of 10 cm x 10 cm, was also tested with an increased exposed area A_2 of 20 cm x 20 cm (see Fig 5.25). The same mechanical tension was applied. The PIM level of this second test was -124 dBm, thus justifying Eq. (3.7) derived in Section 3.3.1. In fact, we have that $A_2 = 4A_1$, thus $10\log\left(A_2/A_1\right) = 6$ dB, which coincides with the increase in the measured PIM level.

The outcomes of this set of radiated PIM measurements were published in [38].

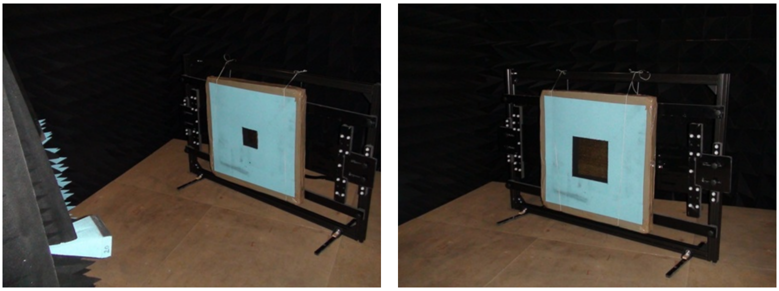
(a) Target area (10 cm x 10 cm) (b) Target area (20 cm x 20 cm)

Figure 5.25: Mesh sample with two different exposed areas.

5.3.4 K/Ka-band test set-up for reflector mesh samples

A similar test to the one carried out in Section 5.3.3 has been performed in K/Ka-band for reflector mesh samples from a different manufacturer. The measurement set-up presented in Section 5.2.3 was employed for evaluating radiated PIM in pre-tensioned mesh samples. The test scenario is detailed in Table 5.15. A test bed schematic is depicted in Fig. 5.26. From a practical point of view, the 7th order PIM is normally the limiting one in the new generation of K/Ka-band satellites, whose uplink band ranges between 27 and 31 GHz [6,49]. In addition, the 3rd order PIM was also measured as worst case, since it is the one with higher amplitude although appears at a different frequency range. The K-band set-up is able to measure by its own the 3rd order PIM contribution provided that it falls in the frequency range between 22.7 and 24.1 GHz, but it must be backed-up by an additional antenna in order to collect and measure the 7th order PIM at the Ka-band reception channel.

Some pictures of the test bed are provided in Fig. 5.27. A radar absorbent material (RAM) covers the low PIM multiplexer, in order to protect the reception (PIM) channel from the back-scattering of the transmission carriers (the meshes are reflective), which could ignite Active Inter-Modulation (AIM) at the low noise amplifier (LNA).

With the insertion of the self-designed low PIM transitions (see Fig. 5.12), the set-up showed an outstanding residual 3rd order PIM above 192 dBc with 50 W CW/carrier (see Table 5.16). For the 7th order PIM, the residual PIM level was

	Tx 1	**Tx 2**	**3rd order PIM**	**7th order PIM**
Frequency (GHz)	17.96	20.5	23.04	28.012

Table 5.15: Radiated PIM at K-band, test scenario.

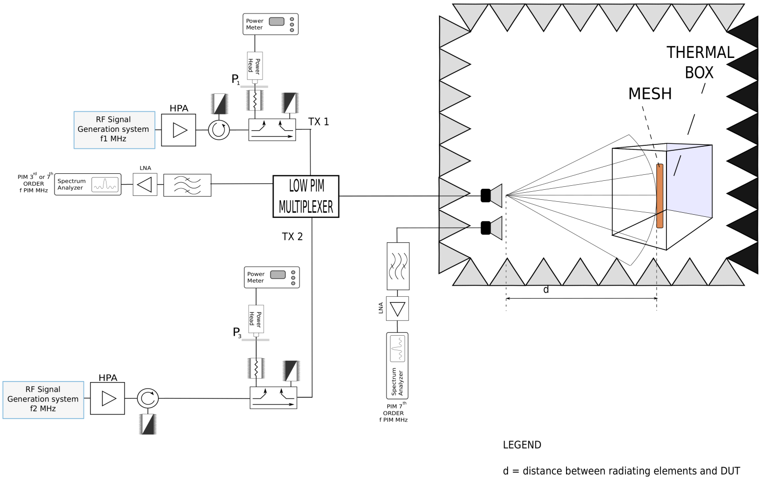

Figure 5.26: Schematic of the test bed for radiated PIM at K/Ka-band.

	Tx 1	**Tx 2**	**3rd ord. PIM**	**7th ord. PIM**	**T (°C)**
Freq. (GHz)	17.96	20.5	23.04	28.012	
RF levels (dBm)	47	47	≤ -145 blank	≤ -160 blank	+22
	47	47	≤ -94 DUT	≤ -135 DUT	+22
	47	47	≤ -77 DUT	≤ -117 DUT	+80/−30

Table 5.16: Radiated PIM at K/Ka-band for reflector meshes, test results.

below −160 dBm (namely, 207 dBc). The verification of the test set-up using a metallic sponge as DUT demonstrated the sensitivity of the measurement system, since a 3rd order PIM of −67 dBm and a 7th order PIM of −110 dBm were observed with only 5 W per CW carrier.

An exhaustive test campaign was performed. Several mesh samples placed at 0.7 m from the horn were tested, each exposed to a different mechanical tension. The sample having a higher mechanical tension showed lower PIM, of around −94 dBm for the 3rd order PIM and −130 dBm for the 7th order PIM. The same sample was also tested under thermal cycle between +80 and −30 °C, showing a 17 dB degradation for both PIM orders when compared with the tests carried out at ambient temperature. The main results are reported in Table 5.16. These experimental results clearly show the relevant differences between PIM terms corresponding to different orders, being the 3rd order PIM contribution the critical one in terms of amplitude level.

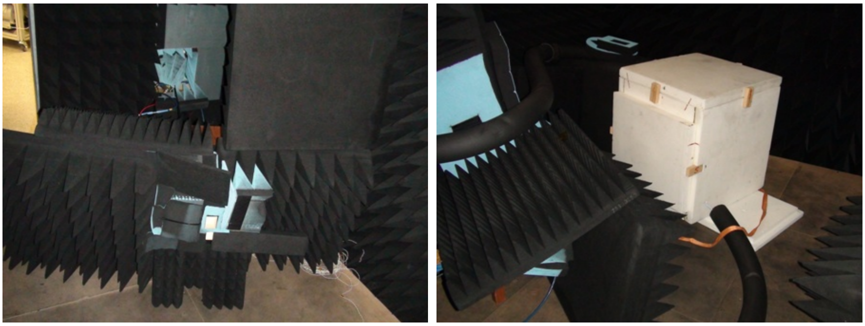

(a) Part inside the anechoic chamber - horn antennas. The multiplexer is covered by RAM absorbers.

(b) Part inside the anechoic chamber - RF transparent box to accommodate the DUT during the thermal cycle tests.

(c) Part outside the anechoic chamber.

Figure 5.27: Test set-up assembled for testing radiated PIM at K/Ka-band.

5.3.5 L-band test set-up for ATV

The final experimental test campaign reported in this chapter is related to the PIM evaluation for an on-board anomaly observed in the International Space Station (ISS).

In 2012, the Automatic Transfer Vehicle ATV-003 (also named Edoardo Amaldi, in honor of the Italian nuclear physicist) suffered an interference during its docking to the ISS. Given the isolated scenario in terms of RF signals and the particular frequency tones involved, an investigation carried out by ESA identified the source of the interference. It was a third order inter-modulation contribution between the strong TDRS (Tracking and Data Relay System) signal transmitted during the docking procedure and the very weak ISS Wi-Fi signal.

But what could have ignited PIM? The suspicious fell on the ATV's external

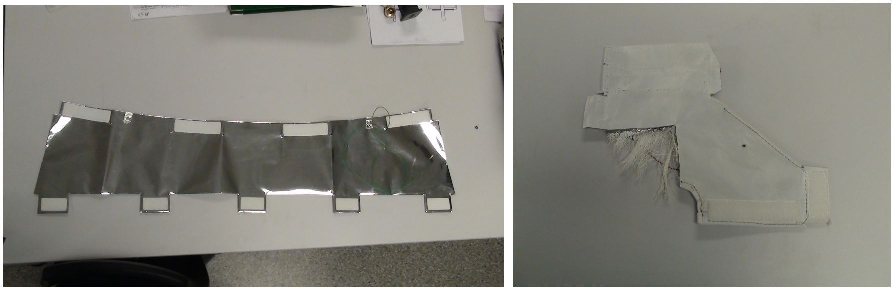

(a) MLI ATV test sample (b) MLI ATV scrap sample

Figure 5.28: Test campaign on ATV - Devices under test.

thermal blanket, the only part of the payload illuminated by both the TDRS and the ISS Wi-Fi signals (the latter through an ISS window). The ESA-VSC European High Power RF Space Laboratory was given the task of confirming the suspicious on the MLI thermal blanket, localizing the particular PIM sources, and providing recommendations to mitigate the disturbances for the upcoming ATV-4 (also named Albert Einstein, in honor of the German physicist winner of a Nobel Prize). A couple of samples of ATV-3 thermal blankets were submitted to ESA-VSC (unused retails obtained after the payload integration, see Fig. 5.28).

For these purposes a radiated PIM test bench at S-band reproducing the ATV docking scenario was assembled. The schematic is provided in Fig. 5.29. Since an integrated solution was not available for this band, a traditional radiated set-up was implemented (see Fig. 5.30).

The test scenario is detailed in Table 5.17, which reproduces the power flux density at the ATV during the docking with the ISS. In particular, the 90 W CW signal at 2.2875 GHz models the TDRS signal, whereas the 0.5 W CW tone at 2.4686 GHz reproduces the ISS Wi-Fi signal. For each test, a dedicated area of the sample was illuminated by the RF carriers, being the remaining sample part masked by a PIM-free absorber (see Fig 5.31). In this way, it was possible to analyze several spots of the DUT, such as rivets, grounding wires, sawing areas, etc.

A test campaign was executed. The summarized results are reported in Fig. 5.32.

	Tx 1	**Tx 2**	**3^{rd} order PIM**	**Distance**
Frequency (GHz)	2.2875	2.4686	2.1064	0.5 m
RF levels (W CW)	90	0.5		

Table 5.17: Radiated PIM at S-band, test results.

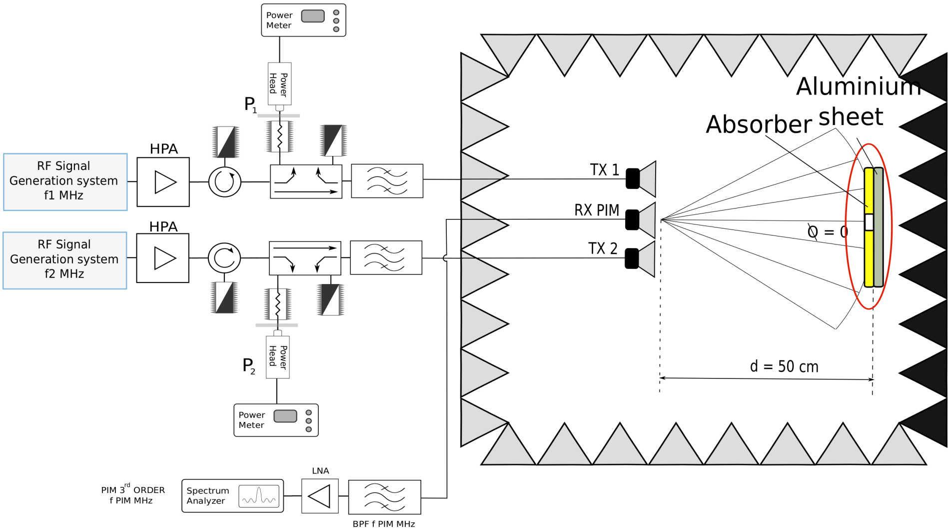

Figure 5.29: Schematic of the S-band radiated PIM set-up assembled for testing the ATV-3 thermal blanket.

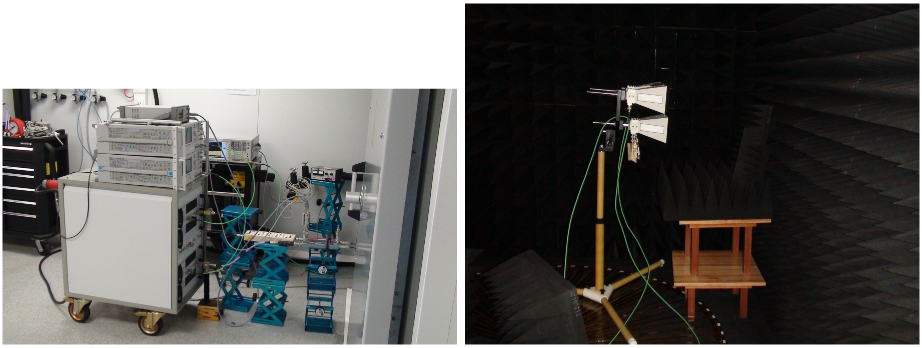

(a) Outside anechoic chamber (b) MLI ATV scrap sample

Figure 5.30: S-band radiated PIM set-up assembled for testing the ATV-3 thermal blanket samples.

Both MLI samples under test (DUT 1 and DUT 2) generated a relevant PIM interference. This was unexpected, since the carrier power levels were very different (i.e., the Wi-Fi signal is 22.5 dB lower than the TDRS signal), which normally causes a strong reduction in the amplitude of the PIM terms [17]. For such a reason, PIM measurement standards specify that both carriers should have the

(a) rivet (b) Sawing

Figure 5.31: Test campaign on ATV - restricted areas of the DUT.

same power [46].

Rivets, grounding wires and any other metal-to-metal junctions were also observed to generate unacceptable levels of PIM. In addition, the scrap white sample (ATV representative sample) does generate high levels of PIM when the illuminated area includes micro-particles of metal, which is the usual case for this sample. The source of these metallic micro-particles is the coating at the back side of the white MLI upper layer. These unwanted particles could migrate to the white side during the deposition process, manufacturing, storage or assembling in the ATV. A large concentration of these particles was observed at the gloves by simply touching this side of the MLI with the finger.

After testing, a further investigation was conducted with a HMOM (High Magnification Optical Microscope) equipment on both samples. Several micro-scratches were observed in sample 1, probably caused by the manufacturing process (see Fig. 5.33(a)). Sample 2 showed the deposition of several metallic particles, which are probably responsible of the PIM ignition mechanism (see Fig. 5.33(b)).

It is important to notice that even when the defective MLI is considered a high source of PIM, this does not imply to be the only one in the vicinity of the TDRS antenna.

As a recommendation, and in order to mitigate the PIM issue for the forthcoming ATVs, it was suggested to ESA to:

- Clean the MLI area around the TDRS antenna with a nitrogen gun, and perform visual inspection to ensure clean and dust-free surfaces.
- Use masking techniques to cover potential PIM sources in the vicinity of the TDRS antenna, such as rivets.

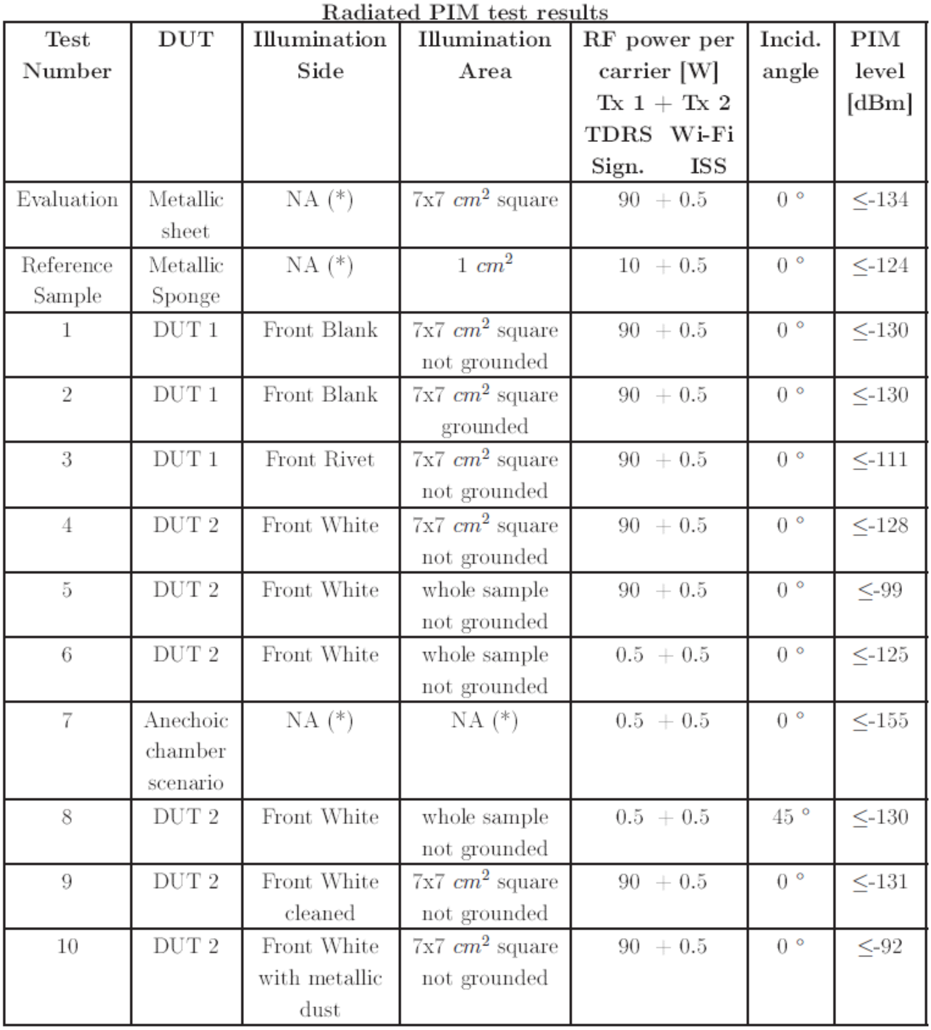

Radiated PIM test results

Test Number	DUT	Illumination Side	Illumination Area	RF power per carrier [W] Tx 1 + Tx 2 TDRS Sign. Wi-Fi ISS	Incid. angle	PIM level [dBm]
Evaluation	Metallic sheet	NA (*)	7x7 cm^2 square	90 + 0.5	0 °	≤-134
Reference Sample	Metallic Sponge	NA (*)	1 cm^2	10 + 0.5	0 °	≤-124
1	DUT 1	Front Blank	7x7 cm^2 square not grounded	90 + 0.5	0 °	≤-130
2	DUT 1	Front Blank	7x7 cm^2 square grounded	90 + 0.5	0 °	≤-130
3	DUT 1	Front Rivet	7x7 cm^2 square not grounded	90 + 0.5	0 °	≤-111
4	DUT 2	Front White	7x7 cm^2 square not grounded	90 + 0.5	0 °	≤-128
5	DUT 2	Front White	whole sample not grounded	90 + 0.5	0 °	≤-99
6	DUT 2	Front White	whole sample not grounded	0.5 + 0.5	0 °	≤-125
7	Anechoic chamber scenario	NA (*)	NA (*)	0.5 + 0.5	0 °	≤-155
8	DUT 2	Front White	whole sample not grounded	0.5 + 0.5	45 °	≤-130
9	DUT 2	Front White cleaned	7x7 cm^2 square not grounded	90 + 0.5	0 °	≤-131
10	DUT 2	Front White with metallic dust	7x7 cm^2 square not grounded	90 + 0.5	0 °	≤-92

Figure 5.32: Test campaign on ATV - summary of results.

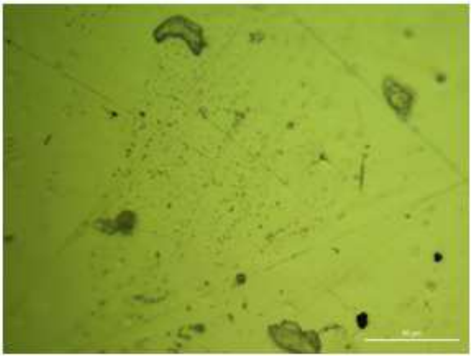

(a) Sample 1 - scratches.

(b) Sample 2 - particle deposition.

Figure 5.33: Test campaign on ATV - details of the ATV-3 samples.

Chapter 6

Conclusions and future work

The work developed in this Ph.D. thesis work is aimed at addressing the passive inter-modulation issue in satellite hardware from both theoretical and experimental points of view.

As far as theoretical concerns (see Chapter 2), the heuristic model able to explain the 3^{rd} order PIM behaviour when non-contributing carriers are added to the scenario represents a step forward in PIM modeling. This model introduces a behavioural assumption, so far never considered in technical literature: the amount of PIM power associated to each order is kept if the amount of power at the input of the non-linear system is constant. The proposed model does not belie the classical polynomial model for PIM, but integrates it with the energy conservation law in order to provide a good agreement with reported experimental data. Furthermore, the novel model introduces the presence of a slope factor parameter derived from the real dependence of the PIM power to the input carriers power. The latter could be refined following the works of Sombrin and Henrie [51,52].

In addition, the baseline of this novel polynomial model could be also extended to higher PIM orders. This can be of interest because, despite the 3^{rd} order PIM is the most critical one in practice and it is largely evaluated at C- and Ku-bands, K/Ka-band payloads tend to suffer from high order inter-modulation orders, such as the 5^{th} and the 7^{th}, due to the higher separation between the uplink and downlink frequency bands. Given that for a generic case with N-carrier signals the number of PIM terms generated grows exponentially and several classes of PIM contributions are ignited, a more complex scenario is expected. The mathematics for the fifth order have been partly developed, but they were not included because a further investigation is needed.

Another contribution of this work is related to the effect of carrier phase in PIM for a generic multicarrier scenario. The theoretical study and the software developed showed that the PIM level at a certain frequency can vary if more than one PIM contribution is present at such a frequency, and this variation depends from the relative phases of the carriers. For the first time, laboratory measurements able to experimentally check this effect were carried out, as described in Chapter 2. These already unpublished results will be submitted in the coming future to a scientific journal. As a future research line, the software developed could be enhanced and a graphic user interface (GUI) can be incorporated to facilitate its use. In addition, the same software may be employed to extract the PIM amplitude factors for a generic N-order and M-carriers scenario starting from the results obtained for an N-order and 2-carriers standard case.

Another key point for future theoretical investigations on PIM is related to modulated signal scenarios. A preliminary study (not included in this work) has been carried out with a simplified two-carriers case, and the first results suggest that the conservation energy law for PIM is still valid. In particular, if the carriers are modulated, the energy associated to the PIM terms is distributed along the spectrum. Nevertheless, some theoretical work, supported by real laboratory tests, is deemed necessary before publishing this novel work.

From an experimental point of view, this Ph.D. thesis work proposes novel PIM test bed architectures (see Chapter 3). These integrated architectures consent the minimization of flange connections in the main RF branch (i.e. where the carriers are mixed), which is the part of the set-up prone to ignite PIM. The rejection obtained with the HFRW and MHFRW filter topologies introduced in Chapter 4 for the transmission channels is outstanding, given their capability for implementing a high number of transmission zeros in the PIM reception band. Several test beds have been developed for a wide range of frequency bands, from C- to K/Ka-band. These test beds, flexible and compact, represent the state-of-art for conducted waveguide PIM set-ups, since they consent the evaluation of different PIM orders with very low residual PIM level (above 185 dBc in all cases), both in forward and backward scenarios. In addition, the proposed architectures have the benefits of absence of return loss degradation, minimization of the insertion losses of the test set-up (reducing thermal issues and so increasing the RF power level available at the DUT input), as well as the avoidance of unwanted resonances related to element interconnections.

As a further degree of flexibility, the same proposed architectures can be easily adapted to radiated PIM test beds placed inside an anechoic chamber, bringing additional advantages. In particular, these architectures permit the use, in most of the cases, of a single antenna for both transmission and reception. The latter avoids the cross-coupling issues between antennas, which is typical of classical radiated PIM test beds, and allows using the same spot for transmission and reception, with consequent minimization of the measurement error.

The PIM measurement test beds developed according to the novel test bed architectures introduced in Chapter 3 have been largely used in real test campaigns, as shown in the experimental examples reported in Chapter 5. These architectures provides outstanding residual PIM levels of the test facilities, which are $20 - 40$ dB lower than typical PIM specifications in the space sector, both for conducted (backward and forward) and radiated scenarios. In addition, the last subsection of Chapter 5 was dedicated to the PIM investigation of one on-board anomaly observed during the docking of the ATV-003 with the ISS. Such a PIM investigation, conducted at S-band, consented to mitigate the PIM generation for the forthcoming ATV-004.

The development of PIM measurement set-ups according to these new architectures at lower frequency bands (for S- or L-band) is a matter of future research. For instance, for implementing L-band PIM tests beds for Global Navigation Satellite Systems (GNSS). For such applications, the rectangular waveguides should be replaced by coaxial technology to keep reasonable dimensions for the hardware. However, coaxial connectors are prone to generate PIM, and novel solutions might be investigated. In addition, a high rejection should be provided without using HFRW and MHFRW filter solutions. Nevertheless, the guidelines of an essential architecture will be kept, in order to minimize the number of potential PIM sources and maintain the benefits detailed above.

The procedure to implement quiet (low PIM) loads in waveguide technology proposed in Section 3.2.2.1 is also a novel contribution, being of practical interest for PIM measurements under conducted PIM scenarios. High-performance backward PIM measurement set-ups are normally limited by the PIM performance of the quiet load, which is successfully blocked by the new proposed approach. As a result, the design of a low PIM load is reduced to the use of a standard waveguide load (dimensioned to the amount of RF power delivered by the transmission carriers) plus a filter suited to let pass the carriers and reject the PIM. Anyway, utmost care should be dedicated to the design of the filter (avoidance of tuning elements, clam-shell assembly, high pressure flanges), in order to minimize any unwanted additional PIM contribution.

As far as radiated PIM concerns, the novel and simple theory proposed in Section 3.3.1 is another outcome of this research work. Using the Friis transmission formula, this theory is able to link the RF power level registered at the power heads/spectrum analyzer of the test bed to the power flux density at the target. After obtaining a full characterization of the transmission/reception antenna pattern, the target can be tailored to be exposed to the RF power in the maximum gain region of the antenna, thus having accurate evaluation of the power flux densities corresponding to both the transmission carriers and the PIM contribution.

For future research in radiated PIM scenarios, an interesting topic is the optimization of PIM behaviour of MLI structures. In particular, a new theory may be developed to explain the difference in PIM levels observed in real laboratory tests between a plane and a wrinkled MLI surface, and take profit of this property to reduce the PIM generated by MLI thermal blankets.

Last but not least, the capability of carrying out radiated PIM tests under thermal cycles is an area of future research. The development of a new thermal system able to minimize the mechanical vibrations generated by the air convection is required. The latter is not trivial, since the PIM radiated scenario only consents heat transfer by convection, which implies that a mixture of nitrogen/air should flow to the DUT. Thus, solutions able to minimize simultaneously the air flow and the thermal losses must be investigated.

From the different results obtained during this Ph.D. thesis work, it can be stated that the main objectives proposed at Section 1.4 have been essentially fulfilled. However, some new and exciting research topics have been identified for future investigation on PIM issues for satellite hardware.

Appendix A

Publications

This appendix provides the list of all the publications carried out in the frame of this Ph.D. Thesis work. All the publications are directly linked to the contents exposed in the previous chapters. The list includes a total of 14 publications: 3 papers published in high-ranked peer-reviewed international journals, 5 communications accepted in peer-reviewed IEEE international conferences, 3 communications accepted in international workshops, 1 invited paper at a national conference, and 2 participations (as invited speaker) in workshops of the 48th European Microwave Conference held in Madrid, Spain.

A.1 Publications in international journals

- **D. Smacchia**, P. Soto, V. E. Boria and D. Raboso, “A new model to determine passive intermodulation terms when non-contributing carriers are added to classical scenarios,” *IEEE Access*, vol. 9, pp. 152070–152074, Nov. 2021, DOI: 10.1109/ACCESS.2021.3126903.

- **D. Smacchia**, P. Soto, M. Guglielmi, J. V. Morro, V. E. Boria and D. Raboso, “Implementation of waveguide terminations with low-passive intermodulation for conducted test beds in backward configuration,” *IEEE Microwave and Wireless Components Letters*, vol. 29, no. 10, pp. 659–661, Oct. 2019, DOI: 10.1109/LMWC.2019.2933600.

- **D. Smacchia**, P. Soto, V. E. Boria, M. Guglielmi, C. Carceller, J. Ruiz-Garnica, J. Galdeano, and D. Raboso, “Advanced compact setups for passive intermodulation measurements of satellite hardware,” *IEEE Transactions on Microwave Theory and Techniques*, vol. 66, no. 2, pp. 700–710, Feb. 2018, DOI: 10.1109/TMTT.2017.2783383.

A.2 Participation in conferences and workshops

- M. Lori, T. Sinn, E. K. Pfeiffer, **D. Smacchia** and J. C. Angevain, “Mesh based reflector surfaces,” *13th European Conference on Antennas and Propagation (EuCAP)*, Krakow, Poland, 31st March - 5th April 2019, 5 pp.

- P. Soto, **D. Smacchia**, J. Ruiz-Garnica, M. Guglielmi, C. Carceller, and V. E. Boria, “High power filters and multiplexers for PIM setups,” presented at the Workshop WM-03 (Recent Advances in RF/microwave Filters for Space Application) in *48th European Microwave Conference (EuMC)*, Madrid, Spain, 23rd - 28th September 2018.

- **D. Smacchia** and P. Soto, “Passive intermodulation measurement and extension to multicarrier scenarios,” presented at the Workshop WM-02 (High Power RF Breakdown and PIM in Space Applications) in *48th European Microwave Conference (EuMC)*, Madrid, Spain, 23rd - 28th September 2018.

- **D. Smacchia**, C. Carceller, M. Guglielmi, P. Soto, V.E. Boria, J. Ruiz-Garnica, and P. González, “A wideband diplexer for Ka-band passive intermodulation measurement,” in *2018 IEEE MTT-S International Microwave Symposium Digest (IMS)*, Philadelphia, PA, 10th - 15th June 2018, pp. 1106–1109, DOI: 10.1109/MWSYM.2018.8439191.

- P. Soto, C. Carceller, J. Ruiz-Garnica, S. Cogollos, V. E. Boria, M. Guglielmi and **D. Smacchia**, “Design of advanced waveguide filters for passive intermodulation measurement setups,” in *2017 IEEE MTT-S Internacional Conference on Numerical Electromagnetic and Multiphysics Modeling and Optimization for RF, Microwave and Terahertz Applications (NEMO)*, Sevilla, Spain, 17th - 19th May 2017, pp. 335–337, DOI: 10.1109/NEMO.2017.7964278.

- **D. Smacchia**, P. Soto, V. E. Boria, D. Raboso and M. Guglielmi, “Comparison of third order passive inter-modulation products in two and three high power RF carriers scenarios,” *9th International Workshop on Multipactor, Corona and Passive Intermodulation (MULCOPIM)*, Noordwijk, The Netherlands, 5th - 7th April 2017, 8 pp.

- P. Soto, **D. Smacchia**, C. Carceller, V. E. Boria and M. Guglielmi, “Computer-aided design (CAD) of filters and multiplexers for passive inter-modulation (PIM) set-ups,” in *2016 IEEE MTT-S Latin America Microwave Conference (LAMC)*, Puerto Vallarta, Mexico, 12th - 14th December 2016, 3 pp., DOI: 10.1109/LAMC.2016.7851247.

- V. E. Boria, L. Nuño, O. Monerris, **D. Smacchia**, D. Argiles and D. Raboso, “Experimental measurements and diagnosis of radio-frequency space high power and electromagnetic compatibility effects,” *2016 ESA Workshop on*

Aerospace EMC (Aerospace EMC), Valencia, Spain, 23rd - 25th May 2016, 6 pp., DOI: 10.1109/AeroEMC.2016.7504600.

- P. Soto, C. Carceller, V. E. Boria, M. Guglielmi, **D. Smacchia**, J. Gil, C. P. Vicente, B. Gimeno, and D. Raboso, "CAD of multiplexers for PIM measurement set-ups," *XXX Simposium Nacional de la Unión Científica Internacional de Radio (URSI 2015)*, Pamplona, Spain, 2nd - 4th September 2015, 4 pp. (invited)

- P. Soto, V. E. Boria, C. Canceller, S. Cogollos, M. Guglielmi, and **D. Smacchia**, "Practical design of rectangular waveguide filters with a capacitive building block providing an extra transmission zero," *2015 IEEE MTT-S International Microwave Symposium (IMS)*, Phoenix, AZ, 17th - 22nd May 2015, 4 pp., DOI: 10.1109/MWSYM.2015.7167019.

- M. Gugliemi, P. Soto, C. Carceller, V. E. Boria, **D. Smacchia**, M. Brumos, S. Cogollos, B. Gimeno, and D. Raboso, "A novel Ku-band test bed for passive intermodulation measurements," *8th International Workshop on Multipactor, Corona and Passive Intermodulation (MULCOPIM)*, Valencia, Spain, 17th - 19th September 2014, 6 pp.

Bibliography

[1] J. G. Dumolin, “Passive intermodulation and its effect on space programs,” in *Proc. IEE Colloquium on Screening Effectiveness Measurements (Ref. No. 1998/452)*, London, UK, May 1998. DOI: 10.1049/ic:19980725, pp. 2/1–2/10.

[2] C. Hoeber, D. Pollard, and R. Nicholas, “Passive intermodulation product generation in high power communications satellites,” in *Proc. 11th AIAA Int. Comm. Satellite Syst. Conf.*, San Diego, CA, Mar. 1986. DOI: 10.2514/6.1986-657, pp. 361–365.

[3] H. Zhang, Y. Zhang, C. Huang, Y. Yuan, and L. Cheng, *Spacecraft Electromagnetic Compatibility Technologies.* Singapore: Springer, 2020.

[4] R. Piazza, B. Shankar, M. R. Rao, and B. Ottersen, “Data predistortion for multicarrier satellite using orthogonal memory polynomials,” in *Proc. 14th IEEE Workshop Signal Process. Adv. Wirel. Commun.*, Darmstadt, Germany, Sep. 2007. DOI: 10.1109/SPAWC.2013.6612138, pp. 689–693.

[5] R. J. Cameron, C. M. Kudsia, and R. R. Mansour, *Microwave Filters for Communication Systems: Fundamentals, Design and Applications*, 2nd ed. Hoboken, NJ: John Wiley & Sons, 2018.

[6] J. Christensen. (2012, Aug.) International Telecommunications Union (ITU) regulation for Ka-band satellite networks. [Online]. Available: https://www.itu.int/md/R12-ITURKA.BAND-C-0001/_page.print

[7] H. Fenech, S. Amos, S. Tomatis, and V. Soumpholphakdy, “High throughput satellite systems: an analytical approach,” *IEEE Trans. Aerosp. Electron. Syst.*, vol. 51, no. 1, pp. 192–202, Jan. 2015. DOI: 10.1109/TAES.2014.130450.

[8] M. Yu and A. Atia (organizers), “High power issues of microwave filter design and realization,” presented at the Workshop WMH in IEEE MTT-S Int. Microwave Symp., Honolulu, Hawaii, June 2007, pp. 1–11.

[9] M. Yu, “Power-handling capability for RF filters,” *IEEE Microw. Mag.*, vol. 8, no. 5, pp. 88–97, Oct. 2007. DOI: 10.1109/MMM.2007.904712.

[10] R. C. Chapman, J. V. Rootsey, and I. Polidi, “Hidden threat - multicarrier passive component IM generation,” in *Proc. 6th AIAA Int. Comm. Satellite Syst. Conf.*, Montreal, Canada, Apr. 1976. DOI: 10.2514/5.9781600865299.0357.0372, pp. 357–374.

[11] A. Kumar, “Passive IM products threaten high-power satcom systems,” *Microwaves & RF*, vol. 26, pp. 98–103, Dec. 1987.

[12] W. Tang and C. Kudsia, “Multipactor breakdown and passive intermodulation in microwave equipment for satellite applications,” in *Proc. IEEE Mil. Commun. Conf.*, Monterrey, CA, Oct. 1990. DOI: 10.1109/MILCOM.1990.117409, pp. 181–187.

[13] P. Lui, “Passive intermodulation interference in communication systems,” *Electron. Comm. Eng. J.*, vol. 2, no. 3, pp. 109–118, June 1990. DOI: 10.1049/ecej:19900029.

[14] J. W. Boyhan, H. F. Lenzing, and C. Koduru, “Satellite passive intermodulation: system considerations,” *IEEE Trans. Aerosp. Electron. Syst.*, vol. 32, no. 3, pp. 1058–1064, July 1996. DOI: 10.1109/7.532264.

[15] F. Carducci, “Passive intermodulations aspects on ITALSAT F2/EMS spacecraft,” in *Proc. Int. Symp. Antenna Technol. Appl. Electromagn.*, Ottawa, CA, Aug. 1994, pp. 377–380.

[16] M. Bayrak and F. A. Benson, “Intermodulation products from nonlinearities in transmission lines and connectors at microwave frequencies,” *Proc. IEE*, vol. 122, no. 4, pp. 361–367, Apr. 1975. DOI: 10.1049/piee.1975.0101.

[17] C. Vicente and H. L. Hartnagel, “Passive-intermodulation analysis between rough rectangular waveguide flanges,” *IEEE Trans. Microw. Theory Techn.*, vol. 53, no. 8, pp. 2515–2525, Aug. 2005. DOI: 10.1109/TMTT.2005.852771.

[18] C. Vicente, D. Wolk, H. L. Hartnagel, B. Gimeno, V. E. Boria, and D. Raboso, “Experimental analysis of passive intermodulation at waveguide flange bolted connections,” *IEEE Trans. Microw. Theory Techn.*, vol. 55, no. 5, pp. 1018–1028, May 2007. DOI: 10.1109/TMTT.2007.895400.

[19] V. Golikov, S. Hienonen, and P. Vainikainen, “Passive intermodulation distortion measurements in mobile communication antennas,” in *Proc. 54th IEEE Veh. Technol. Conf.*, Atlantic City, NJ, Oct. 2001. DOI: 10.1109/VTC.2001.957226. pp. 2623–2625.

[20] M. Steer, *Microwave and RF Design. Modules*, 3rd ed. Chappel Hill, NC: NC State University, 2019, vol. 4.

[21] A. P. Foord and A. D. Rawlins, “A study of passive intermodulation interference in space RF hardware,” Univ. Kent, Canterbury, UK, Tech. Rep. ESTEC Contract 111036 Final Report, May 1992.

[22] L. O. Hocker, D. R. Sokoloff, V. Daneu, A. Szoke, and A. Javan, “Frequency mixing in the infrared and far-infrared using a metal-to-metal point contact diode,” *Appl. Phys. Lett.*, vol. 12, no. 12, p. 401, Jan. 1968. DOI: 10.1063/1.1651873.

[23] J. A. Bean, B. Tiwari, G. H. Bernstein, P. Fay, and W. Porod, “Thermal infrared detection using dipole antenna-coupled metal-oxide-metal diodes,” *J. Vac. Sci. Technol. B*, vol. 27, no. 11, pp. 11–14, Jan. 2009. DOI: 10.1116/1.3039684.

[24] L. E. Dodd, S. Shenton, G. A. J., and D. Wood, “Improving metal-oxide-metal (MOM) diode performance via the optimization of the oxide layer,” *J. Electron. Mater.*, vol. 45, no. 5, pp. 1361–1366, May 2015. DOI: 10.1007/s11664-015-3624-9.

[25] G. H. Schennum and G. Rosati, “Minimizing passive intermodulation product generation in high power satellites,” in *Proc. of IEEE Aerosp. Applications Conf.*, Aspen, CO, Feb. 1996. DOI: 10.1109/AERO.1996.496060, pp. 155–164.

[26] M. Vladimirescu, R. Kwiatkowski, and K. Engel, “Tunnel conduction consequences in high frequency microcontacts; passive intermodulation effect,” in *Proc. 50th IEEE Annu. Holm Conf. Electr. Contacts and 22nd Int. Conf. Electr. Contacts*, Seattle, WA, Sep. 2004. DOI: 10.1109/HOLM.2004.1353112, pp. 152–159.

[27] J. Russer, A. Ramachandran, A. Cangellaris, and P. Russer, “Phenomenological modeling of passive intermodulation (PIM) due to electron tunneling at metallic contacts,” in *IEEE MTT-S Int. Microwave Symp. Dig.*, San Francisco, CA, June 2006. DOI: 10.1109/MWSYM.2006.249389, pp. 1192–1132.

[28] S. Zhang, X. Zhao, F. Gao, and Y. He, “Study of metal contact resistance and its statistical correlationship with passive intermodulation,” in *Proc. IEEE Annu. Holm Conf. Electr. Contacts*, Albuquerque, NM, Oct. 2018. DOI: 10.1109/HOLM.2018.8611745, pp. 1–6.

[29] J. Wilkerson, K. Gard, A. Schuchinsky, and M. Steer, “Electro-thermal theory of intermodulation distortion in lossy microwave components,” *IEEE*

Trans. Microw. Theory Techn., vol. 56, no. 12, pp. 2717–2725, Dec. 2008. DOI: 10.1109/TMTT.2008.2007084.

[30] R. Cox, "Measurements of waveguide component and joint mixing products in 6-GHz frequency diversity systems," *IEEE Trans. Commun. Tech.*, vol. 18, no. 1, pp. 33–37, Feb. 1970. DOI: 10.1109/TCOM.1970.1090317.

[31] J. A. Jargon and D. C. DeGroot, "NIST passive intermodulation measurement comparison for wireless base station equipment," in *52nd ARFTG Conf. Dig.*, Rohnet Park, CA, Dec. 1998. DOI: 10.1109/ARFTG.1998.768634, pp. 128–139.

[32] J. Z. Wilcox and P. Molmud, "Thermal heating contribution to intermodulation fields in coaxial waveguides," *IEEE Trans. Commun.*, vol. 24, no. 2, pp. 238–243, Feb. 1976. DOI: 10.1109/TCOM.1976.1093272.

[33] J. S. Petit and A. D. Rawlins, "The impact of passive intermodulation on specifying and characterising components," in *Proc. 3rd ESA Electron. Comp. Conf.*, Noordwijk, The Netherlands, Apr. 1997, pp. 45–49.

[34] J. Henrie, A. Christianson, and W. Chappell, "Engineered passive nonlinearities for broadband passive intermodulation distortion mitigation," *IEEE Microw. Wireless Compon. Lett.*, vol. 19, no. 10, pp. 614–616, Oct. 2009. DOI: 10.1109/LMWC.2009.2029733.

[35] D. M. Pozar, *Microwave Engineering*, 4th ed. Hoboken, NJ: John Wiley & Sons, 2011.

[36] G. G. Connor, "Elimination of fine tuning in high power, low-PIM diplexers for combined transmit/receive antennas," in *Proc. IEE Colloquium Microw. Filters and Multiplexers*, London, UK, Nov. 1990, pp. 4/1–4/6.

[37] P. L. Lui, A. D. Rawlins, and D. W. Watts, "Measurement of intermodulation products generated by structural components," *Electron. Lett.*, vol. 24, no. 16, pp. 1005–1007, Aug. 1988. DOI: 10.1049/el:19880684.

[38] M. Lori, T. Sinn, E. K. Pffeifer, D. Smacchia, and J. C. Argevain, "Mesh based reflector surfaces," in *Proc. 13th Eur. Conf. Antennas Propag.*, Krakow, Poland, Mar. 2019, pp. 1–5.

[39] R. M. Kalb and W. R. Bennett, "Ferromagnetic distortion of a two-frequency wave," *Bell Syst. Tech. J.*, vol. 14, no. 2, pp. 322–359, Apr. 1935. DOI: 10.1002/j.1538-7305.1935.tb00418.x.

[40] A. De Sabata and A. Ignea, "Passive intermodulation distortions induced by ferromagnetic materials at GSM frequencies," in *Proc. Int. Symp. Signals*

Circuits Syst., Iasi, Romania, July 2013. DOI: 10.1109/ISSCS.2013.6651200, pp. 1–4.

[41] J. C. Lee, “Intermodulation measurements and analysis of some conducting materials commonly used in aerospace,” in *Proc. IEEE Int. Conf. Commun.*, vol. 2, Seattle, WA, June 1980, pp. 25.6.1–25.6.6.

[42] W. D. Watson, “The measurement, detection, location and suppression of external non-linearities which affect radio systems,” in *Proc. IERE Conf. Electromagn. Compat.*, Southampton, UK, Sep. 1980, pp. 1–10.

[43] M. T. Abuelmaátti, “Prediction of passive intermodulation arising from corrosion,” *Proc. IEE Sci. Meas. Tech.*, vol. 150, no. 1, pp. 30–34, Feb. 2003. DOI: 10.1049/ip-smt:20020563.

[44] F. Arazm and F. A. Benson, “Nonlinearities in metal contacts at microwave frequencies,” *IEEE Trans. Electromagn. Compat.*, vol. 22, no. 3, pp. 142–149, Aug. 1980. DOI: 10.1109/TEMC.1980.303873.

[45] J. Sanford, “Passive intermodulation considerations in antenna design,” in *Proc. IEEE Mil. Commun. Conf.*, Ann Arbor, MI, June 1993. DOI: 10.1109/APS.1993.385516, pp. 1651–1654.

[46] *Passive RF and Microwave Devices, Intermodulation Level Measurement*, International Electrotechnical Commission (IEC) Std. IEC62 037-1 to -6, 2012–2013.

[47] M. Silicani and S. Richard, “Presentation of MDA PIM test facility capabilities and studies of PIM order amplitude relationship and PIM level variation as a function of transmit power flux density,” in *Proc. 9th Int. Workshop Multipactor, Corona and Passive Intermodulation*, Noordwijk, The Netherlands, Apr. 2017, pp. 1–9.

[48] A. Shitov, D. Zelenchuk, and A. Schuchinsky, “Carrier-power dependence of passive intermodulation products in printed lines,” in *Loughborough Antennas and Propagation Conference*, Loughborough, UK, Nov. 2009. DOI: 10.1109/LAPC.2009.5352393, pp. 177–180.

[49] J. Christensen, “ITU regulations for Ka-band satellite networks,” in *Proc. 30th AIAA Int. Comm. Satellite Syst. Conf.*, Ottawa, Canada, Sep. 2012. DOI: 10.2514/6.2012-15179, pp. 524–527.

[50] A. Shayegani, J. Salmon, and R. Singh, “Multicarrier PIM behavior and testing in communications satellites,” in *Proc. 9th Int. Workshop Multipactor, Corona and Passive Intermodulation*, Noordwijk, The Netherlands, Apr. 2017, pp. 1–11.

[51] J. Sombrin, G. Soubercaze-Pun, and I. Albert, "New models for passive non linearities generating intermodulation products with non-integer slopes," in *Proc. 7th Eur. Conf. Antennas Propag.*, Gothenburg, Sweden, Apr. 2013, pp. 25–28.

[52] J. Henrie, A. Christianson, and W. J. Chappell, "Linear-nonlinear interaction's effect on the power dependence of nonlinear distortion products," *Appl. Phys. Lett.*, vol. 94, no. 11, pp. 114 101–1–3, Mar. 2009. DOI: 10.1063/1.3098068.

[53] G. Macchiarella, G. B. Stracca, and L. Miglioli, "Experimental study of passive intermodulation in coaxial cavities for cellular base stations duplexers," in *Proc. 34th Eur. Microwave Conf.*, Amsterdam, The Netherlands, Oct. 2004, pp. 981–984.

[54] B. Rosenberger, "The measurement of intermodulation products on passive components and transmission lines," in *Proc. IEEE MTT-S Int. Top. Symp. Tech. Wireless Appl.*, Vancouver, Canada, Feb. 1999. DOI: 10.1109/MTTTWA.1999.755129, pp. 57–62.

[55] J. A. Jargon and D. C. DeGroot, "Comparison of passive intermodulation measurements for the U.S. wireless industry," National Institute of Standards and Technology, Boulder, CO, Tech. Rep. NIST Technical Note 1515, Oct. 1999.

[56] S.-J. Chou, H.-T. Chou, and L.-R. Kuo, "Potential causes of PIM problems in the LTE outdoor base station multi-band antennas," in *Proc. Int. Symp. Antennas Propag.*, Okinawa, Japan, Oct. 2016, pp. 1080–1081.

[57] S. Rao and L. Shafai, *Handbook of Reflector Antennas and Feed Systems.* Boston, MA: Artech House, 2013, vol. 3.

[58] P. Bolli, S. Selleri, and G. Pelosi, "Passive intermodulation on large reflector antennas," *IEEE Antennas Propag. Mag.*, vol. 4, no. 5, pp. 13–20, Oct. 2002. DOI: 10.1109/MAP.2002.1077773.

[59] J. Henrie, A. Christianson, and W. J. Chappell, "Prediction of passive intermodulation from coaxial connectors in microwave networks," *IEEE Trans. Microw. Theory Techn.*, vol. 56, no. 1, pp. 209–216, Jan. 2008. DOI: 10.1109/TMTT.2007.912166.

[60] P. Zhao, X. Zhang, D. Yang, and X. Hy, "Superposition effect of passive intermodulation for cable assemblies with discrete point-sources," *China Commun.*, vol. 12, no. 4, pp. 97–105, Apr. 2015. DOI: 10.1109/CC.2015.7114056.

[61] Y. Patenaude, J. Dallaire, F. Menard, and S. Richard, "Antenna PIM measurements and associated test facilities," in *IEEE AP-S Int. Symp. Dig.*, vol. 4, Boston, MA, July 2001. DOI: 10.1109/APS.2001.959541, pp. 1–4.

[62] D. S. Kozlov, A. P. Shitvov, and G. Schuchinsky, "Polynomial model for high-order and multi-carrier passive intermodulation products," in *Proc. 46th Eur. Microwave Conf.*, London, UK, Oct. 2016. DOI: 10.1109/EuMC.2016.7824422, pp. 631–634.

[63] D. Smacchia, P. Soto, V. E. Boria, and D. Raboso, "A new model to determine passive intermodulation terms when non-contributing carriers are added to classical scenarios," *IEEE Access*, vol. 9, pp. 152 070 – 152 074, Nov. 2021. DOI: 10.1109/ACCESS.2021.3126903.

[64] MATLAB. Mathworks, Natick, MA. [Online]. Available: https://www.mathworks.com/products/matlab

[65] A. V. Oppenheim and S. Ronald, *Discrete-time Signal Processing*, 3rd ed. Essex, UK: Pearson Education Limited, 2009.

[66] A. J. Christianson, J. J. Henrie, and W. J. Chappell, "Higher order intermodulation product measurement of passive components," *IEEE Trans. Microw. Theory Techn.*, vol. 56, no. 7, pp. 1729–1736, July 2008. DOI: 10.1109/TMTT.2008.925238.

[67] D. Smacchia, P. Soto, V. E. Boria, M. Guglielmi, C. Carceller, J. Ruiz, J. Galdeano, and D. Raboso, "Advanced compact setups for passive intermodulation measurements of satellite hardware," *IEEE Trans. Microw. Theory Techn.*, vol. 66, no. 2, pp. 700–710, Jan. 2018. DOI: 10.1109/TMTT.2017.2783383.

[68] D. Smacchia, P. Soto, M. Guglielmi, J. V. Morro, V. E. Boria, and D. Raboso, "Implementation of waveguide terminations with low-passive intermodulation for conducted test beds in backward configuration," *IEEE Microw. Wireless Compon. Lett.*, vol. 29, no. 10, pp. 659–661, Aug. 2019. DOI: 10.1109/LMWC.2019.2933600.

[69] D. Smacchia, "Passive intermodulation measurement and extension to multicarrier scenario," presented at the Workshop WM-02 in 48th Eur. Microwave Conf., Madrid, Spain, Sep. 2018, pp. 1–43.

[70] C. Carceller, P. Soto, V. E. Boria, M. Guglielmi, and J. Gil, "Design of compact wideband manifold-coupled multiplexers," *IEEE Trans. Microw. Theory Techn.*, vol. 63, no. 10, pp. 3398–3407, Oct. 2015. DOI: 10.1109/TMTT.2015.2460738.

[71] B. Deats and R. Hartman, “Measuring the passive-IM performance of RF cable assemblies,” *Microw. RF Eng.*, vol. 36, pp. 108–114, Mar. 1997.

[72] S. Cogollos, P. Soto, V. E. Boria, M. Guglielmi, M. Brumos, B. Gimeno, and D. Raboso, “Efficient design of waveguide manifold multiplexers based on low-order EM distributed models,” *IEEE Trans. Microw. Theory Techn.*, vol. 63, no. 8, pp. 2540–2549, Aug. 2015. DOI: 10.1109/TMTT.2015.2442990.

[73] D. Smacchia, C. Carceller, M. Guglielmi, P. Soto, V. E. Boria, J. Ruiz, and P. Gonzalez, “A wideband diplexer for Ka-band passive intermodulation measurement,” in *IEEE MTT-S Int. Microwave Symp. Dig.*, Philadeplphia, PA, June 2018. DOI: 10.1109/MWSYM.2018.8439191, pp. 1106–1109.

[74] C. A. Balanis, *Antenna Theory: Analysis and Design*, 4th ed. Hoboken, NJ: John Wiley & Sons, 2016.

[75] H. Friis, “A note on a simple transmission formula,” *Proc. IRE*, vol. 34, no. 5, pp. 254–256, May 1946. DOI: 10.1109/JRPROC.1946.234568.

[76] D. C. Hogg, “Fun with the Friis free-space transmission formula,” *IEEE Antennas Propag. Mag.*, vol. 35, no. 4, pp. 33–35, Aug 1993. DOI: 10.1109/74.229847.

[77] P. Soto, C. Carceller, V. E. Boria, M. Guglielmi, D. Smacchia, J. Gil, C. P. Vicente, B. Gimeno, and D. Raboso, “CAD of multiplexers for PIM measurement set-ups,” in *Proc. XXX Simposium Nacional de la Unión Científica Internacional de Radio*, Pamplona, Spain, Sep. 2015, pp. 1–4.

[78] P. Soto, D. Smacchia, C. Carceller, V. E. Boria, and M. Guglielmi, “Computer-aided design (CAD) of filters and multiplexers for passive inter-modulation (PIM) set-ups,” in *IEEE MTT-S Latin American Microwave Conf. Dig.*, Puerto Vallarta, Mexico, May 2016. DOI: 10.1109/LAMC.2016.7851247, pp. 1–3.

[79] P. Soto, C. Carceller, J. Ruiz, S. Cogollos, V. E. Boria, M. Guglielmi, and D. Smacchia, “Design of advanced waveguide filters for passive intermodulation measurement setups,” in *Proc. IEEE MTT-S Int. Conf. Numer. Electromagn. Multiphysics Model. Optim. RF Microw. Terahertz Appl.*, Seville, Spain, May 2017. DOI: 10.1109/NEMO.2017.7964278, pp. 335–337.

[80] M. Guglielmi, “Hybrid folded rectangular waveguide filter,” European Patent PCT/EP2013/072 406, 2013.

[81] C. Carceller, P. Soto, V. E. Boria, and M. Guglielmi, “Design of hybrid folded rectangular waveguide filters with transmission zeros below the passband,” *IEEE Trans. Microw. Theory Techn.*, vol. 64, no. 2, pp. 475–485, Feb. 2016. DOI: 10.1109/TMTT.2015.2510644.

[82] P. Soto, V. E. Boria, C. Carceller, S. Cogollos, M. Guglielmi, and D. Smacchia, “Practical design of rectangular waveguide filters with a capacitive building block providing an extra transmission zero,” in *IEEE MTT-S Int. Microwave Symp. Dig.*, Phoenix, AZ, May 2015. DOI: 10.1109/MWSYM.2015.7167019, pp. 1–4.

[83] S. B. Cohn, “Direct-coupled-resonator filters,” *Proc. IRE*, vol. 45, no. 2, pp. 187–196, Feb. 1957. DOI: 10.1109/JRPROC.1957.278389.

[84] G. L. Matthaei, L. Young, and E. M. T. Jones, *Microwave Filters, Impedance-Matching Networks, and Coupling Structures.* Norwood, MA: Artech House, 1980.

[85] D. Sánchez-Escuderos, J. Ruíz-Garnica, M. Baquero-Escudero, P. Soto, V. E. Boria, G. Tosso, P. Angeletti, and M. Guglielmi, “Evanescent-mode ridge-waveguide radiating filters for space applications,” *IEEE Trans. Antennas Propag.*, vol. 67, no. 10, pp. 6286–6297, Oct. 2019. DOI: 10.1109/TAP.2019.2920272.

[86] M. Guglielmi and G. Connor, “Industrial implementation of tuning-less microwave filters,” *Microw. Eng. Eur.*, no. 1, pp. 39–40, Jan. 1996.

[87] P. Soto, V. E. Boria, C. Carceller, C. P. Vicente, J. Gil, and B. Gimeno, “EM-based synthesis and design of bandpass waveguide filters including manufacturing effects with FEST3D,” *Int. J. RF and Microwave CAE*, vol. 22, no. 1, pp. 93–103, Jan. 2012. DOI: 10.1002/mmce.20588.

[88] R. Sorrentino and G. Bianchi, *Ingegneria delle microonde e radiofrequenze.* Milan, Italy: McGraw-Hill Companies, 2006.

[89] H. J. Riblet, “Waveguide filter having nonidentical sections resonant at same fundamental frequency and different harmonic frequencies,” U.S. Patent 3 153 208, 1964.

[90] M. Morelli, I. Hunter, R. Parry, and V. Postoyalko, “Stop-band improvement of rectangular waveguide filters using different width resonators: Selection of resonator widths,” in *IEEE MTT-S Int. Microwave Symp. Dig.*, Phoenix, AZ, May 2001. DOI: 10.1109/MWSYM.2001.967215, pp. 1623–1626.

[91] ——, “Stopband performance improvement of rectangular waveguide filters using stepped-impedance resonators,” *IEEE Trans. Microw. Theory Techn.*, vol. 50, no. 7, pp. 1657–1664, July 2002. DOI: 10.1109/TMTT.2002.800381.

[92] J. Helszajn, *Ridge Waveguides and Passive Microwave Components.* Bodmin, UK: IET, 2000.

[93] C. Carceller, P. Soto, V. E. Boria, and M. Guglielmi, "Capacitive obstacle realizing multiple transmission zeros for in-line rectangular waveguide filters," *IEEE Microw. Wireless Compon. Lett.*, vol. 26, no. 10, pp. 795–797, Oct. 2016. DOI: 10.1109/LMWC.2016.2605462.

[94] Aurora Software and Testing. FEST3D Full-wave Electromagnetic Simulation Tool. Dassault Systèmes, Vélizy-Villacoublay, France. [Online]. Available: https://www.3ds.com/products-services/simulia/products/fest3d/

[95] G. Conciauro, M. Guglielmi, and R. Sorrentino, *Advanced Modal Analysis - CAD Techniques for Waveguide Components and Filters.* Hoboken, NJ: John Wiley & Sons, 2000.

[96] J. Uher, J. Bornemann, and U. Rosenberg, *Waveguide Components for Antenna Feed Systems: Theory and CAD.* Norwood, MA: Artech House, 1993.

[97] R. Mehrotra, *Regulation of global broadband satellite communications.* Geneva, Switzerland: International Telecommunication Union, 2012.

[98] J. Wang, B. Du, Y. Wu, and Y. He, "A wideband waveguide diplexer for the extend C-band antenna systems," *Prog. Electromagn. Res. C*, vol. 69, pp. 73–82, Jan. 2016. DOI: 10.2528/PIERC16083104.

[99] F. De Paolis, R. Goulouev, J. Zheng, and M. Yu, "CAD procedure for high-performance composite corrugated filters," *IEEE Trans. Microw. Theory Techn.*, vol. 61, no. 9, pp. 3216–3224, Sep. 2013. DOI: 10.1109/TMTT.2013.2275451.

[100] F. Teberio, I. Arregui, A. Gomez-Torrent, E. Menargues, I. Arnedo, M. Chudzik, M. Zedler, F. Görtz, R. Jost, T. Lopetegi, and M. Laso, "High-power waveguide low-pass filter with all-higher-order mode suppression over a wide-band for Ka-band satellite application," *IEEE Microw. Wireless Comp. Lett.*, vol. 25, no. 8, pp. 511–513, Aug. 2015. DOI: 10.1109/LMWC.2015.2440662.

[101] F. Arndt, J. Dittloff, U. Papziner, D. Fasold, N. Nathrath, and H. Wolf, "Rigorous field theory design of compact and lightweight broadband diplexers for satellite communication systems," in *Proc. 19th Eur. Microwave Conf.*, London, UK, Sep. 1989. DOI: 10.1109/EUMA.1989.334139, pp. 1214–1219.

[102] L. Accatino, "Computer-aided design of a Ku-band antenna diplexer," in *Proc. 23th Eur. Microwave Conf.*, Madrid, Spain, Sep. 1993. DOI: 10.1109/EUMA.1993.336621, pp. 544–546.

[103] J. Esteban and J. Rebollar, "Design and optimization of a compact Ka-band antenna diplexer," in *IEEE AP-S Int. Symp. Dig.*, vol. 1, Newport Beach, VA, Jun. 1995. DOI: 10.1109/APS.1995.529984, pp. 148–151.

[104] HFSS High Frequency Simulation Software. Ansys Inc., Pittsburgh, PA. [Online]. Available: https://www.ansys.com/products/electronics/ansys-hfss

[105] A. D. Rawlins, J. S. Petit, and S. Mitchell, "PIM characterisation of the ESTEC Compact Test Range," in *Proc. 28th Eur. Microwave Conf.*, vol. 2, Amsterdam, The Netherlands, Oct. 1998. DOI: 10.1109/EUMA.1998.338211, pp. 544–548.

[106] D. Smacchia, P. Soto, V. E. Boria, D. Raboso, and M. Guglielmi, "Comparison of third order passive inter-modulation products in two and three high power RF carriers scenarios," in *Proc. 9th Int. Workshop Multipactor, Corona and Passive Intermodulation*, Noordwijk, The Netherlands, Apr. 2017, pp. 1–8.

[107] M. Guglielmi, P. Soto, C. Carceller, V. E. Boria, D. Smacchia, M. Brumos, S. Cogollos, B. Gimeno, and D. Raboso, "A novel Ku-band test bed for passive intermodulation measurements," in *Proc. 8th Int. Workshop Multipactor, Corona and Passive Intermodulation*, Valencia, Spain, Sep. 2014, pp. 1–6.